SAR

DTIC
ELECTE
JUN 21 1973
S D
B

JASON
MITRE

DTIC QUALITY INSPECTED 5

19950616 047

DISCLAIMER NOTICE

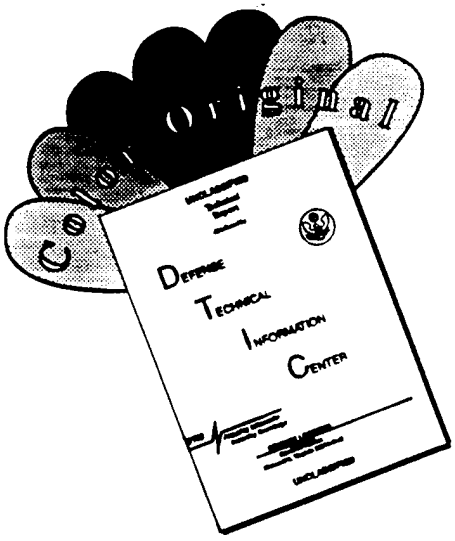

THIS DOCUMENT IS BEST QUALITY AVAILABLE. THE COPY FURNISHED TO DTIC CONTAINED A SIGNIFICANT NUMBER OF COLOR PAGES WHICH DO NOT REPRODUCE LEGIBLY ON BLACK AND WHITE MICROFICHE.

SAR

P. Banks
M. Cornwall
W. Dally
A. Despain
F. Dyson
S. Flatté
J. Goodman
P. Horowitz
W. Nierenberg
F. Perkins
A. Peterson
T. Prince
W. Press
O. Rothaus
J. Vesecky
P. Weinberger

DTIC
ELECTE
JUN 20 1995
S D
B

April 1995

JSR-93-170

Approved for public release; distribution unlimited.

JASON
The MITRE Corporation
7525 Colshire Drive
McLean, Virginia 22102-3481
(703) 883-6997

REPORT DOCUMENTATION PAGE

Form Approved
OMB No. 0704-0188

Public reporting burden for this collection of information estimated to average 1 hour per response, including the time for review instructions, searc hing existing data sources, gathering and maintaining the data needed, and completing and reviewing the collection of information. Send comments regarding this burden estimate or any other aspect of this collection of information, including suggestions for reducing this burden, to Washington Headquarters Services, Directorate for Information Operations and Reports, 1215 Jefferson Davis Highway, Suite 1204, Arlington, VA 22202-4302, and to the Office of Management and Budget. Paperwork Reduction Project (0704-0188), Washington, DC 20503.

1. AGENCY USE ONLY (*Leave blank*)	2. REPORT DATE	3. REPORT TYPE AND DATES COVERED
	April 20, 1995	

4. TITLE AND SUBTITLE	5. FUNDING NUMBERS
SAR	04-958533-01
6. AUTHOR(S)	
A. Despain et.al	
7. PERFORMING ORGANIZATION NAME(S) AND ADDRESS(ES)	**8. PERFORMING ORGANIZATION REPORT NUMBER**
The MITRE Corporation JASON Program Office 7525 Colshire Drive McLean Virginia 22102	JSR-93-170
9. SPONSORING/MONITORING AGENCY NAME(S) AND ADDRESS(ES)	**10. SPONSORING/MONITORING AGENCY REPORT NUMBER**
Advanced Research Projects Agency 3701 North Fairfax Drive Arlington, Va 22203-1714	JSR-93-170

11. SUPPLEMENTARY NOTES

12a. DISTRIBUTION/AVAILABILITY STATEMENT	12b. DISTRIBUTION CODE
Approved for Public Release, Distribution Unlimited	

13. ABSTRACT *(Maximum 200 words)*

This report: 1) explores reformulations of the theory of SAR imaging so as to understand how to improve SAR images, structure parallel algorithms and machine architectures and to see what new SAR applications may be possible, 2) examines the issue of formulating parallel algorithms, 3) examines massive parallel computer architectures to determine the possibilities and limits provided by today's and the future massively parallel processors, 4) explores novel methods enabled by massive computing in SAR computation, 5) considers the role of countermeasures, 6) looks forward to how new SAR systems can be designed to exploit massive computing capabilities, and 7) identifies a number of research issues for future study. Lastly, the report draws conclusions as to the role of massive computing in SAR technology.

14. SUBJECT TERMS			15. NUMBER OF PAGES
			16. PRICE CODE
17. SECURITY CLASSIFICATION OF REPORT	18. SECURITY CLASSIFICATION OF THIS PAGE	19. SECURITY CLASSIFICATION OF ABSTRACT	20. LIMITATION OF ABSTRACT
Unclassified	Unclassified	Unclassified	SAR

NSN 7540-01-280-5500

Standard Form 298 (Rev. 2-89)
Prescribed by ANSI Std. Z39-18
298-102

Contents

1 INTRODUCTION **1**

1.1 SAR and Massively Parallel Computers (MPCs) 1
1.2 Importance of SAR 6
1.3 Importance of SAR to DOD Missions 7
1.4 New SAR Capabilities Enabled by MPCs 7
1.5 Processing Required by Future SARs 8
1.6 Overview of the Report 8

2 THEORY **11**

2.1 First Principles Reformulation 11
2.2 Iterative Algorithm 14
2.3 Stochastic SAR Algorithm 18
2.3.1 Inversion Algorithm 20
2.3.2 Computing Load 21
2.3.3 Signal–To–Noise Ratio 22
2.3.4 Effects of Limited Time and Bandwidth 26
2.4 Exact Inversion of the SAR Equation 27
2.5 Analytic Inversion 39
2.6 An Alternative to Polar Reformatting 44
2.7 Estimating the Correct Pixel Phase During SAR Processing . 48
2.7.1 Phase Errors in Complex SAR Images 48
2.7.2 Optimal Time Domain Imaging 50
2.7.3 Origins of Phase Errors 51
2.7.4 Established Processing Schemes 52
2.7.5 Polar Algorithms 58
2.7.6 Summary and Conclusions 60
2.8 Atmospheric and Ionospheric Propagation 61
2.8.1 Ionospheric Phase Fluctuations 63
2.8.2 Ionospheric Amplitude Fluctuations 66
2.8.3 Tropospheric Phase Fluctuations 67
2.8.4 Tropospheric Amplitude Fluctuations 69
2.8.5 Effects on SAR (Change Detection) 70

DTIC TAB
Unannounced
Justification
By
Distribution/
Availability Codes
Dist | Avail and/or Special
A-1

3 PARALLEL PROCESSING **73**
3.1 Introduction 73
3.2 Evaluation of MPCs for SAR Computation 73
3.3 Approach 74
3.3.1 Evaluation of Systems 76
3.3.2 Future Trends 78
3.4 Custom SAR Processors 80
3.4.1 Required Memory, Bandwidth, and Processing 82
3.4.2 Silicon Area Required 84
3.4.3 Alternative Designs 87
3.4.4 Latency, Throughput, and Cost 92
3.4.5 Commercial DSP-Based Design 94
3.4.6 Commercial Multiprocessor and Multicomputers 95
3.5 Brute-Force SAR Processing 97
3.5.1 Brute-Force Convolution 97
3.6 What Number of Parallel Processors Are "Right" for SAR? . . 100
3.7 What Computer Architectures Will Do SAR Processing? . . . 102
3.8 Massive Mapping Project 106

4 NOVEL METHODS IN SAR EXPLOITATION **109**
4.1 Moving Targets 109
4.1.1 Future SARS 114
4.1.2 SAR Processing 115
4.1.3 Ground Targets and Their Shadows 123
4.1.4 Subaperture Processing 127
4.1.5 Frequency-Domain Processing 128
4.2 SAR Processing for Airborne Azimuthal Scan Radars 132
4.2.1 Periscope Radars: The Case for an Azimuthal-Scan SAR135
4.3 Battlefield Scanning SAR 145
4.4 Measurement of the Atmosphere and the Ionsphere 146
4.5 SAR for Measuring Land and Ocean Characteristics 148
4.5.1 Overview of SAR and Environment Science 148
4.5.2 What SAR can do that "photography" can't 149
4.5.3 Example Applications in Environmental Science 151
4.5.4 Multi-frequency, Polarimetric SAR 162
4.6 Imaging of Underground Phenomena by SAR 163
4.7 SAR Detection of Vibrating Objects 167

5 SAR COUNTERMEASURES **175**
5.1 Concealment and Nets 175
5.2 Signature Diversity and Anti-Simulation 176
5.3 Decoys and Jamming 179

6 SAR OF THE FUTURE **181**
6.1 SAR Waveforms: Introduction 181
6.1.1 Stochastic SAR Waveforms 182
6.1.2 Deterministic Coding 183
6.2 Geosynchroneous-Orbit Bistatic SAR 197
6.2.1 Public-Service SAR Parameters 199
6.2.2 Instant Interferometry 203
6.2.3 Incoherent 3-D SAR 206
6.2.4 Bistatic Detection of Aircraft 207
6.3 Low-Earth-Orbit "Bistatic" Battlefield SAR 212

7 CONCLUSIONS **225**

A PROOF OF EQUATION (2-34) **233**

B PROOF OF EQUATION (2-42) **235**

C SAR ON A SPHERE **237**

1 INTRODUCTION

1.1 SAR and Massively Parallel Computers (MPCs)

"SAR" stands for "Synthetic Aperture Radar". The basic idea, as illustrated in Figure 1-1, is to have a vehicle send out radar pulses and coherently record the returns across an aperture of a very large number of wavelengths. A high resolution image is then computed from the recorded returns. Thus the aperture is synthesized and an image is formed through the recording and calculation process. The result can be a spectacular image, of excellent resolution, useful for many diverse tasks. Because the image is coherently formed and its phase recorded, (unlike photographic images) it can be exploited in ways that an ordinary photograph cannot.

SAR technology began in June 1951 when Wiley (1965) discovered how to improve azimuth resolution of ordinary radar by processing the Doppler spread of the returned radar signal. Today, SARs are widely used on airplanes and spacecraft for military surveillance and civilian environmental studies.

A typical SAR vehicle, the Seasat-A SAR Satellite, is illustrated in Figure 1-2. It has an antenna length of about 10 m and operates with a wavelength of about 24 cm. Seasat-A was launched in 1978 and provided a ground resolution of 23 meters. A similar SAR satellite was the "ALMAZ" launched by the USSR in 1981.

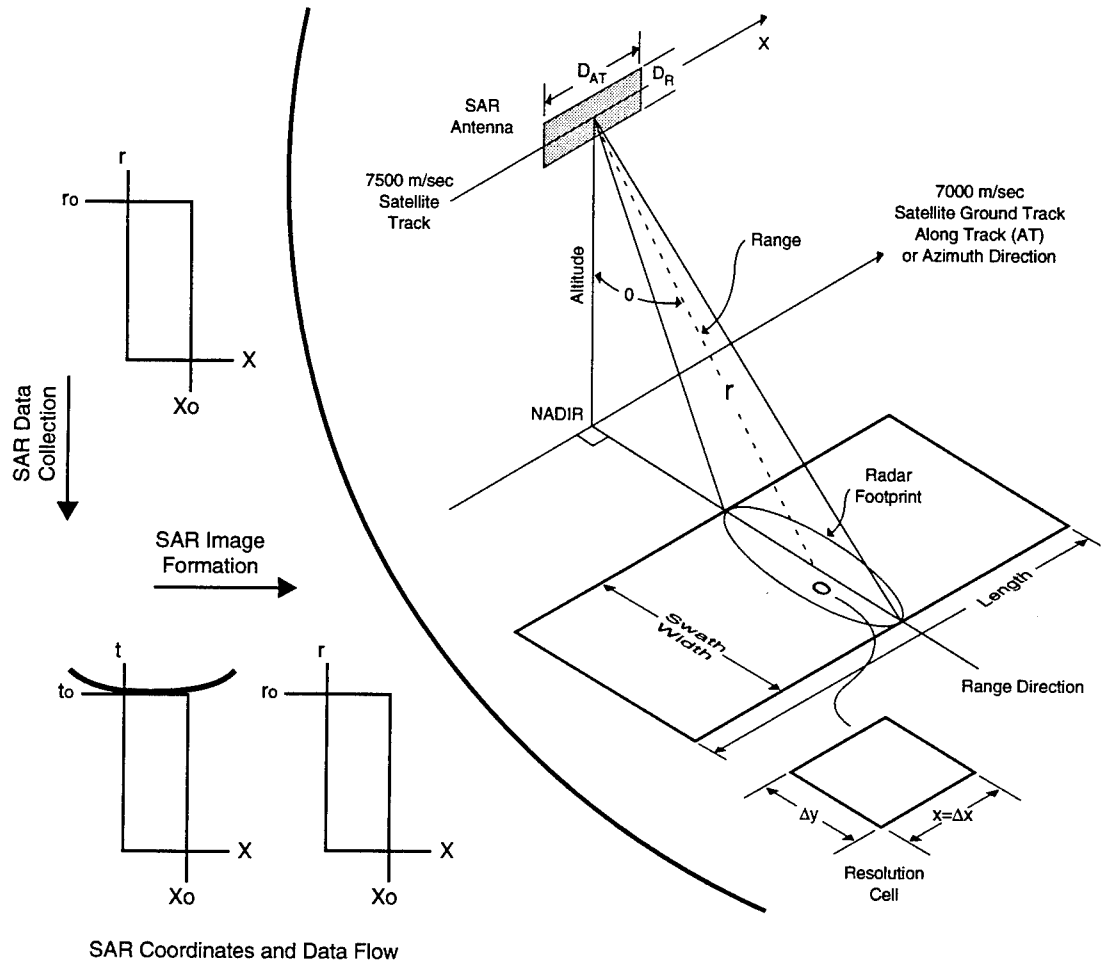

Figure 1-1. Synthetic Aperture Radar Basics

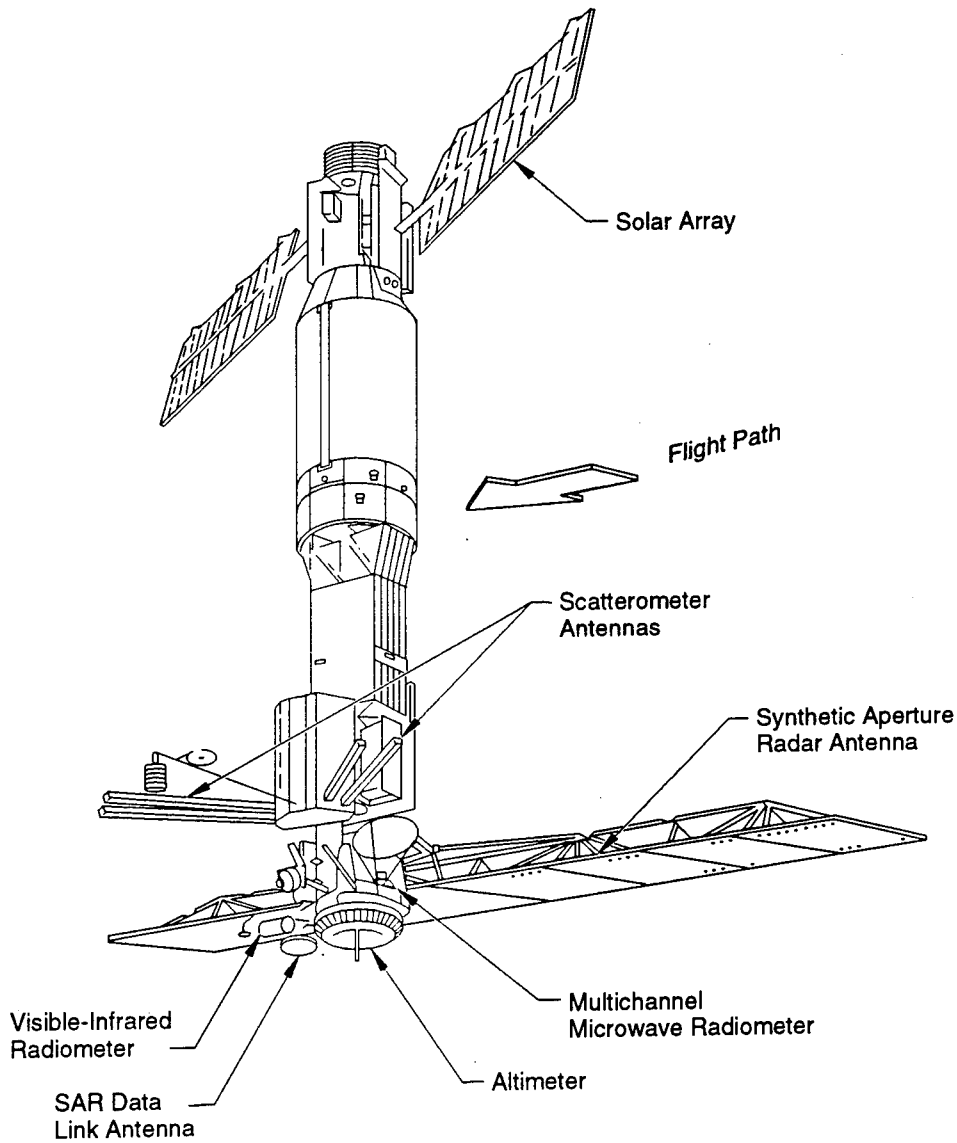

Figure 1-2. Illustration of the Seasat-A SAR satellite.

It is a counter intuitive fact that the limit to ground resolution is about the actual aperture of the SAR antenna. Thus smaller SAR antennas are needed for increased resolution. However, smaller antennas spread out the radar beam, thus requiring more transmitter power.

Figure 1-3 is an illustration of a typical SAR image. The physical antenna was about 8 m along track and 1 m transverse to the track. The size of the synthetic aperture for this image is 100 km. Samples of the returned radar pulse were measured and recorded during the 15 second transit time of the vehicle across the aperture. Many millions of samples were then processed by a digital computer to produce this image.

SAR technology has steadily improved, primarily due to advances in computing. At first, simple analog signal processing was employed to improve radar resolution. Then optical correlators were employed to produce higher resolution radar images. However, analog and optical devices have limited dynamic range and undesirable nonlinearities. This severely limits the quality of SAR images.

Digital processing began in about 1970, first with special purpose processors designed for SAR and just recently with general-purpose computers. Today, about 100 operations are required to compute each pixel. For a typical SAR image of 10^8 to 10^9 pixels, about 10 to 100 giga operations are required. For real-time operation of 10 seconds per picture, 1 to 10 GOPS (giga operations per second) are required. The recent advent of much more powerful computing promises many more applications of SAR technology.

ESA/EARTHNET
★ SEASAT 1 SAR IMAGE ★

ORBIT 762
RECEIVED AT UKO
ON THE 19 AUG 1978
DIGITALLY PROCESSED
AT THE ROYAL AIRCRAFT
ESTABLISHMENT, UK, ON
THE 23 JAN 1980 USING
THE EXPERIMENTAL SAR
PROCESSOR DEVELOPED BY
SYSTEMS DESIGNERS LTD.

★IMAGE GRID PARAMETERS
ORIGIN, LAT 51: 0: 0 N
LONG 2:30: 0 E
ROTATION OF +Y AXIS
FROM TRUE NORTH,
= -27.50 DEG
PIXEL SPACING,
X AXIS = 20.00 M
Y AXIS = 20.00 M

★ IMAGE PARAMETERS
IMAGE EXTENT,
X AXIS, FROM -20.000KM
TO 20.000KM
Y AXIS, FROM -10.000KM
TO 30.000KM
IMAGE CENTRE,
LAT 51: 4:47 N
LONG 2:26: 3 E
GMT OF IMAGE CENTRE
= 6 HR 45 MIN 56 SEC
INCIDENCE ANGLE AT
IMAGE CENTRE=23.277DEG

★PROCESSING PARAMETERS
RESOLUTION,
IN AZIMUTH= 25 M
IN RANGE = 21 M
SIDELOBE LEVEL,
AZIMUTH=-24.3 DB
RANGE =-24.3 DB
★★★ WARNING- PARTIALLY
DEPENDENT LOOKS
HAVE BEEN SUPERIMPOSED
LOOK NUMBERS USED
= 1 3 5
SUB APERTURE WIDTH
= 0.249 DEG
SUB APERTURE DOPPLER
BANDWIDTH = 282 HZ
LOOK CENTRES RELATIVE
TO ANTENNA BORESIGHT
(POSITIVE LEADING),
NUMBER 1 = 0.000 DEG
NUMBER 3 = 0.249 DEG
NUMBER 5 =-0.125 DEG
ROTATION OF +Y AXIS
FROM THE ACROSS TRACK
DIRECTION (INCR. RANGE)
= -89.664 DEG

RUN IDENTIFIER 762104

Figure 1-3. A typical SAR image. The image is about 40 x 40 km in size and shows the coast of Belgium along the English channel, including Dunkirk. The structures in the top half of the image are offshore bottom features that are manifested as ocean surface roughness changes. SEASAT image processed by RAE Farnborough.

The goal of this report is to examine issues and opportunities for employing massive parallel computing in the service of SAR.

1.2 Importance of SAR

SAR is important because it offers remote observational capabilities that cannot be achieved by ordinary photography or other means. In particular, SAR works just as well in total darkness and bad weather. It can produce some kind of (perhaps distorted) image of targets obscured by materials or structures so long as the radar pulses can penetrate and return through these. For example a SAR has imaged channels cut into bedrock but covered by dry sand.

Because the radar signal can be tailored as to wavelength, bandwidth, polarization, and modulation, some properties of the materials that reflected back the radar pulse can be determined. For example SAR signals can be processed to learn something about the sea ice.

SAR signals are coherent. Thus it is possible to produce a synthetic interferometer with each pixel in a scene by proper registration of two independent, (in time) complex SAR images of the same scene. The result is that any changes in the scene that occur between the sampling of the two SAR images will produce interference fringes. This allows the measurement of tiny shifts (down to fractions of a wavelength if desired) in the surface of the earth, produced for example, by earthquakes. Motion of objects can similarly be determined.

Exploitation of SAR, as suggested above, requires enormous computing. The new massive parallel processors offer new possibilities for exploiting SAR. We will examine in this report several new possibilities for exploiting SAR that can be enabled by Massive Parallel Processing (MPC).

1.3 Importance of SAR to DOD Missions

SAR can provide high quality images in near real time, day and night and through good and bad weather. This is important to successful warfighting. For the United States, this requires not only winning, but doing so while suffering extremely small friendly and civilian casualties, such as recently demonstrated in Desert Storm. Warfighting is controlled by tempo...the ability to react faster than an adversary can make and execute decisions, at all levels of combat. This requires timely information about what the adversary is doing. SAR technology can provide much of this information in real time, by displaying high resolution images of all the forces in play. Massive real time computing is required to produce such images in large numbers for the many purposes needed in battle.

1.4 New SAR Capabilities Enabled by MPCs

In this report, one of our goals is to determine what new SAR capabilities can be enabled by massive parallel computing. Possibilities include smaller, light-weight SAR instruments, the ability to detect and characterize moving

targets, characterize object motion and vibration, estimate environmental parameters, detect changes in scenes over time and produce 3-D maps.

1.5 Processing Required by Future SARs

It seems likely that the cost of computer processing will continue its dramatic drop each year. This, coupled with the likely increase in demand for SARs unique product, will result in the use of much more computing for SAR. At the same time better SAR instruments are also being developed that themselves employ more computing to produce more and better images. In addition, there may be a significant trade-off between expensive flight hardware and massive computing on the ground.

1.6 Overview of the Report

This report of our study proceeds "top-down". First, we explore reformulations of the theory of SAR imaging so as to understand how to improve SAR images, structure parallel algorithms and machine architectures and to see what new SAR applications may be possible. Second, we examine the issue of formulating parallel algorithms. Third, we examine massive parallel computer architectures to determine the possibilities and limits provided by todays and the future massively parallel processors. Fourth, we explore novel methods enabled by massive computing in SAR computation. Fifth, we consider the role of countermeasures. Sixth, we look forward to how new SAR systems can be designed to exploit massive computing capabilities. Seventh,

we identify a number of research issues for future study. Lastly, we draw conclusions as to the role of massive computing in SAR technology.

2 THEORY

2.1 First Principles Reformulation

The theory of SAR image formation has a long history. Today there are a large number of formulations, each with advantages and disadvantages. In this section, we will reformulate the SAR image formation equation from first principles. We will then develop two new variations that will have some new intriguing properties. Finally, we will examine these and some of the other classic formulations for the approximations they employ. Then the corresponding damage they cause in image quality can be assessed.

The general formulation is illustrated in Figure 2-1. Let $\mathbf{s}(t)$, a 3–vector, be the 3–dimensional position of the SAR transmitter as a function of time t. Let (x, y) be two dimensional coordinates on the ground, that is, positions on the topographically distorted "drape" of the Earth. We will assume for now that the drape (topography) is known, although this could easily be relaxed and the drape solved–for, exactly as in present SAR techniques, e.g., autofocus. Then let $\mathbf{r}(x, y)$ be the 3–dimensional position of the draped point (x, y). Let $\sigma(x, y)$ be the monostatic radar cross section (RCS) per unit area at the point (x, y). (Implicitly, this is from the illuminating direction. To keep the notation simple, we won't include the directional dependence explicitly.)

We let $R(t)$ represent the received radar signal where $\mathrm{T}(t')$ is the transmitted signal. Then $R(t)$ can be written in the form of an integral over all

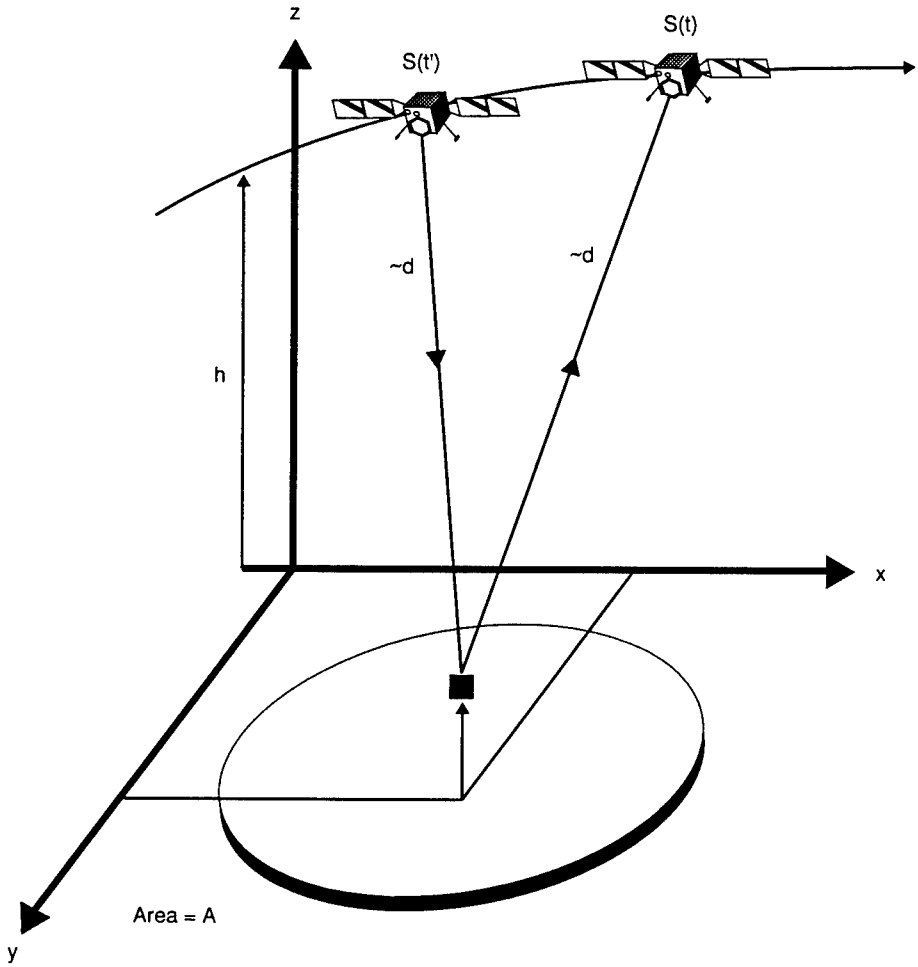

Figure 2-1. General Formulation

points x and y, and all times of previous transmission t' as (to good accuracy)

$$R(t) = \int\int\int dx\, dy\, dt' T(t') \frac{\sigma(x,y)}{(d/2)^2} \delta(t - t' - d)) \tag{2-1}$$

where $d = d(x, y, t, t')$ is the two–way propagation distance to the point (x, y),

$$d = |\mathbf{s}(t') - \mathbf{r}(x,y)| + |\mathbf{s}(t) - \mathbf{r}(x,y)| \tag{2-2}$$

and δ is the Dirac delta function.

At every time t we can view $R(t)$ as giving an independent sample. Similarly, we can discretize $\sigma(x, y)$ by sampling at discrete positions (x_i, y_j). Then Equation (2-3) can be viewed as a very large set of *linear algebraic equations* relating the measured values $R(t)$ to the unknowns $\sigma(x_i, y_j)$.

$$R(t) = H\sigma(x_i, y_j) \tag{2-3}$$

or in matrix form

$$R = H\sigma. \tag{2-4}$$

The formal solution to the imaging problem is then

$$\sigma = H^{-1}R. \tag{2-5}$$

A number of approximations have been made in this formulation. First it is erroneously assumed that the vehicle flight path, the DTED and the instrument artifacts (such as phase errors) are known exactly. Second, features on the ground that are sometimes shadowed by other regions, are not taken into account. Third, multiple paths will occur when a radar signal 'bounces' from a ground feature, illuminates another ground feature and scatters back to the vehicle. Fourth, the finite-sized reflectance element $\sigma(x_i, y_j)$ will contain multiple unresolved, but coherent, scatter, causing 'speckle' patterns in

the final image. Later we will discuss how these errors and approximations are handled.

It can be seen that σ is just the solution of the linear algebraic equations in which N is the number of equations and unknowns. N is just the number of pixels, say 10^6 to 10^8. (One might want to have more samples of R(t) than the number of pixels, in which case one might want the pseudo–inverse or least squares solution to the linear system.)

A direct solution of Equation (2-4) will require $O(N^3)$ or on the order of 10^{18} to 10^{24} arithmetic operations! This is clearly impractical today. Therefore all practical imaging algorithms make various additional approximations to reduce the number of calculations needed to form an image.

2.2 Iterative Algorithm

Here we suggest a new approach, that as far as we know, has not been employed to produce SAR images. Assume that somehow Equation (2-4) has been approximately solved and we would like to calculate a better estimate of the image. We can then perhaps solve Equation (2-4), with massively parallel computation, using iterative methods.

Consider the general problem of solving a set of linear equations, expressed as the matrix equation

$$\mathbf{A}\mathbf{x} = \mathbf{b}. \tag{2-6}$$

Suppose that a fast method is available for solving some slightly different problem, obtaining

$$\mathbf{x} = \mathbf{B}_0\mathbf{b} \tag{2-7}$$

where $\mathbf{B}_0$ is an *approximate inverse* of $\mathbf{A}$. The goodness of approximation can be measured by the residual matrix

$$\mathbf{R} \equiv \mathbf{I} - \mathbf{B}_0\mathbf{A} \tag{2-8}$$

where $\mathbf{I}$ is the identity matrix. $\mathbf{B}_0$ is a good approximate inverse to $\mathbf{A}$ if $\mathbf{R}$ is small, in the sense of having all eigenvalues less than (hopefully, much less than) unity.

Now (following *Numerical Recipes in Fortran*, p. 49) consider the following formal manipulation:

$$\begin{aligned} \mathbf{A}^{-1} &= \mathbf{A}^{-1}(\mathbf{B}_0^{-1}\mathbf{B}_0) = (\mathbf{A}^{-1}\mathbf{B}_0^{-1})\mathbf{B}_0 = (\mathbf{B}_0\mathbf{A})^{-1}\mathbf{B}_0 \\ &= (\mathbf{1} - \mathbf{R})^{-1}\mathbf{B}_0 = (\mathbf{1} + \mathbf{R} + \mathbf{R}^2 + \mathbf{R}^3 = \cdots)\mathbf{B}_0. \end{aligned} \tag{2-9}$$

We can define the nth partial sum of the last expression by

$$\mathbf{B}_n \equiv (\mathbf{1} + \mathbf{R} + \cdots + \mathbf{R}^n)\mathbf{B}_0 \tag{2-10}$$

so that $\mathbf{B}_\infty \rightarrow \mathbf{A}^{-1}$, if the limit exists.

To solve our original problem $\mathbf{A}\mathbf{x} = \mathbf{b}$, define

$$\mathbf{x}_n \equiv \mathbf{B}_n\mathbf{b}. \tag{2-11}$$

Then it is easy to show that

$$\mathbf{x}_{n+1} = \mathbf{x}_n + \mathbf{B}_0(\mathbf{b} - \mathbf{A}\mathbf{x}_n). \tag{2-12}$$

Notice that Equation (2-12) has a very simple intuitive interpretation: One solves the desired problem with the approximate inverse $\mathbf{B_0}$, then computes a residual vector **b - Ax**, then again solves, with the approximate inverse applied to the residual. And so on. This method now has a computational complexity of $O(N^2)$ or 10^{16} to 10^{18} arithmetic operations. This is very large but not unthinkable.

Our goal then, is to find a sufficiently good inverse to Equation (2-3) so that the iteration Equation (2-12) converges rapidly. Furthermore, the starting estimate to σ must not be too expensive to calculate. There are many methods that can be employed.

As only a crude illustration consider an example where we let T(t) be the transmitted complex phasor of the SAR at time t, that is, the transmitted complex amplitude "unwound" by the band center frequency. We only require that the two-point autocorrelation function for T,

$$< T(t)T(t-\tau) > \tag{2-13}$$

should be T_0^2 at $\tau = 0$ and decrease smoothly and rapidly to zero for τ greater than some $\tau*$, the characteristic correlation time (whose inverse approximates the channel bandwith).

Consider now, a crude "tomographic inverse" of the form

$$\sigma(x,y) = \text{ const } \times \int\int dt\, dt' \frac{R(t)}{T(t')} d^2\delta(t-t'-d). \tag{2-14}$$

This basically paints a stripe at constant range for each transmitted chip. In fast time, the different ranges are disambiguated by the incoherent addition of the random transmitted code. In slow time, the along–track direction is

resolved (after a fashion) by the changing direction of the constant range surfaces.

One can readily show that the impulse response of this approximate inverse, that is the quantity $\mathbf{B}_0\mathbf{A}$ in the language of Equation (2-8), is a "bow–tie" pattern. The angular opening of the bow–tie is the change in angle of the SAR during the data accumulation. In general, outside of the bow–tie pattern, the response is stochastically down by something that scales as the square root of the total number of pulses; within the bow–tie (along track) the density of the response scales as $1/s$ where s is the distance to the center of the cross.

Unfortunately, the tomographic inverse (Equation(2-14)) is not sufficiently good for the iteration (Equation (2-12)) to converge: the eigenvalues of the residual matrix are logarithmically divergent, which corresponds to the fact that the energy in the bow–tie, integrated cross–track, is actually uniform along–track, with no concentration at the center of the cross.

A relatively conventional processing approach would be, now, to deconvolve the bow–tie pattern by FFT methods, then use the deconvolved result in the iteration Equation (2-12). However, although we have not worked out all details, there is some good evidence that somewhat cleverer approximate inverses than the inverse of Equation (2-14) can directly achieve results that will converge under iteration. These estimates of $\sigma(x, y)$ are developed below.

2.3 Stochastic SAR Algorithm

For certain waveforms, one would be able to show that the matrix implied by Equation (2-3) reduces to a special form whose inverse can be obtained by special, fast methods such as the FFT. Here we want to take a different tack. We want to keep $T(t)$ general. Our main assumption is that the autocorrelation of the transmitted signal be like that of stochastic signals:

$$\langle T(t_1)T^*(t_2)\rangle = T_o^2.\delta(t_1 - t_2). \tag{2-15}$$

If we multiply the receiver signal Equation (2-1) at time t by the complex conjugate of the transmitter signal at time t', and take the expectation-value the result is

$$\langle R(t)T^*(t')\rangle = T_o^2 \int\int \sigma(x,y)dxdy(d/2)^{-2}\delta(t - t' - d). \tag{2-16}$$

Note that Equation (2-16) is totally untrue if the expectation value is not taken on the left side. It can only be true in some average sense when integrated over t and t'.

Suppose that the radar is moving uniformly in the x-direction with velocity V along the track with constant $y = 0$. If the coherent integration of signals is over a distance short compared with the range

$$r = |r(x,y)|, \tag{2-17}$$

the distance (Equation (2-2)) can be approximated by the linear expression

$$d = 2r - Vc(t + t'), \tag{2-18}$$

$$c = (x/r). \tag{2-19}$$

It is convenient to use polar coordinates (r, c) instead of (x, y). The radar cross-section in terms of polar coordinates is

$$f(r, c) = (r^2/|y|)\sigma(x, y), \tag{2-20}$$

$$f(r, c)drdc = \sigma(x, y)dxdy. \tag{2-21}$$

Then Equation (2-16) becomes

$$\langle R(t)T^*(t')\rangle = T_o^2(u/2)^{-2} \int\int f(r, c)drdc\, \delta(u - 2r + Vcv), \tag{2-22}$$

with

$$u = t - t', v = t + t'. \tag{2-23}$$

Equation (2-22) has the form of a tomographic image of the source-distribution $f(r, c)$, giving the integral of the source along each line

$$2r - Vcv = u \tag{2-24}$$

in the (r, c) plane. To determine $f(r, c)$ from Equation (2-22), we need only to invert the tomographic image to obtain the true image.

To do the inversion we use the Mexican–hat function $\phi(x)$, which is defined as a distribution with the properties

$$\phi(x) = \int_o^\infty \mu \cos \mu x d\mu, \tag{2-25}$$

$$\phi(x) = (d/dx)^2 \log |x| = -x^{-2}, \tag{2-26}$$

and as a limit by the expression

$$\phi(x) = \lim_{\epsilon \to o} \frac{\epsilon^2 - x^2}{(\epsilon^2 + x^2)^2}. \tag{2-27}$$

The right side of Equation (2-26) has the shape of a Mexican hat with a narrow maximum

$$\phi(x) = \epsilon^{-2} \text{at } x = 0 \tag{2-28}$$

and broad wings with minima

$$\phi(x) = -\frac{1}{8}\epsilon^{-2} \text{at } x = \pm\sqrt{3}\epsilon. \tag{2-29}$$

When integrals are approximated by finite sums over integer variables, the Mexican-hat function is replaced by the discrete function of an integer k,

$$\phi(k) = \int_o^\pi (\mu - \frac{\mu^2}{2\pi}) \cos \mu k d\mu, \tag{2-30}$$

$$\phi(k) = -k^{-2} \text{ for } k \neq o, \tag{2-31}$$

$$\phi(0) = (\pi^2/3). \tag{2-32}$$

2.3.1 Inversion Algorithm

If

$$g(a,b) = \int\int f(r,c)\delta(r-a-bc)drdc, \tag{2-33}$$

then

$$f(r,c) = \frac{1}{2\pi^2}\int\int g(a,b)\phi(r-a-bc)\, da\, db. \tag{2-34}$$

The proof of Equation (2-34) is given in Appendix A. Application of Equation (2-34) to invert Equation (2-22) gives the result

$$f(r,c) = \frac{V}{2\pi^2 T_o^2}\int\int \langle R(t)T^*(t')\rangle\,(t-t')^2\phi(t-t'-2r+Vc(t+t'))dtdt'. \tag{2-35}$$

2.3.2 Computing Load

A "Brute Force" calculation of Equation (2-35) would require a double integral over time for each pixel of the image. The total number of operations would then be of the order $N^3 = m^6$, where $N = m^2$ is the number of pixels. The number of operations can be greatly reduced by using fast Fourier Transforms, as is customary in the data-processing of conventional SAR. The inversion algorithm Equation (2-35) is essentially the same as the standard algorithm known as CBP (Convolution Back Projection) [1].

Let $\tilde{R}_\kappa(u), \tilde{T}_\kappa(u)$ be the Fourier Transforms of $t^\kappa R(t), t^\kappa T(t)$ for $\kappa = 0, 1, 2$. The computation of $\tilde{R}_\kappa$ and $\tilde{T}_\kappa$ requires only $(N \log N) \sim (m^2 \log m)$ operations. Then Equation (2-35) becomes

$$f(r,c) = \frac{V}{4\pi^2 T_0^2} \int |\mu| \exp(-2\,\mathrm{i}\,\mathrm{r}\mu)\mathrm{d}\mu.$$

$$\times \left[\tilde{R}_2\left((1+Vc)\mu\right)\tilde{T}_0^*\left((1-Vc)\mu\right) - 2\,\tilde{R}_1\tilde{T}_1^* + \tilde{R}_0\,\tilde{T}_2^*\right]. \qquad (2\text{-}36)$$

Unfortunately the N products in the integrand of Equation (2-36) must be computed separately for each of the m values of the azimuth c, and the FFT integration must also be done separately for each c. Therefore the number of operations required for computing Equation (2-36) for a stochastic SAR is of order

$$m\,N + m\,N \log N \sim N^{3/2}\,\log N \sim m^3 \log m. \qquad (2\text{-}37)$$

This means that stochastic SAR may be practical for $m \leq 10^4$ but is impractical for $m \sim 10^5$.

For conventional SAR the numbers are much more favorable. The transmitted signal $T(t)$ is then periodic with period f^{-1}, where f is the pulse repetition frequency. The fourier transforms $\tilde{T}_\kappa(u)$ are non-zero only when u is an integer multiple of $2\pi f$. The number of products in the integrand of Equation (2-36) is of order m for each value of c, making $N = m^2$ products altogether. The FFT integration of Equation (2-36) requires only $m \log m$ operations for each value of c. The number of operations required for computing Equation (2-36) for a conventional SAR is of order

$$m^2 + m^2 \log m \sim m^2 \log\ m \sim N \log N, \tag{2-38}$$

which is practical at least up to $m \sim 10^5$. This shows that Equation (2-36) is an efficient algorithm for a conventional SAR. The difference between Equations (2-37) and (2-38) shows that either (A) a better algorithm than Equation (2-36) for the processing of stochastic SAR remains to be discovered, or (B) stochastic SAR is inherently inferior to conventional SAR for computational reasons. More work is needed to decide whether (A) or (B) is true.

2.3.3 Signal–To–Noise Ratio

When we use the algorithm (Equation (2-35)) to compute the radar cross–section image from real data, we are dealing with a single instance of the transmitter output $T(t)$ and not with an ensemble. The computed value of $f(r, c)$ is given by Equation (2-35) without the expectation-value brackets

<>. Let the computed value of $f(r,c)$ be $\hat{f}(r,c)$. Then the mean-square noise caused by the stochastic nature of the transmission is

$$n^2 = \left\langle |\hat{f}(r,c) - f(r,c)|^2 \right\rangle = \left\langle |\hat{f}(r,c)|^2 \right\rangle - |f(r,c)|^2. \tag{2-39}$$

When Equation (2-39) is expanded using Equations (2-35) and (2-6), the result is an integral over the fourth-order correlation function

$$\langle T(t_1)T^*(t_1')T^*(t_2)T(t_2\,')\rangle\,, \tag{2-40}$$

which for a white-noise transmission is a sum of two terms

$$T_o^4\left[\delta(t_1 - t_1')\delta(t_2 - t_2') + \delta(t_1 - t_2)\delta(t_1' - t_2')\right]. \tag{2-41}$$

The first term gives the square of the expectation–value $f(r,c)$ and is exactly cancelled by the second term in Equation (2-39). The second term in Equation (2-41) gives the stochastic noise n^2. A lengthy calculation summarized in Appendix B gives the noise–to–signal ratio

$$\begin{aligned}(\frac{n}{S})^2 = \left(\frac{n}{f(r,c)}\right)^2 &= \frac{V}{\pi^2}\int\int\int\int dr_1 dr_2 dc_1 dc_2 \\ \left(\frac{r^2}{r_1 r_2}\right)^2 &\frac{f(r_1c_1)f^*(r_2c_2)}{|f(rc)|^2}\phi(r_1 - r_2)\delta(c_1 - c_2).\end{aligned} \tag{2-42}$$

It is easy to understand the result (Equation 2-42) qualitatively as the effect of cross-talk between two reflections at the points (r_1c_1) and (r_2c_2). It is not so easy to understand quantitatively the coefficient (V/π^2). Roughly speaking, the number of independent looks by the radar at each pixel is proportional to V^{-1}, and these V^{-1} looks add coherently in the signal and incoherently in the noise. The large denominator (π^2) is an additional bonus for which we have no simple explanation.

To estimate the size of Equation (2-42) it is convenient to introduce the spectrum of the radar return,

$$\Sigma(\lambda,\mu) = \int\int \frac{f(r',c')}{(r')^2}\exp\left(i(\lambda r' + \mu c')\right)dr'dc'. \tag{2-43}$$

Then Equation (2-42) becomes

$$(\frac{n}{S})^2 = \frac{V}{4\pi^3 P(r,c)}\int\int |\lambda||\Sigma(\lambda,\mu)|^2 d\lambda d\mu, \tag{2-44}$$

where

$$P(r,c) = r^{-4}|f(r,c)|^2 \tag{2-45}$$

is the power–density reflected by the terrain at (r,c). We bound Equation (2-44) by using Cauchy's inequality

$$(\frac{n}{S})^2 \leq \frac{V}{4\pi^3 P(r,c)}(\int\int |\Sigma(\lambda,\mu)|^2 d\lambda d\mu)^{1/2}(\int\int \lambda^2|\Sigma(\lambda,\mu)|^2 d\lambda d\mu)^{1/2}. \tag{2-46}$$

Unless the spectrum has a very peculiar shape, the over–estimate of Equation (2-44) by Equation (2-46) will not be significant. Now Equation (2-43) and Equation (2-45) imply

$$\int\int |\Sigma(\lambda,\mu)|^2 d\lambda d\mu = 4\pi^2\int\int P(r',c')dr'dc' = 4\pi^2 P, \tag{2-47}$$

where P is the total power reflected from the scanned area. Likewise Equation (2-43) gives

$$\int\int \lambda^2|\Sigma(\lambda,\mu)|^2 d\lambda d\mu = 4\pi^2\int\int (r')^{-4}|\partial f/\partial r'|^2 dr'dc' = 4\pi^2(P/L^2), \tag{2-48}$$

where L is the length defined by Equation (2-47) and Equation (2-48). Thus L^2 is the mean–square gradient of the complex radar return on the ground,

and L is a measure of the dominant scale of contrast in the radar image. Note that L measures the scale of phase-variation as well as brightness-variation.

Putting together Equations (2-46), (2-47), and (2-48) we have

$$(\frac{n}{S})^2 \leq \frac{VP}{\pi P(r,c)L}. \tag{2-49}$$

If (r,c) is a point of average brightness in the target area, we have

$$\frac{P}{P(r,c)} = \frac{A}{r}, \tag{2-50}$$

where A is the total area scanned, and

$$\left(\frac{n}{S}\right)^2 \leq VA/\pi Lr. \tag{2-51}$$

If the area consists of m^2 pixels each of linear size p

$$\left(\frac{n}{S}\right)^2 \leq \frac{Vm^2p^2}{\pi Lr} \leq \frac{Vm}{\pi}\frac{\sqrt{A}}{r} < \frac{Vm}{\pi}, \tag{2-52}$$

since the contrast–scale L is at worst equal to p, and the area A is less than r^2. Equation (2-52) is the main result of this analysis.

Note that the velocity V of the SAR is measured in units such that the velocity of light is unity. For SAR carried in an airplane we have roughly

$$V \sim 300(m/\text{sec}) = 10^{-6}, \tag{2-53}$$

$$\left(\frac{n}{S}\right)^2 < 3.10^{-7}m, \tag{2-54}$$

so that the signal-to-noise ratio is comfortably high for m as large as 10^5. For SAR carried in a satellite in low earth orbit we have

$$V \sim 8 \text{ Km/sec} \approx 3.10^{-5}, \tag{2-55}$$

but in this case the ratio

$$\frac{\sqrt{A}}{r} < \frac{10 \text{ Km}}{300 \text{ Km}} = \frac{1}{30}, \tag{2-56}$$

and the estimate (Equation (2-52)) gives the same limit (Equation(2-54)) as for the airplane. The signal–to–noise ratios are high because the motions of airplanes and satellites are highly non-relativistic.

2.3.4 Effects of Limited Time and Bandwidth

Our analysis is quite general and is valid whether the times and bandwidths are limited or not. For example, the radar Equation (2-1) and its inversion Equation (2-36) are written as continuous integrals over time extending from $-\infty$ to $+\infty$, but the band-width and duration of the integrals are automatically limited by the finite bandwidth and duration of the integrands. The bandwidth of the integrand is the smaller of the transmitter band-width and the terrain structure band-width. The duration of the integrand is the smaller of the coherent processing duration of the radar and the duration of travel of the radar over the observed patch of terrain. We assumed for convenience that the radar is matched to the terrain, so that the band-width and duration of the integrals are set by the pixel-size and the patch-size of the terrain. If the radar is not so matched, then the band-width and duration of the integrals are set by the pixel-size and the patch-size of the reconstructed image. In any case, the reconstructed image will be obtained by computing finite sums as in the data-processing of a conventional SAR.

The main result of our analysis is the estimate Equation (2-52) of the stochastic noise arising from the random character of the transmission. This estimate shows the noise depending on the pixel-size p and contrast-scale L and area A of the image. In deriving this estimate, we took fully into account the limited duration and band-width of the radar signals.

2.4 Exact Inversion of the SAR Equation

Equation (2-1), repeated below, can also be solved by an exact inversion.

$$S(t) = \int\int\int dxdydt' \frac{T(t')}{(D/2)^2} \delta(t - t' - \frac{D}{c}) \sigma(x, y),$$

where $T(t)$ is the imaging waveform, and D is the sum of the distances from platform at time t to the point (x, y, o) plus that from point (x, y, o) to the platform at time t'. To make our analysis, we will assume operation in the stop and shoot mode, i.e., the platform does not move during the time it takes the signal to reach the point (x, y, o) and return to the platform. We may also assume the platform is flying along a path in the (x, z) plane at constant height h. Now, letting d = distance from point (ξ, o, h) in flight path to image point (x, y, o), we get for radar return:

$$S(\xi, t) = \int\int dx\, dy \frac{\sigma(x, y)}{4d^2} T(t - \frac{2d}{c}).$$

Taking the Fourier transform of the last equation with respect to t, we obtain

$$\hat{S}(\xi, w) = \hat{T}(w) \int\int dxdy \frac{\sigma(x, y)}{4d^2} e^{\frac{-2iwd}{c}},$$

and assuming T is broadband, we may retrieve

$$k(\xi, w) = \int\int dx\, dy \frac{\sigma(x, y)}{(x - \xi)^2 + y^2 + h^2}\, e^{-iw\sqrt{(x-\xi)^2+y^2+h^2}}.$$

In most procedures, at this point the square root in the exponential is linearized by a Fraunhofer or Fresnel approximation so that a conventional Fourier analysis can be applied. We do not make this convenient assumption, and this perhaps constitutes the greatest novelty in our approach. In the last integral, translate x by ξ, then go to polar coordinates to get

$$k(\xi, w) = \int_0^\infty dr \int_0^{2\pi} d\theta \frac{r\sigma(\xi + r\cos\theta, r\sin\theta}{r^2 + h^2} e^{-iw\sqrt{r^2+h^2}}$$

and substitute again $s = \sqrt{r^2 + h^2}$, obtaining

$$k(\xi, w) = \int_h^\infty ds \int_0^{2\pi} d\theta \frac{\sigma(\xi + \sqrt{s^2 - h^2}\cos\theta, \sqrt{s^2 - h^2}\sin\theta)}{s} \cdot e^{-iws}$$

Finally, an inverse Fourier transform with respect to s gives us

$$K(\xi, r) = \int_0^{2\pi} \sigma(\xi + r\cos\theta, r\sin\theta) d\theta$$

for any positive value of r, and all values of ξ.

(As a matter of fact, the inverse Fourier transform gives us linear constraints on the $k(\xi, w)$, since $k(\xi, w)$ is the transform of a function supported on (h, ∞).)

We can interpret the last integral above as that of the function $\sigma(x, y)$ about an arbitrary circle centered on the real axis, and this interpretation makes the problem quite attractive and suggestive.

Our problem is similar but not identical to standard Computer Aided Tomography (CAT). The problem of CAT is that of finding a function $\sigma(x, y)$ given its integral along all straight lines.

Radon solved the CAT problem in 1917 [2]; the problem was reposed and resolved by Cormack in 1963 [3] for radiographic applications. (Cormack

received the Nobel prize partly for this work.) There is by now enormous literature on this problem [4].

There are many formally different solutions to the Radon problem, the real reason being that the problem is overdetermined. We mean to say that the collection of straight line integrals satisfy a number of linear constraints. Thus if a linear transformation K gives the answer for the data, so also does $K + L$, where L is any linear transformation which annihilates the vector subspace in which the received data must lie.

Our circular tomography problem has the same feature; it is overdetermined, but it also has an additional ambiguity which must be removed. If $\sigma(x, y)$ is an odd function of the 2nd variable, then $K(\xi, r)$, the integral of σ about a circle centered at $(\xi, 0)$ of radius r is identically zero, and σ is unrecoverable. In fact, in the general case, we can only recover the even part of the function σ. So we are going to assume from the outset that σ is even in y. This is no serious difficulty in the practical case of SAR processing—we are imaging a field on one side of the y axis; we simply create a mirror image on the other side.

There is another interpretation of this circular tomographic problem which is even more suggestive mathematically; we say a little about this just now, more later.

Assuming σ is even in y, we find our problem is equivalent to knowing the integral of σ along all semicircles centered on real axis in the upper half-plane $y \geq 0$. To be more precise, let us take any $\sigma(x, y)$ in the upper half-plane

and say we know its integrals along the same semicircles, and try to recover it. Replace $\sigma(x,y)$ by $\Sigma(x,y)/y$. Then what we are given is essentially

$$K(\xi,r) = \int_0^\pi \Sigma(\xi + r\cos\theta, r\sin\theta)\frac{d\theta}{\sin\theta}.$$

Thus we are given the integral of Σ along most geodesics in the Poincaré metric for the upper half-plane. The integrals along remaining geodesics, vertical rays in upper half-plane, can be gotten by simple limits.

We return to the original formulation. Considering $\lim_{r\to\infty} rK(y+r,r)$, we see that we can recover $\int_{-\infty}^{\infty}\sigma(x,y)dy$, i.e., the integral of σ along any vertical line. By inserting a line source, parallel to the x-axis, into the (x,y) plane, at a great height above the x-axis, we can remove, so to speak, the vertical DC component of $\sigma(x,y)$. While it is not absolutely necessary to do so, this normalization appears to make the integrals appearing in our work more manageable and probably facilitate numerics. So we may assume where necessary, that $\int_{-\infty}^{\infty}\sigma(x,y)dy \equiv 0$. The even character of $\sigma(x,y)$ then implies that $\int_0^\infty (x,y)dy \equiv 0$.

The DC component may be restored once the computation of the reduced σ is completed.

We now show how to invert the circular tomographic data. Let $\hat{\sigma}(\alpha,\beta)$ be the Fourier transform of σ, i.e.,

$$\hat{\sigma}(\alpha,\beta) = \frac{1}{4\pi^2}\int \sigma(x,y)e^{-i(\alpha x+\beta y)}dx\,dy.$$

Since σ is even in the 2nd variable, so also is $\hat{\sigma}$. If σ has all vertical DC components zero, then $\hat{\sigma}(\alpha,0)\equiv 0$.

We compute the circular Radon data for σ using its Fourier expression. Thus

$$\begin{aligned} K(\xi, r) &= \int \sigma(\xi + r\cos\theta, r\sin\theta)\, d\theta \\ &= \int d\alpha d\beta d\theta\, \hat{\sigma}(\alpha,\beta) e^{i\alpha\xi} e^{i(\alpha r\cos\theta + \beta r\sin\theta)} \\ &= \int d\alpha d\beta d\theta\, \hat{\sigma}(\alpha,\beta) e^{irR\cos(\theta-\phi) i\alpha\xi}, \end{aligned}$$

(where (R, ϕ) are polar coordinates of (α, β))

$$\begin{aligned} &= 2\pi \int d\alpha d\beta \hat{\sigma}(\alpha,\beta) e^{i\alpha\xi} J_o(r\sqrt{\alpha^2+\beta^2})\, d\alpha d\beta \\ &= 4\pi \int_{\beta>o} d\alpha d\beta\, \hat{\sigma}(\alpha,\beta)\, e^{i\alpha\xi} J_o(r\sqrt{\alpha^2+\beta^2}). \end{aligned}$$

Now make a substitution $u = \alpha, v = \sqrt{\alpha^2+\beta^2}$ valid in half-plane $\beta \geq 0$ and which sends it to the part of (u, v) plane with $v \geq |u|$. Continuing:

$$\begin{aligned} &= 4\pi \int_{v\geq|u|} du\, dv \frac{\hat{\sigma}(u, \sqrt{v^2-u^2})}{\sqrt{v^2-u^2}} e^{iu\xi} v J_o(rv) \\ &= \int_{v\geq 0} du\, dv H(u,v) e^{iu\xi}\, v\, J_o(rv) \end{aligned}$$

where

$$H(u,v) = \begin{cases} \frac{4\pi\hat{\sigma}(u,\sqrt{v^2-u^2})}{\sqrt{v^2-u^2}} & \text{if } v \geq |u| \\ 0 \text{ otherwise} \end{cases}.$$

The last integral above is a Fourier transform in the first variable, a zeroth-order Hankel in the second. (Notice that $H(u, v)$ is better behaved if σ has no vertical DC components.) Since the Hankel transform is self reciprocal,

$$H(u,v) = \frac{1}{2\pi} \int_{r>0} dr\, d\xi \quad rK(\xi, r) e^{-iu\xi} J_o(rv).$$

Since the integral above is zero for $0 \leq v < |u|$, there are consequential linear constraints on $K(\xi, r)$. It is not clear to us at this point how to use these constraints in practical situations.

Notice also that we have determined $\hat{\sigma}(\alpha, \beta)$ from $K(\xi, r)$. Thus we have, formally at least, inverted the circular Radon problem.

There is one more remark called for from a practical point of view. When we are imaging a small patch in the far field, $K(\xi, r)$ is zero for small r. Also $H(u, v)$ is zero for small v (relative to $|u|$). Accordingly, replacing $J_o(rv)$ by its first order asymptotics will be legitimate in some circumstances, and the inversion problem is an ordinary Fourier inversion.

We would now like to eliminate the Fourier transforms used thus far, and give the determination of $\sigma(x, y)$ directly by means of an integral kernel applied to $K(\xi, r)$. Fortunately this can be done, with an explicit kernel which is not too complicated functionally, and for which, owing to its special form, there is some hope that economical numerical procedures can be devised to effect the required integrations.

The method we will follow is a little circuitous, and so first we will sketch the steps and not go through the algebra necessary to give the final answer in closed form. We will give, however, Radon's closed-form solution of the problem cast in the geometry of the Poincare plane, though we do not compare it with our series solution. Finally after a change of notation, we will give a third and fourth form of the integral kernel, in closed form, which may be suitable for numerical implementation.

We begin with what we already know:

$$\hat{\sigma}(\alpha,\beta) = \frac{|\beta|}{8\pi^2}\int_{r>0} dr d\xi\ rK(\xi,r)J_o(r\sqrt{\alpha^2+\beta^2})e^{-i\alpha\xi},$$

valid for β positive, and by assumption on σ, for β negative as well. Also, of course,

$$\begin{aligned}\sigma(x,y) &= \int d\alpha d\beta\ \hat{\sigma}(\alpha,\beta)e^{i(x\alpha+y\beta)} \\ &= 2\int_{\beta>0} d\alpha d\beta\ \hat{\sigma}(\alpha,\beta)e^{ix\alpha}\cos(y\beta)\,.\end{aligned}$$

Thus:

$\sigma(x,\ y) = \frac{1}{4\pi^2}$

$\int_{\beta>0,\ r>0} d\alpha d\beta dr\ d\xi\ rK(\xi,r)J_o(r\sqrt{\alpha^2+\beta^2})\cdot e^{i\alpha(x-\xi)}(\cos y\beta)\beta$ and what interests us is:

$$\begin{aligned}&\int_{\beta>0} d\alpha d\beta(\beta)(\cos y\ \beta)\ J_o(r\sqrt{\alpha^2+\beta^2})e^{i\alpha(x-\xi)} \\ &= 2\int_{\alpha>0,\beta>0} d\alpha d\beta\beta\cos\ (y\ \beta)\cos\alpha(x-\xi)J_o(r\sqrt{\alpha^2+\beta^2}).\end{aligned}$$

To effect the last integration, we use the well-known fact:

$$J_o(r\sqrt{\alpha^2+\beta^2}) = J_o(r\alpha)\ J_o(r\beta) + 2\Sigma_{n=1}^{\infty}J_o(r\alpha)\ J_o(r\beta)$$

valid for $r,\alpha,\beta > 0$.

The double integral in question splits into the sum of the product of singles:

$$\int_{\alpha>0} d\alpha\ \cdot\cos\ \alpha(x-\xi)J_n(\alpha r)$$

and

$$\int_{\beta>0} d\beta\ \cdot\beta\cos(y\ \beta)\,J_n\,(\beta r).$$

The second equation above is a distribution. To handle it, we treat, rather than $\sigma(x,y)$, the quantity $\int_o^y \sigma(x,t)dt$. The second integral is then replaced by

$$\int_{\beta>0} \sin(y\,\beta)\, J_n(\beta\, r) d\beta.$$

The resultant integrals are now easily extracted from the known result

$$\begin{aligned} &\textstyle\int_o^\infty dt\ J_n(\mathrm{at})\ e^{ibt} \\ = \ & \frac{i^{n+1}a^n}{\sqrt{b^2-a^2}(b+\sqrt{b^2-a^2})^n} \end{aligned}$$

valid for $a, b > o$. If $b \geq a$, the positive square root is to be taken. If $b < a$, then $\sqrt{b^2-a^2} = i\sqrt{a^2-b^2}$. All that remains is to sum the series; fortunately, we only have geometric series to evaluate, so the sum can be effected. The final answer is basically a simple rational function of $x+\xi, r$, and y, with some quadractic irrationalities such as $\sqrt{y^2-r^2}$ and $\sqrt{(x+\xi)^2-r^2}$ thrown in.

We now return briefly to the description of our inversion problem set in the Poincaré upper half-plane. The Riemannian metric is $ds^2 = 4\frac{(dx^2+dy2)}{y^2}$, which has a constant curvature -1. The geodesics are semicircles centered on the x-axis, and vertical lines. The integral along a circular geodesic in the Poincaré metric of a function $\sigma(x,y)$ is

$$K(\xi,r) = 4\int_o^\pi d\theta \frac{\sigma(\xi + r\cos\theta, r\sin\theta)}{\sin\theta}.$$

In his 1917 paper, Radon gives explicitly, without proof, an inversion formula for this problem. The problem is, of course, a perfect analogue of his original—we know the integral of a function over all the geodesics of manifold; Radon remarks that the solution for the Poincaré plane has a striking analogy to that of the Euclidean plane.

Here is his inversion. Take all points in the Poincaré plane. Identify these points with the Euclidean half-plane for visualization (x, y) with $y > 0$. A circle on the Poincaré half-plane is the locus of points equidistant (in the Poincaré metric) from a fixed point (x, y). That circle appears on our Euclidean half-plane as a circle. We need a label to describe the radius of the circle; call it q. We can use the Poincaré metric or the Euclidean metric, it doesn't matter. It is also important that the center of the circle in our Euclidean half-plane is not (x, y), though (x, y) does lie inside the circle.

From the point (x, y) one and only one Poincaré geodesic emanates at angle θ with the x axis; call it $g(\theta)$. The geodesic $g(\theta)$ intersects the circle of radius q at a unique point p. (See Figure 2-2).

There is one and only one Poincaré geodesic $g(p)$ through p that is tangent to the circle q. Let $\sigma(p)$ be the integral of the function $\sigma(x, y)$ along $g(p)$. Now define a function F_q as the average of $\sigma(p)$ with respect to angle, θ. That is:

$$F_q = \frac{1}{2\pi} \int_0^{2\pi} \sigma(p) d\theta$$

where the point p in $\sigma(p)$ is the point on the circle defined by the geodesic $g(\theta)$.

Then according to Radon,

$$\sigma(x, y) = -\frac{1}{\pi} \int_o^{\infty} \frac{dF_q}{\sinh q}.$$

We have not written this answer out any more explicitly than above, nor have we compared it with the answer we derived earlier by different methods. The integral kernels may <u>not</u> be the <u>same</u>.

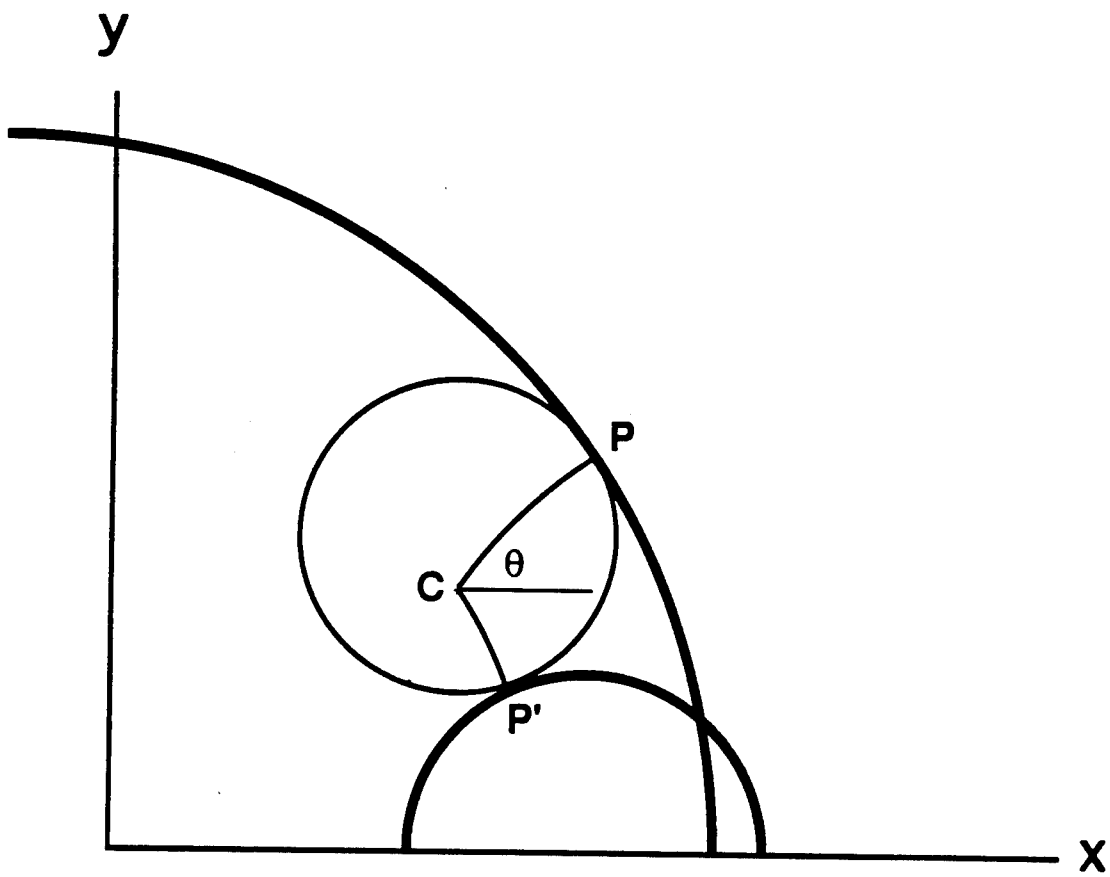

Figure 2-2. Visualization of a circle and geodesics that satisfy the Poincaré metric. All points on the circle are equidistant from the point C in the Poincaré metric. The deodesics from C to two points P and P' are shown. The heavy semicircles through points P and P' are the geodesics tangent to the circle at those points, and they are the curves along which the integral of the cross section is known.

As a matter of fact, a little more thought tends to suggest one should not work too hard to get the integral kernel at all, since it factors naturally into steps which are computationally easier to carry out. This we now explain.

The kernel of interest is (up to scale factor)

$$\int_0^\infty J_o(r\sqrt{\alpha^2+\beta^2})\,|\beta|\,e^{i\alpha(x-\xi)}e^{i\beta y}d\alpha d\beta.$$

Suppose we worry for the moment only about

$$\int J_o(r\sqrt{\alpha^2+\beta^2})\,e^{i\alpha(x-\xi)}\,e^{i\beta y}\,d\alpha d\beta.$$

The kernel we want can be gotten readily from the last by a differentiation with respect to y, followed by a Heaviside transformation in y.

The Heaviside transformation, a modified Hilbert transform, multiplies the positive spectrum by +1, the negative spectrum by -1, and is easily computed by an integral transform:

$$(Hf)(x) = \pm\frac{i}{\pi}\int\frac{f(x)-f(y)}{x-y}dy.$$

The choice of sign depends on how you normalize your Fourier transform. In practice, of course, the Heaviside transform H should be computed on the spectral side, by Fourier transform, multiplication by signum, and Fourier inversion.

So for our immediate purpose we have to compute the Fourier transform (2-D) of $J_o(r\sqrt{\alpha^2+\beta^2})$. Let us consider the distribution D_A which assigns to $f(x,y)$ the number

$$D_A f = \int_o^{2\pi} f(A\cos\theta, A\sin\theta)d\theta.$$

An easy computation (repeating ones we have already made), shows

$$D_A e^{i(\alpha x + \beta y)} = 2\pi J_o(A\sqrt{\alpha^2 + \beta^2}).$$

Hence the Fourier transform of $J_o(A\sqrt{\alpha^2 + \beta^2})$ is just $\frac{1}{4\pi^2} D_r$. We can now easily evaluate the integral

$$\int_{r>0} r\, K(\xi, r) D_r \;\; dr\; d\xi$$

through some care must be exercised in computing—the result is simply that the resulting distribution is a function, not a generalized function, and a simple one at that

$$\frac{1}{4\pi^2} \int_{-\infty}^{\infty} K(\xi,\, \sqrt{(x-\xi)^2 + y^2}) d\xi.$$

(The $\underline{r}$ in the original integral $\int r\, K(\xi, r)\;\; D_r$ is absorbed by polar to rectangular coordinate change.)

The integral above is easily parametrized:

$$\frac{|y|}{4\pi^2} \int_{-\infty}^{\infty} K(x\, +\, |y| \sin ht, |y| \cos ht) \cos ht\; dt.$$

Since it is one dimensional, it requires at brute force level $\underline{N}^3$ steps. The remaining differentiation and Heaviside transform need only $N^2 + N^2 \lim N$ steps, so the whole computation thus factored is order N^3.

We have just discovered a paper "An Inverse Method for the processing of synthetic aperture radar data" by H. Helbsten and L. E. Anderson, published in Inverse Problems 3 (1987) p. 111-129, published in the UK by IOP Publishers, Ltd, which has very substantial overlap with the formulas and points of view of this section and next, but which is less concerned with numerical implementation.

2.5 Analytic Inversion

The derivation of the last section now leads to a complete analytic inversion. We are concerned here only with the issue of avoiding the Fraunhofer or Fresnel approximation which can [5] affect the accuracy of phase recovery beyond all the other approximations generally made. Our result, in two forms, gives the complex reflectivity $\sigma(\vec{x})$ of a flat plane (with coordinates $\vec{x} = (x, y)$) as an integral of a two-dimensional kernel over the received signal S.

For any frequency component of the transmitted signal, the received signal at range R', where

$$R' = [(x - \xi)^2 + Y^2]^{1/2}, \tag{2-57}$$

is

$$S(t, R') = \int \frac{d^2x}{(R')^2} e^{i\omega(t-2R'/c)} \sigma(x, y). \tag{2-58}$$

Here ξ is the position along track of the SAR and

$$Y = (y^2 + H^2)^{1/2} \tag{2-59}$$

where H is the (constant) altitude of the SAR. It is trivial to go from Y to y, so from now on we will ignore this distinction and write y in place of Y in R'.

We apply a matched filter $\sim e^{-i\omega(t-2R/c)}$ to S in Equation (2-58), and integrate over ω to find (dropping a multiplicative factor)

$$S(R,\xi) = \int \frac{d^2x}{(R')^2}\delta(R-R').\sigma(x,y) \tag{2-60}$$

$$= R^{-1}\int d\theta\sigma(\xi + R\cos\theta, R\sin\theta)\,. \tag{2-61}$$

Here, by abuse of notation, we continue to denote the signal after matched filtering by S, and have written

$$x = \xi + R'\cos\theta, \quad y = R'\sin\theta \tag{2-62}$$

in the integral.

To deduce σ from S in Equation (2-61) is a tomographic problem, whose nature will be discussed more fully later. One way to proceed is to write $\sigma(\vec{x})$ as a Fourier transform:

$$\sigma(\vec{x}) = \frac{1}{(2\pi)^2}\int d^2k e^{i\vec{k}\cdot\vec{x}}\hat{\sigma}(\vec{k}). \tag{2-63}$$

Use Equation (2-63) in Equation (2-61) and do the integral over θ to find

$$S(R,\xi) = \frac{1}{2\pi R}\int d^2k J_o(kR)e^{i\xi k_x}\hat{\sigma}(\vec{k}) \tag{2-64}$$

where we have used the well-known expansion

$$e^{ikR\cos\alpha} = \Sigma\, i^N\, J_N(kR)e^{iN\alpha}. \tag{2-65}$$

Next, using the orthonormality relation

$$\int_0^\infty dRR\,J_o(kR)J_o(k'R) = k^{-1}\delta(k-k') \tag{2-66}$$

we show that

$$\begin{aligned} P(k,\xi) &\equiv \int dRR^2\, J_o(kR)S(R,\xi) \\ &= \frac{1}{2\pi}\int d\phi e^{ik\xi\cos\phi}\hat{\sigma}(k,\phi), \end{aligned} \tag{2-67}$$

where ϕ is the polar angle of $\vec{k}$ and the integral over the magnitude of k in Equation (2-64) has been done with the delta-function in Equation (2-66). Then we multiply $P(k,\xi)$ by $\exp(-ik\xi\cos\phi)$ and integrate over all ξ to generate another delta-function, coming to

$$\hat{\sigma}(k,\phi)+\hat{\sigma}(k,-\phi) = |k_y|\int dRR^2\int d\xi J_o(kR)e^{-i\xi k_x}S(R,\xi) \tag{2-68}$$

where

$$k_x = k\cos\phi, \quad k_y = k\sin\phi. \tag{2-69}$$

The reason for the appearance of two terms on the LHS of Equation (2-68) is that the delta-function coming from the integral over ξ is of the form $\delta(\cos\phi' - \cos\phi)$, with roots at $\phi = \pm\phi'$. In consequence, the inversion formula for $\hat{\sigma}$ picks up only the term even in k_y, which in real space means only the term in $\sigma(\vec{x})$ which is even in y survive. But our σ can always be made even in y (see Section 2.4)

Note that in extending the integrals over ω and ξ from $-\infty$ to ∞ means that we are ignoring an essential feature of real-world SAR, which is that SAR is band-limited both in fast time (corresponding to ω) and in slow time (ξ). But these are unessential complications for our purpose, as long as $\omega R/c$ and $\xi/\Delta x$ are both $\gg 1$ (Δx is the SAR's azimuthal resolution).

It remains to invert the Fourier transform in Equation (2-68), which we show can be written as a two-dimensional integral, by explicitly doing two

of the four integrations which result when Equation (2-68) is Fourier transformed. These integrals are not of the FFT type, and the computational burden at first glance appears to be $O(N^4)$, where N is the number of pixels corresponding to a typical scene linear span. However, we make the important observation that those purposes for which accurate phase information is needed (the motivation of this study is phase accuracy) can often be implemented in Fourier space, and that going to real space may be an unnecessary complication. For example, coherent change detection (of phase differences between two images of the same scene, displaced in time) can be implemented in Fourier space. In that case, the computational burden is only $O(N^2)$, to recover $\hat{\sigma}(\vec{k})$.

Inverting the Fourier transform has one minor complication: The appearance of $|k_y|$ rather than k_y in Equation (2-68). (If only k_y appeared, the inversion integral would be one dimensional.) One way to handle this is to write

$$|k_y| = lim_{\epsilon \to O+} \left(\frac{-i}{\pi}\right) k_y \int_{-\infty}^{\infty} du \, \frac{u e^{iUk_y}}{u^2 + \epsilon^2}. \tag{2-70}$$

Using this in Equation (2-68), along with the Fourier definition in Equation (2-63), yields

$$\sigma(\vec{x}) = \frac{-1}{4\pi^3} \frac{\partial}{\partial y} \int d^2k e^{i\vec{k}\cdot\vec{x}_s} \int R^2 dR \int d\xi \int \frac{du\, u}{u^2 + \epsilon^2} J_o(kR) S(R, \xi) \tag{2-71}$$

where

$$\vec{x}_s = (x - \xi, \, y + u) \tag{2-72}$$

and k_y has been replaced by $-i\partial/\partial y$.

The k-integral is the Fourier transform of a Bessel function:

$$\int \frac{d^2k}{(2\pi)^2} e^{i\vec{k}\cdot\vec{x}_s} J_o(kR) = \frac{1}{2\pi R}\delta(R - R_s) \tag{2-73}$$

$$R_s \equiv |\vec{x}_s|. \tag{2-74}$$

This immediately yields

$$\sigma(\vec{x}) = -\frac{1}{2\pi}^2 \frac{\partial}{\partial y} \int d\xi \int \frac{du\, u}{u^2 + \epsilon^2} R_s S(R_s, \xi). \tag{2-75}$$

Note that R_s depends on both ξ and u, via Equation (2-72).

One may also do the $\vec{k}$ integral in inverse-transforming (Equation (2-68)) directly, without use of Equation (2-70).

We have

$$\sigma(\vec{x}) = \frac{1}{8\pi}^2 \int d^2\, k\, |k_y| e^{i\vec{k}\cdot\vec{x}} \int dR R^2 \int d\xi\, J_o\,(kR) e^{-i\xi k_x} S(R, \xi). \tag{2-76}$$

The integral over k_x is found in e.g., Gradshtyen and Ryzhik (Section 6.677) and results in

$$\sigma(\vec{x}) = \frac{1}{(2\pi)^2} \int dk_y |k_y| e^{iyk_y} \int R^2 dR \int \frac{d\xi}{R_1} \cos(k_y R_1) S(R, \xi) \tag{2-77}$$

where

$$R_1 \equiv [R^2 - (x - \xi)^2]^{1/2} \tag{2-78}$$

and the integral in Equation (2-77) has support in R_1 real. The integral over k_y is elementary, but if (as before) the range of integration is infinite, it must be regularized; we do this by multiplying the integral by $e^{-\epsilon|k_y|}$ and find

$$\sigma(\vec{x}) = \frac{1}{(2\pi)^2} \frac{\partial}{\partial y} \int R^2 dR \int \frac{d\xi}{R_1} S(R, \xi) \left[\frac{y + R_1}{(y + R_1)^2 + \epsilon^2} + \frac{y + R_1}{(y - R_1)^2 + \epsilon^2} \right]. \tag{2-79}$$

This integral is the analytic inverse, and not, unfortunately a form of FFT. It should be, as for the case of exact solution by other integral kernels be studied carefully for numeric implementation. If some kernel has simpler enough form, clever numerical analysis may reduce the computation (possibly to an FFT). The experience of the CAT scene community may be helpful here.

A mathematical treatment of the exact inversion problem for imaging a spherical earth appears in Appendix C.

2.6 An Alternative to Polar Reformatting

In spotlight-mode SAR processing, data are collected (rectangular gridding on wave number side) from ground points lying in the frustum of a circular cone, polar gridding:

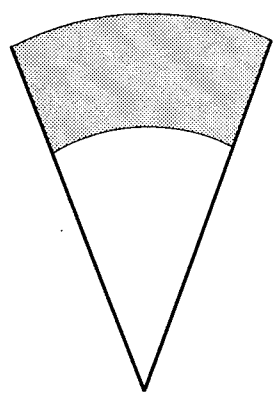

An intricate and costly numerical procedure is then used to interpolate the points in the polar grid to a rectangular format, so that FFTs may be used.

Can the polar reformatting be circumvented? We think it can, and from at least two points of view, and we believe that numerical work is saved even beyond that resulting from non-reformatting.

Here is the analytic setup.

$$\begin{aligned} F(\alpha,\beta) &= \int f(x,y)e^{i(\alpha x+\beta y)}dxdy \\ &= \int\int_{r\geq 0, 0\leq\theta\leq 2\pi} r\ f(r\cos\theta, r\sin\theta)e^{iRr\cos(\theta-\phi)}dr\ d\theta \\ \text{where}(\alpha,\beta) &= (R\cos\phi, R\sin\phi). \end{aligned}$$

From the known formula

$$e^{iz\cos\theta} = \sum_{n=-\infty}^{\infty} i^n J_n(z)e^{in\theta}$$

we get

$$F(R\cos\phi, R\sin\phi) = \sum_{-\infty}^{\infty} A_n(R)e^{in\phi}$$

where

$$A_n(R) = i^n \int r dr\ d\theta f(r\cos\theta, r\sin\theta)e^{-in\theta}J_n(rR).$$

The above is just the Fourier series expansion (for each fixed R) of the periodic function $F(R\cos\theta, R\sin\theta)$.

If we take the Fourier series expansion of $f(r\cos\theta, r\sin\theta)$ as

$$= \sum_{-\infty}^{\infty} a_n(r)e^{in\theta},$$

we have finally

$$A_n(R) = 2\pi i^n \int_0^\infty r\ a_n(r)\ J_n(rR)\ dr$$

which has, by the well-known inversion formulae for Hankel transforms, the solution

$$a_n(r) = \frac{1}{2\pi i^n}\int_0^\infty RA_n(R)J_n(rR)\ dR.$$

In actual practice, the function $f(r\cos\theta, r\sin\theta)$ is non-zero only for relative large r, and so the same is true for $a_n(r)$. Moreover, $J_n(z)$, for $n \neq 0$, vanishes at $z = 0$, and $J_n(z)$ for each n, including $n = 0$, has good asymptotics:

$$J_n(z) \approx \left(\frac{2}{\pi z}\right)^{1/2} \cos\left(z - \frac{n\pi}{2} - \frac{\pi}{4}\right).$$

Thus for R moderately large in magnitude

$$A_n(R) = 2\pi i^n \int_0^\infty r a_n(r) \frac{2^{1/2}\cos\left(rR - \frac{n\pi}{2} - \frac{\pi}{4}\right)}{\pi^{1/2} r^{1/2} R^{1/2}}\, dr,$$

which can be solved for $a_n(r)$ by 1-D FFT, or more appropriately, by using the Bessel asymptotics in the Hankel inversion formula, i.e.,

$$a_n(r) = \frac{1}{2\pi i^n} \int_0^\infty R A_n(R) J_n(rR) dR.$$

In the above formula use direct integration up to some reasonable R threshold, then replace $J_n(rR)$ by its asymptotics and use Fourier transform numerics over the remainder of the range of integration.

Some special treatment (more care) is needed for $n = 0$, (to get the DC component), because $J_0(z)$ is not small for small z, and so the contribution to the integral for $a_0(r)$ at small values of R is more significant.

Apart from special treatment for $n = 0$, and possibly small values of R, we have one FFT for each R range bin, and another for each frequency bin ϕ, looking altogether like one 2-D FFT.

From the conventional user's point of view, there may be two disadvantages—the received signal $F(\alpha, \beta)$ has to be polar formatted, and the ground reflectivity $f(x, y)$ is recovered on a polar grid.

This may not be so bad once you get used to it.

We want to show next that the method just described can be substantially improved in terms of numerical load. The improvement depends on the simple observation that the central angle, θ_0, of the viewed area is small. We will suppose, moreover, that θ_0 is an integral part of 2π, i.e., $\theta_0 = \frac{2\pi}{Q}$. For the sake of illustration, we suppose the geometric situation is:

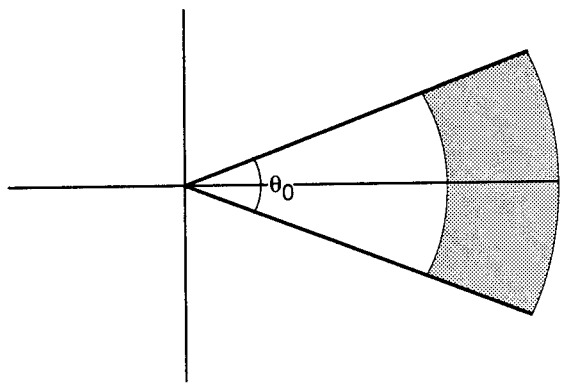

We expand $f(x, y)$, which is zero outside of shaded region as:

$$f(x,y) = \sum_{-\infty}^{\infty} a_n(r) e^{inQ\theta},$$

valid for θ satisfying $-\frac{\theta_0}{2} \leq \theta \leq \frac{\theta_0}{2}$.

For the received signal, we still have

$$\begin{aligned} F(\alpha, \beta) &= \int r f(r\cos\theta, r\sin\theta) e^{irR\cos(\theta-\phi)} dr\, d\theta \\ &= \int_{-\theta_0/2}^{\theta_0/2} d\theta \int_0^{\infty} r dr f(r\cos\theta, r\sin\theta) e^{irR\cos(\theta-\phi)}. \end{aligned}$$

While most of the Fourier coefficients of $F(R\cos\theta, R\sin\theta)$ are of little interest, one sees readily that

$$A_{nQ}(R) = i^n \int_0^{\infty} r a_n(r) J_{nQ}(rR) dr,$$

so we only need coefficients of F on a beat of Q to recover the a_n's.

Fortunately, an easy modification of FFT finds the coefficients on a beat of Q without finding others. One has only to wrap the function around itself and add. By this we mean to simply say that if

$$g(\theta) = \sum_{-\infty}^{\infty} C_n \, e^{in\theta},$$

then g is periodic with period 2π, then

$$G(\theta) = \frac{1}{Q} \sum_{n=0}^{Q-1} g\left(\frac{\theta}{Q} + \frac{2\pi n}{Q}\right)$$

is also periodic with period 2π and has C_{nQ} as its non-negligible Fourier components.

Thus, the restricted Fourier expansion of f has reduced the work to a Qth of the earlier approach.

2.7 Estimating the Correct Pixel Phase During SAR Processing

2.7.1 Phase Errors in Complex SAR Images

Fundamentally SAR images are complex, containing an amplitude and a phase for each pixel. In most SAR applications the amplitude of a pixel is squared and displayed as image intensity with the phase being ignored. The phase contains precise information on geometrical properties of a pixel

on scales of a fraction of the radar wavelength. As discussed in section 5.0, the phase of pixels can be used in many innovative ways, such as coherent change detection and topography estimation. Phase errors (instrumental and signal processing, systematic and stochastic) limit the usefulness of pixel phase information in exploiting SAR data. Smaller phase errors allow more complete exploitation of SAR data.

The principal issues that arise with regard to phase errors in SAR images can be summarized as follows:

1. What is the phase noise floor in a given SAR image?
2. What is the phase error budget, in terms of environmental, equipment, processing, etc. factors
3. What approximations in various imaging algorithms contribute to phase errors?
4. Which algorithms provide the best phase estimates?
5. What is the computational price of reducing phase errors?
6. What benefits flow from reduced phase errors?

To begin we consider the 'optimal' retrieval of a SAR image from a SAR signal data set. The process is illustrated schematically in Figure 1-1.

SAR image formation begins with the scene illuminated by the SAR in cross-track or range r and along-track or azimuth coordinate x. The track is the direction of the SAR platform. SAR data $d(x,t)$ is collected in terms

of time t and position along track x. The signal corresponding to a target at (r_o, x_o) is spread along the curve shown in the (x,t) or data coordinate system. An imaging or focusing algorithm takes the signal $d(x,t)$ and forms it into an image scene $u(x,r)$ that should be the radar image of the original scene from which the signal data were collected.

2.7.2 Optimal Time Domain Imaging

Bamler [6] compares a variety of SAR imaging algorithms with the optimal retrieval algorithm given by

$$u(x,r) = \int \int_{-\infty}^{\infty} d(x',t) h^*(x'-x, t - \frac{2r}{c}; r)\, dx'\, dt \qquad (2\text{-}80)$$

where x is distance along the SAR platform trajectory, r is range to the target, t is time delay of target echo and $d(x,t)$ is the range compressed SAR data as shown in Figure 1-1. The normalized point scatterer response (PSR) is

$$h(x,t;r) = \delta[t - \frac{2}{c}\Delta R(x;r)] e^{-j\omega_o \frac{2}{c}\Delta R(x;r)} \qquad (2\text{-}81)$$

where ΔR is the *range migration* given by $(R-r)$ where $R(x;r)$ is the range to a target, located at range r from the SAR platform trajectory, from a point x along the SAR platform trajectory. Thus, when the SAR is just passing the target, ΔR is zero.

To say that Equation (2-80) is the optimal time domain imaging formalism is something of an exaggeration since a number of assumptions have been made, e.g. the SAR trajectory is a straight line and constants have been disgarded. However, within these assumptions it is the best that can be done.

The point here is to establish a sensible standard with which to compare real algorithms – Equation (2-80) is Bamler's (1992) [6] standard.

One can see in Equation (2-80) the challenge of SAR processing in that h is both two dimensional and space invariant, i.e., h is a function of both x and r. A full two dimensional time domain correlation as expressed in Equation (2-80) would handle the challenge, but the computational demands are still too high for current computation capability.

2.7.3 Origins of Phase Errors

The phase of a pixel in a complex SAR image is accumulated as part of an integration or transform process and is thus generally data dependent. That is, phase errors depend on the scene being imaged. For example if Fourier transforms are used to perform correlation, then the final step is the inverse transform of

$$U(k_x, k_r) \approx D(k_x, \omega) H^*(k_x, \omega; r) \tag{2-82}$$

where k_x and k_r and ω are the transform variables corresponding to x, r and t. U, D and H^* are the transforms of the complex image, the data of Figure 1-1 and the transform of the PSR, h.

Fundamentally no current algorithm performs the optimal image formation processing of Equation (2-80). There are approximations in the kernel h^*, truncation of the range of integration as well as other short cuts in correlation and/or interpolation that impact the phase estimate for a given pixel. Below we will consider phase errors resulting from these causes, particularly

in the approximation of the phase of h^*. Interpolation errors are very important in polar reformatting schemes in which data are interpolated to a grid where the form of Equation (2-82) can be used directly.

2.7.4 Established Processing Schemes

Digital SAR processors come in a variety of types as illustrated in Figure 2-3. When any of these algorithms is implemented in software the process in evolutionary. For example, the SEASAT SAR processor at Jet Propulsion Laboratory evolved over more than a decade under the direction of J. C. Curlander (Curlander and McDonough, 1991) [7]. Image products appearing in the late 1980's were far superior to those of the early 1980's. Similar progress was made in the processor at the Royal Aircraft Establishment, Farnborough, UK (Barber, 1983, 1985) [8], [9]. Over time algorithms go through incremental improvement, incorporating some the ideas shown in Figure 1-1 and discussed below. However, most of the work in the 1980's was dedicated to the goal of improving intensity image quality, not the image phase that concerns us here. Hence, one should alway regard image phase with some suspicion until the quality of the phase output from a given processor is established.

We divide SAR algorithms into polar and rectangular types and their derivatives. Most of the variants are discussed briefly below and at more length in Bamler (1992) [6], Curlander and McDonough (1991) [7], Barber

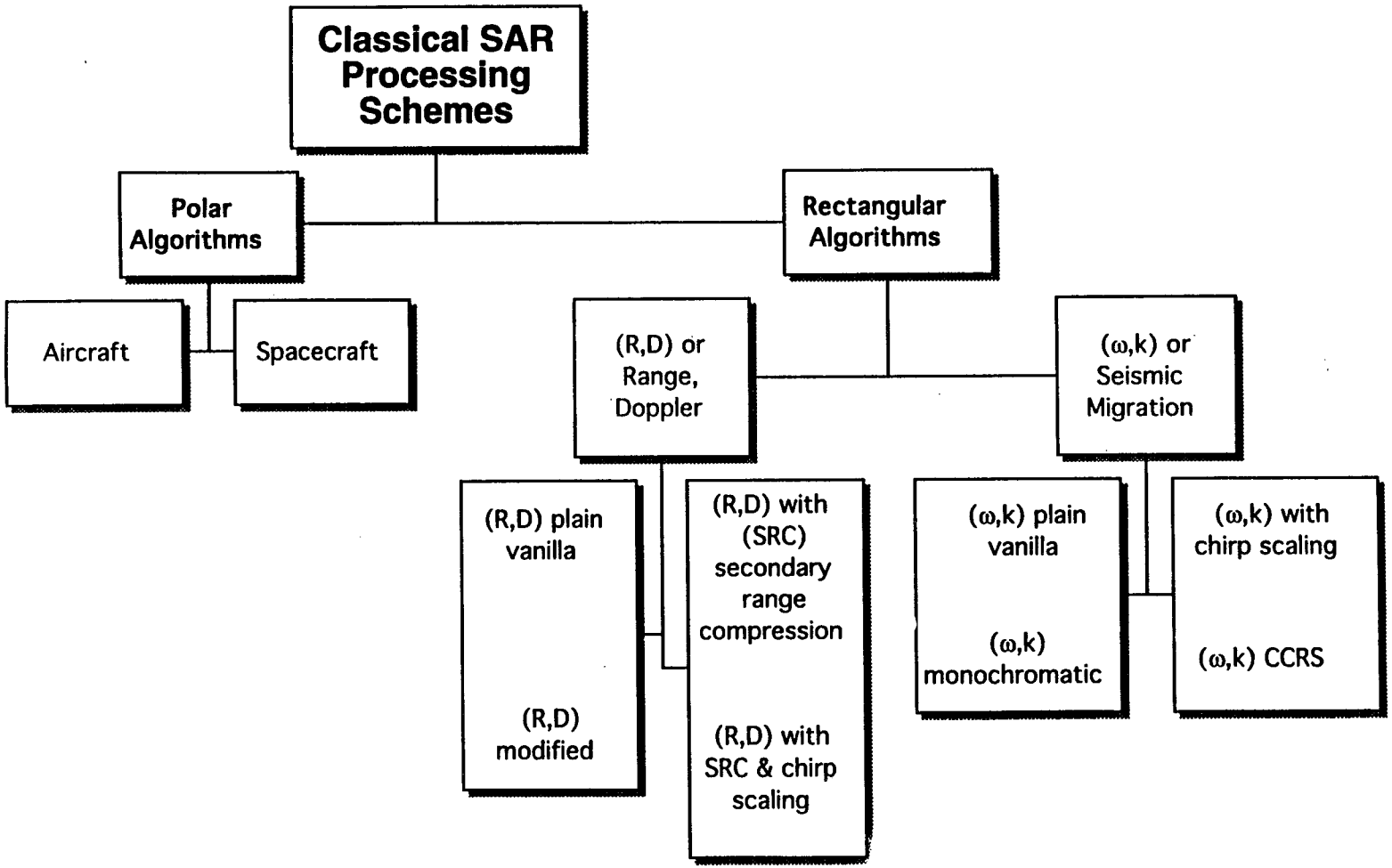

Figure 2-3. Schematic diagram of SAR Imaging Algorithms.

(1983, 1985) [8], [9] as well as other references, quoted here and in these publications. The several variants in each type correspond to the evolutionary improvement in digital SAR processors over the past decade or so.

Rectangular Algorithms

(R,D) or Range, Doppler: Range doppler algorithms have been the basis of most high quality digital SAR imaging processors since the days of SEASAT SAR. In this algorithm the two-dimensional correlation is done by two one-dimensional matched filter operations. The first performs the range compression (fast time) and the second operates in the Doppler domain created from the phase of the result of the first compression. Between the two is a range migration correction to flatten out the curvature of the data as shown in Figure 1-1. The basic process is shown schematically in Figure 2-4.

The range migration correction brings all the range cells corresponding to the curved data trajectories of Figure 1-1 into as single range line so that the azimuth compression filter can operate on them correctly. This is the equivalent of having the azimuth compression filter operate on the curved data path indicated in Figure 1-1. For spacecraft SAR data one generally needs to compensate for 'range walk' as well. This effect is due to the rotation of the Earth during the SAR integration time. In an inertial frame the Earth's surface at the equator is moving at 465 m/s. This step is a crucial one in maintaining accuracy in the final complex image $u(x, r)$. There are several ways of doing the range migration correction. The most straightforward way is a K_x dependent r shift, but this requires an interpolation that must be

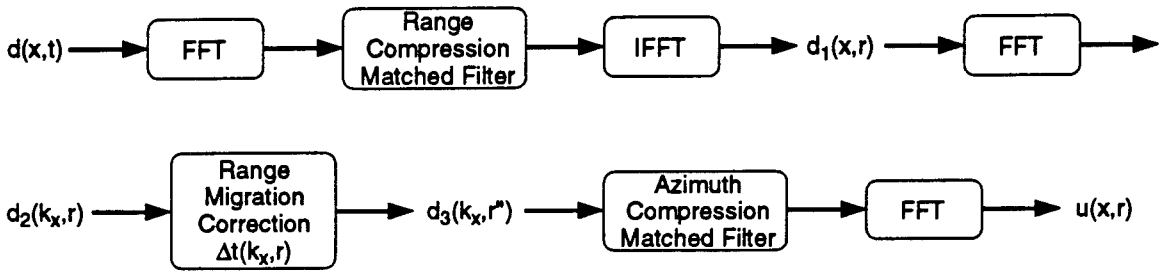

Figure 2-4. Schematic block diagram of data processing for the basic rectangular range-Doppler scheme of SAR image formation. In the range direction t=2r/c, so either t or r can be used as the range coordinate.

carried out accurately. If the iterpolation is too crude, 'ghost' smearing will appear in the final intensity image and phase distortion will be present.

As discussed below, one can perform the range migration step by first performing an FFT in azimuth (x), applying a compex correction factor to the resulting $d(k_x, t)$ data and then performing the range compression. This in effect adjusts the orignial chirp rates such that when range compression is done the range migration correction is performed along with range compression. This method is known as *chirp scaling* and avoids interpolation in the range migration correction step.

Phase Aberration: The more simple range-Doppler processing scheme produces a phase abberation with respect to the optimal scheme of Equation (2-80), i.e. an unwanted phase change of the form

$$exp\{jr\frac{c}{4}\frac{k_x^2}{\omega_o^2}\frac{\omega_o}{\omega+\omega_o}\} \tag{2-83}$$

where ωo is the carrier frequency (Bamler, 1992) [6]. Note that this phase change is a function of range, azimuthal wavenumber and wave frequency ω.

Secondary Range Compression: Since the phase aberration is known, it can be compensated for in the processing by adjusting the reference signal in the range chirp decompression. This process is called *secondary range compression* and can reduce the maximum aberration figures above by a factor of two or more using a convenient approximation to Equation (2-83). In the SEASAT and ERS-1 cases to 0.75 and 0.03 radians respectively (Bamler, 1992) [6]. This correction is one of the step-by-step fixes that have been done in the evolution of SAR processors, as discussed above.

Other Range-Doppler Algorithm Modifications

Secondary range compression is but one of a number of methods of correcting for the phase aberration of Equation (2-83) and the residual error after secondary range compression. We list a selection of these below:

1. Correction for Equation (2-83) in the (k_x, ω) domain (Chang et al., 1989) [10].

2. Correction for Equation (2-83) by interpolation in the (k_x, r) domain during the range migration correction procedure (Wong and Cumming, 1989 and Smith, 1991) [11], [12].

Range-Doppler processing can be adapted by the above and other schemes to give very accurate phase estimates, but at the cost of increased computation time. Ultimately one could provide a separate range migration correction and azimuth compression filter for each output pixel. The work mentioned above as well as much more is aimed at achieving sufficiently accurate complex images at the least computational cost. As we shall see in section 3.0 of this report, computation capabilities, especially using application specific integrated circuits, are adequate today for processing required images with full phase correction.

Wavenumber Domain (ω, k) Processing

This approach to processing grew out of seismic migration processing ideas in geophysics (Rocca, 1987) [13]. It was originally based on wave equation techniques, as is the seismic processing analog; but Bamler (1992) [6]

has shown that the results can be derived independent of the use of the wave equation. The basic approach, as shown in Figure 2-5, can be summarized as follows:

1. 2D Fourier transform of the input data (x, t) into the wavenumber domain (k_x, ω)

2. A change of variables from ω to k_r using

$$\omega = (c/2)\{[k_r + (2\omega_o/c)]^2 + k_x 2]^{0.5} - \omega_o.$$

   This step, called a Stolt mapping, takes care of the range migration problem.

3. 2D inverse Fourier transform to go from the wavenumber domain (k_x, k_r) back to the slant range plane (x, r) image.

This method is as "exact" as the "exact" form of the range-Doppler formulation. The two main drawbacks noted by Bamler (1992) [6] are that the change of variable must be done very accurately and that the interpolation implicit to the mapping must be very exact. Also large Doppler centroid variations in range or azimuth may require special effort.

2.7.5 Polar Algorithms

Polar algorithms rely on transforming from the input data space into a coordinate system such that image formation is simply a Fourier transform. This formulation is very useful for spotlight mode data. Phase errors in

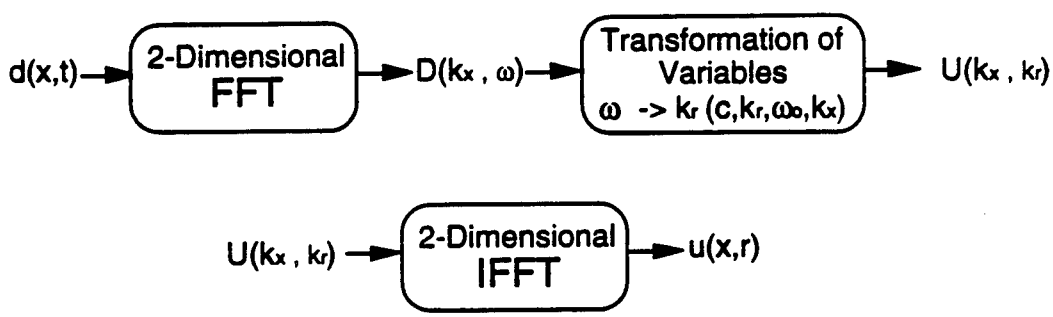

Figure 2-5. Schematic diagram of wavenumber domain processor.

this algorithm depend on the interpolation or reindexing step. There are a wide variety of interpolation options and the dependence of phase errors and little information is available on the relative performance of different choices. Further information on the general aspects of the algorithm are given by Curlander and McDonough (1991) [7].

2.7.6 Summary and Conclusions

Accurate pixel phase is essential to advanced exploitation of SAR data, coherent change detection, topographic mapping and motion detection. As phase accuracy is increased, further exploitation arenas will be opened, e.g. phase scintillation by convective plumes in the lower atmosphere. Given this importance it is necessary to emphasize pixel phase fidelity in future algorithm development goals and system specifications. Two ways of testing the phase fidelity are as follows:

1. Injection of known signals into an existing SAR signal data set and observe the rendering of the test signal in the SAR complex image
2. Field observation of vibrating targets with known amplitude and phase structure.

It appears clear that both rectangular and polar algorithms are capable of producing complex SAR images with low phase distortion. The complexity of the implementation of these algorithms makes a priori evaluation difficult. Thus, we recommend that benchmark tests be run between competing

algorithms using the testing methods above. Such competitions should be assessed on phase error coupled with wide applicability. Further it is necessary to construct a phase error budget including phase errors caused by propagation, e.g. scintillation, and target phenomena, e.g. moving trees or brush. There may also be improvements that can be made in terms of phase error reduction in SAR hardware electronics.

2.8 Atmospheric and Ionospheric Propagation

The natural environment modifies the phase and amplitude of a propagating electromagnetic wave because of variability in refractive index. There are two altitude regions of variability that are important for SAR: the ionosphere at a typical altitude of 250 km, with a thickness of roughly 50 km, and the lower atmosphere, from the ground to about 10 km (roughly a scale height). See Figure 2-6. Clearly the ionosphere is important only for space-based SAR.

It is noteworthy that books and review articles on SAR often do not mention these effects at all, not even to give a rough estimate to show whether they can be neglected [14]. For this reason, the following section will be introductory in nature; its main purpose will be to show quantitatively that the effect of the ionosphere on space-based SAR is expected to be substantial under many (though not all) different conditions, and that effects of the neutral atmosphere will be less important. SAR may be used as a tool to measure both ionosphere and atmosphere; that topic is covered in Section 5.2.4, which will use the formulas developed in this section.

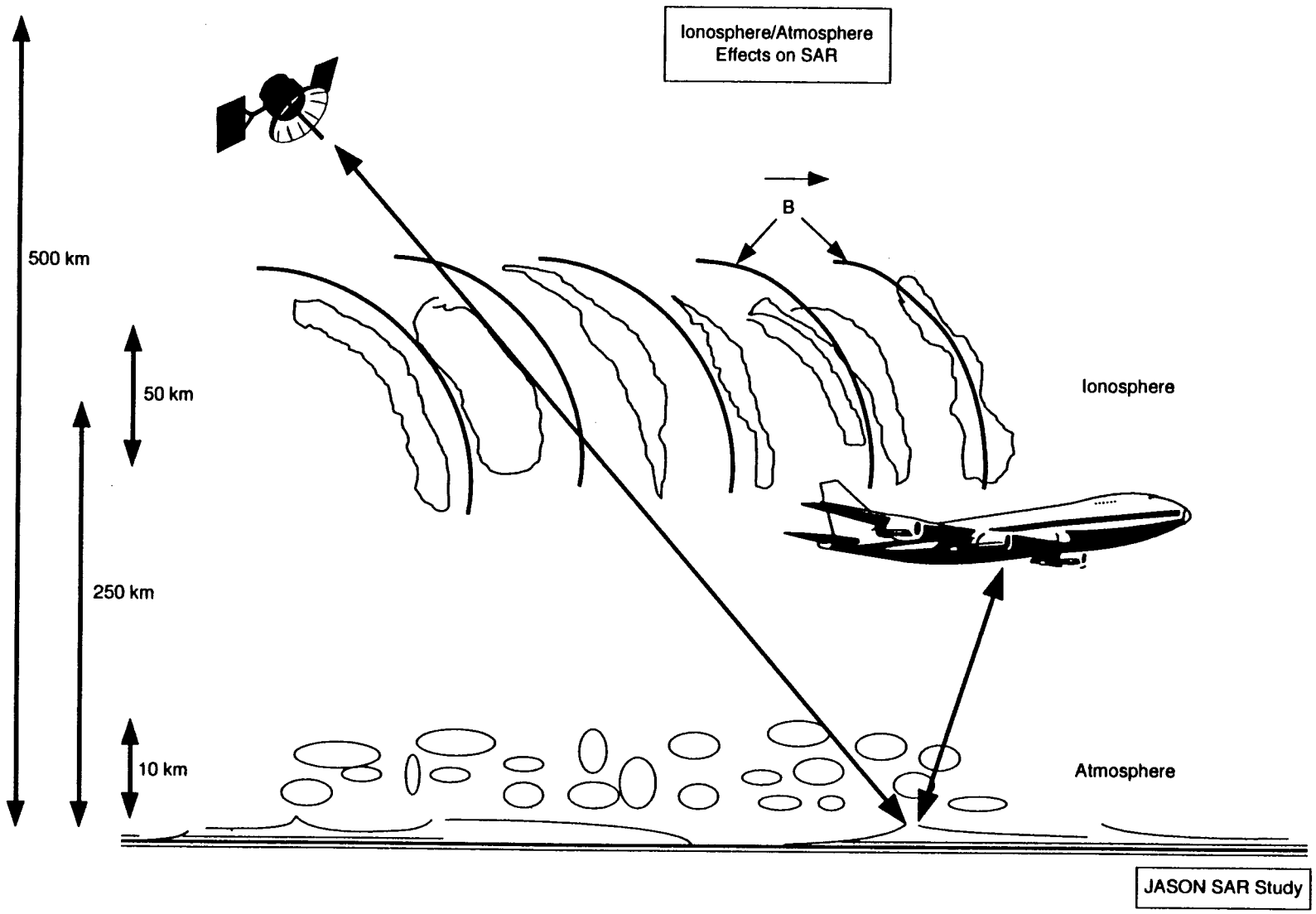

Figure 2-6. Ionosphere/atmosphere effects on SAR.

2.8.1 Ionospheric Phase Fluctuations

For the purposes of this report, the ionosphere is a region of space surrounding the earth in which electrons (and ions) exist at significant densities. A typical density is $N = 10^6$ cm^{-3}, with much higher densities in the auroral zones surrounding the poles [15]. Within this belt of electrons, the density has strong variability, and since this variability aligns with the earth's magnetic field, the variability is called "striations." To a good approximation the variability can be given in terms of a two-dimensional spectrum, where the two dimensions are transverse to the local magnetic field [16].

The refractive index n is expressed in terms of the frequency f of the propagating EM wave and the plasma frequency f_p, which in turn is expressed in terms of the electron density:

$$n - 1 = -(\frac{f}{f_p})^2 \tag{2-84}$$

$$f_p = \frac{1}{2\pi}(\frac{Ne^2}{m\epsilon_0})^{1/2} = 9\,\mathrm{KHz}\,(\sqrt{\mathrm{N}}) \tag{2-85}$$

where in the last expression the electron density N must be in number per cubic centimeter.

Since $n - 1$ is proportional to N, the fluctuations in the refractive index are also proportional to N. In many instances the fluctuations have been measured to be nearly 100 percent of the mean of $n - 1$; we will make that assumption for numerical evaluations. We define the deviation of the

refractive index from its mean as μ; the rms value of μ (for 100 percent fluctuations) is then

$$\mu_{rms} = C\lambda^2 \tag{2-86}$$

where the constant $C = (10^{-13}\,\text{cm})\,\text{N}$. Thus $C = 10^{-7}\ \text{cm}^{-2}$ for $N = 10^6\ \text{cm}^{-3}$.

The spectrum of refractive-index fluctuations can thus be directly related to the spectrum of electron-density fluctuations. We will deal directly with μ from here on. The spectrum of μ may be written as a function of a two-dimensional wavevector $\vec{\kappa}$ with components κ_1 and κ_2. The spectrum is usually expressed in terms of a power law, and a close-enough approximation for our estimates is to write: [15]

$$S(\vec{\kappa}) = \frac{A}{({\kappa_1}^2 + {\kappa_1}^2)^2}. \tag{2-87}$$

The normalization constant A is set by requiring the double integral of the spectrum to equal the variance. We set the lower limit of each wavenumber component to κ_{min}, and find that

$$A = \frac{3}{8}\kappa_{min}^2 C^2 \lambda^4. \tag{2-88}$$

The phase fluctuation of a wave traversing a medium with refractive index fluctuation $\mu(\vec{x})$ is

$$\phi = k\int_0^R \mu(x)dx \tag{2-89}$$

where the integral is along the trajectory of propagation. The variance of the phase fluctuation is: [17]

$$\langle\phi^2\rangle = k^2\int_0^R dx \int d\kappa_1 S(\kappa_1, \kappa_2 = 0). \tag{2-90}$$

Doing the above integration approximately, we find:

$$\langle \phi^2 \rangle = \pi^2 C^2 L \kappa_{min}^{-1} \lambda^2 \tag{2-91}$$

where L is the thickness of the ionosphere. Taking $L = 50\,\text{km}$, $\kappa_{min} = 2\pi/10\,\text{km}$, and $\lambda = 1\,\text{cm}$, we find $\phi_{rms} = 0.3\,\text{radians}$, or $0.05\,\text{cycles}$. *The phase fluctuation as a number of cycles is proportional to the wavelength.* The following table gives typical values of phase fluctuations induced by the ionosphere. The column labeled "min" is the result of the above calculation. The column labeled "max" is just a factor of ten larger, to account for two important effects that are relatively common. First, the minimum calculation assumed the radar wave traversed the ionosphere in a direction perpendicular to the earth's magnetic field. Any other angle will give a larger value. In particular, if the radar is pointed along the magnetic field line, a very large factor can result. Second, the auroral zone in polar latitudes has electron densities (and fluctuations) that are an order-of-magnitude larger than in temperate latitudes.

f	λ	ϕ_{rms}(min)	ϕ_{rms}(max)
GHz	cm	cycles	cycles
30	1	0.05	0.5
10	3	0.15	1.5
3	10	0.5	5
1	30	1.5	15

We note that the table indicates that SEASAT ($\lambda = 24$ cm) would have a cycle of phase fluctuation almost all the time. We have not looked at SEASAT data to evaluate these effects. Others have looked at some ionospheric SAR effects in the context of SEASAT, but they concentrated on the question of transverse resolution rather than change detection or other

sensitive topography measurement [18]. The characteristics of these phase fluctuations are that they have horizontal scales of 10 km and smaller, and that their intrinsic time scales are a few seconds to a minute. (For our model spectrum, the spectrum of phase fluctuations will behave like κ^{-4}, or ω^{-4} for a temporal spectrum.) A satellite at 500-km altitude creating a synthetic aperture of length 10 km will be looking at a specific pixel through a window of the ionosphere that is about 5 km wide, and it will traverse this window in about 2 s. Thus the typical integration times and altitudes of satellites place them in a vulnerable position for ionospheric effects.

A very specific application that might be affected by the ionosphere is change detection, where two radars, or two passes of the same radar, are used to develop an interferogram: a picture of the phase difference between the two cases [52]. This phase difference is translated directly into a topography height difference. If two passes are used, then the ionospheric phase contributions to the two passes are uncorrelated, and there will be a false topography generated from the ionospheric phase. However, if two radars are separated by a small distance (say 100 m) then the ionospheric phases in the two radars are correlated strongly, and the difference will have a contribution that is much less than the total ionospheric phase on one of them.

2.8.2 Ionospheric Amplitude Fluctuations

Waves traversing a random medium develop amplitude fluctuations after they have propagated a finite distance. The accumulated refractive-index

fluctuation directly becomes the final phase fluctuation. The amplitude fluctuation, however, is controlled by the second derivative of the refractive-index fluctuation, because the physical process of importance is focussing and defocussing, like moving through a series of lenses. An important scale in this problem is the **Fresnel length** given by

$$R_f = \sqrt{\frac{R}{k}} \tag{2-92}$$

where R is the distance from the ionosphere to the ground. In our case

$$R_f = 200\,\mathrm{m}^{1/2}\lambda^{1/2}. \tag{2-93}$$

The log-amplitude fluctuation is denoted by χ, and the expression for the variance of χ is: [20]

$$\langle\chi^2\rangle = 2k^2 \int dx \int d\kappa_1 S(\kappa_1, \kappa_2 = 0)\, \sin^2(\frac{\kappa_1^2 R_f}{k}). \tag{2-94}$$

By taking the ratio of amplitude to phase fluctuations, we can cancel out dependences and achieve a simple relation:

$$\frac{\langle\chi^2\rangle}{\langle\phi^2\rangle} = R^{3/4}\, k^{9/4}\, \kappa_{\mathrm{min}}^3 \tag{2-95}$$

which evaluates to an incredibly small 10^{-11}, which is completely negligible.

2.8.3 Tropospheric Phase Fluctuations

The troposphere is the 10 km of atmosphere that is closest to the ground. This region has fluctuations caused by many physical processes, particularly water vapor and clouds. The refractive index difference from unity is given

in terms of the pressure p in millibars, the temperature T in Kelvin and the specific humidity s in grams of water per kilogram of air: [17]

$$\mu = 10^{-6} p (\frac{78}{T} + \frac{600s}{T^2}). \tag{2-96}$$

The relative humidity h is given by:

$$h = spe^{-2360/T}. \tag{2-97}$$

For example, if $T = 300$ K and $h = 50\%$, then $\mu = 3 \times 10^{-4}$.

The variability in the neutral atmosphere is typically a few percent of the mean; therefore we have

$$\mu_{rms} = 10^{-5}. \tag{2-98}$$

The outer scales of atmospheric fluctuations vary from 1000 m down to centimeters. The spectrum of fluctuations may be taken as Kolmogorov turbulence for an estimate which works well in many places [20]. The refractive-index fluctuations are characterized by a structure function:

$$\langle(\mu(r) - \mu(0))^2\rangle = C_n^2 r^{2/3}. \tag{2-99}$$

An outer scale of L_0 results in a phase variance of:

$$\langle\phi^2\rangle = k^2 L C_n^2 L_0^{5/3}. \tag{2-100}$$

In this case we will estimate L by 5 km and L_0 by 100 m, with typical values of ${C_n}^2$ near the ground being about $10^{-13}\,\mathrm{m}^{-2/3}$. We should note here

that C_n^2 varies by several orders of magnitude (especially between day and night). Our estimate gives

$$\phi_{rms} = \frac{0.7\text{cm}}{\lambda}. \tag{2-101}$$

We see that unlike the ionospheric case, the neutral atmosphere effect is strongest at small wavelength, decreasing for the longer wavelengths. This is because the refractive index is independent of wavelength, so that the cumulative effect is a fixed length, which is a smaller and smaller fraction of a wavelength as the wavelength increases.

The effect at 1 cm is only 0.1 cycles, but we must remember that a region of highly variable weather can easily have turbulent strengths that are one hundred times larger, which would yield an rms value ten times larger.

2.8.4 Tropospheric Amplitude Fluctuations

The theory of waves through turbulence yields an equation for the amplitude fluctuations: [20]

$$\langle \chi^2 \rangle = C_n^2 k^{7/6} L^{11/6} \tag{2-102}$$

and this evaluates to a small number (10^{-3}).

2.8.5 Effects on SAR (Change Detection)

The effect of a typical ionosphere is to vary the phase of the returns from a given pixel by about a cycle with a correlation length (along the radar track) of $\sim$ 10 km. (The ionosphere has negligible effect on the intensity of the received signal.) The intensity of a standard pixel comes from a sum over $\sim$ 100 resolution pixels, each of which has random phase — another random phase from the ionosphere doesn't matter.

In change detection, on the other hand, the phase difference from one pass to another is measured resolution pixel by resolution pixel. Then the average of that difference is taken over 10-100 of these pixels. Now the ionosphere enters directly to ruin the phase difference, because it causes a variation of a cycle or more that is not correlated geometrically with a topographic change.

It would be of interest to numerically simulate this effect to see how it projects onto apparent topography. Since the ionosphere is at $\sim$ 200 km altitude and satellites are typically at 400-500 km, the projection may still yield an apparent topography, with a magnification factor.

If change detection were important, and ionospheric effects were anywhere from significant to catastropic, the ionospheric effect can easily be removed from the data in the early stages. The means for doing this are contained in normal SAR hardware, and only require software modifications. The basic physics that allows this correction is the dependence on wavelength of index of refraction of the ionosphere. As a result, two different frequencies have

different travel times through the ionosphere, and this difference can be measured. The two frequencies can be realized by dividing the bandwidth into two parts.

The extra computation to carry out this correction should be small compared with the normal SAR computational load. The calculations need to be done only for a few pixels for each square kilometer of the ionosphere. However, if the calculations are <u>not</u> done, change detection could fail catastrophically.

3 PARALLEL PROCESSING

3.1 Introduction

There are two aspects to the parallel processing of SAR images. The first is to cast the SAR image forming algorithms as given in the previous chapter into parallel form. Then these algorithms must be coded and compiled for each particular parallel-machine architecture. SAR image-formation is particularly blessed in that all the steps are naturally embarrassingly parallel. This is because SAR image formation is fundamentally a linear process (so that separately computed parts can be simply summed) or a very local process. The most difficult step to parallize appears to be the two dimensional (2D) FFT which is easily parallelized, although the "corner-turn" (matrix transpose) operation does require massive, complex data reorganization in parallel computers. Because the 2D FFT seems to be the most difficult step in the parallel computation of SAR image formation, we have focused upon it to determine how suitable Massively Parallel Computing Systems are for SAR computation.

3.2 Evaluation of MPCs for SAR Computation

As part of the study of SAR techniques and applications, we investigated the suitability of massively parallel processors (MPCs) for carrying out SAR

calculations. In particular, we evaluated several commercially available systems to determine whether recent advances in general-purpose parallel computers would allow these systems to be used for routine processing of SAR images. The conclusions were:

1. General-purpose MPCs are commercially available with sufficient capability for production SAR processing. Moderate size systems (64 processors) can process on average SAR image in one minute or less. Large systems (1024 processors) can process one image every few seconds.

2. Given current trends in microprocessor performance and interconnection technology, significant improvement (x10) is expected on a 3–4 year timescale.

3. Large general-purpose parallel computers can enable new uses of SAR data by allowing development and testing of computationally intensive SAR analysis algorithms.

3.3 Approach

To evaluate current-generation MPCs, we chose a benchmark SAR computation: calculation of a 16k $\times$ 16k complex SAR image. For simplicity the calculation was taken to be a 2-D FFT: an initial set of 16k 1-dimensional FFTs (range), followed by a transpose operation (corner turn), and completed by a second set of 16k 1-D FFTs (azimuth). Input data was assumed to be $\geq$ 8-bit and the computation to have $\geq$ 24-bit accumulation precision.

The 2-D FFT computation is the computationally intensive component of many standard SAR imaging algorithms, including SAR "spotlight" imaging, and so-called $\omega - k$ algorithms. Such imaging algorithms require phase correction or interpolation in addition to the 2-D FFT. Thus, although realistic production SAR processing involves more calculation than the simple benchmark (typically by a factor of 2–3), any system showing suitable performance on the benchmark problem is expected to show reasonable performance on a full production algorithm.

As a reference, a 100% efficient parallel computer that can perform the benchmark calculation in 10 s has the following performance characteristics:

- 4 GOPS total processor speed
- 2 GByte memory
- 10 GByte/s processor-memory bandwidth
- 600 MByte/s inter-processor bisection bandwidth

Commercially available systems, having less than 100% efficiency, will require larger peak processor speeds, memory, and bandwidth than the reference configuration above. For this study we generally assumed 50% peak speed in floating point and instructions for all systems studied. Typical performance varies from 25-60% depending on architecture, coding, and optimization.

3.3.1 Evaluation of Systems

Several specific commercial systems were studied. The intent was not to choose the "best" commercial system, but rather to identify "existence proofs" of SAR processing capability. The following systems were studied:

- General Purpose MIMD MPCs

- CM-5 [Sparc mP - Fat tree]

- Cray T3D [Alpha μP - 3-D Torus]

- nCUBE/2s [nCUBE μP - Hypercube]

- Paragon [i860$\times$P μP - 2-D Mesh]

- SIMD MPCs

- IBM/Execube [closely coupled processor/memory]

- Maspar [fine-grained commercial SIMD]

Table 3.1 gives the characteristics of the systems studied. The terms used in these and following tables are:

N_p		Number of processing elements
r_{clock}	(MHz)	Processor clock speed
r_{ips}	(Mips)	Peak instructions per second per processor
R_{ips}	(Gips)	Total instructions per second (estimated)
r_{flops}	(Mflops)	Peak floating point operations per second per processor
R_{flops}	(Gflops)	Floating point operations per second per partition (estimated)
s_{mem}	(MB)	Main memory per processor
s_{cache}	(KB)	Cache memory per processor
S_{mem}	(GB)	Total memory
b_{mem}	(MB)	Memory bandwidth per processor
B_{mem}	(GB/s)	Total memory bandwidth
b_{com}	(MB/s)	Communication bandwidth per processor
B_{com}	(GB/s)	Bisection bandwidth
$B_{I/O}$	(GB/s)	Total I/O bandwidth
T_{lat}	(ms)	Maximum set up time for zero-length message

Table 3.1. System Characteristics

	N_p	R_{ips}	R_{flops}	S_{mem}	B_{mem}	B_{com}	T_{lat}
CM-5	64	4.1	4.1	4.1	33	0.3	5
Cray-MPC	64	9.6	4.1	4.1	(50)	(> 15.0)	-
nCUBE/2s	1024	15.4	4.3	4.1	102	2.9	12
Paragon	64	1.6	3.2	4.1	26	1.6	5
IBM/Execube	8000	32.0	N/A	4.1	1600	5.1	-
Maspar	16000	2.4	3.2	1.0	20	0.6	-
Reference		[4.2]	[4.2]	2.0	10	0.6 (Estimate) [fp or int OK]	

In each case, the number of processors was chosen to give sufficient memory to carry out the required calculations (except for the Maspar system, which used the largest possible configuration). Floating point FFT calculations were assumed. Table 3.1 also contains the 100% efficient configuration for reference.

Table 3.2. Benchmark Times

CM-5	64 processor	$\sim$ 20 s
nCUBE/2	1024 processor	$\sim$ 40 s
Paragon	64 processor	$\sim$ 30 s

Vendors were asked to provide times for calculation of the benchmark problem. Table 3.2 gives the results of some of the benchmark calculations. The times are indicative of typical achievable speeds, and not necessarily optimized performance. With optimization, calculation time on the benchmark problem could be expected to improve. We therefore conclude that currently available moderate-size MPCs can compute a 16k $\times$ 16k SAR image with an average processing on the order of a few times 10 seconds. Large systems with 1024 fast processors can reduce the average processing time per image to a few seconds.

3.3.2 Future Trends

To evaluate future trends in commercial MPCs, we evaluated current processor characteristics (circa mid-1993) and extrapolated performance improvements to the year 2000. Table 3.3 gives the characteristics of several current microprocessors.

Table 3.4 extrapolates microprocessor characteristics from current (1993) to the year 2000. Based on the extrapolation of a factor of 4 improvement

Table 3.3. Processor Characteristics

	r_{ips}	r_{flops}	r_{clock}	s_{mem}	s_{cache}	b_{mem}	b_{com}
Alpha	300	150	150	64	8	800	300
Execube	8×0.5	N/A	-	8×0.064	N/A	8×25	0.6
i860XP	42	100	50	64	16	400	200
Maspar	0.3	0.4	12.5	0.064	N/A	1.25	1.25
nCUBE/2s	15	4.2	25	64	-	100	78
Sparc+Vector	128	128	32	128	64	512	20

Table 3.4. Extrapolated Performance of Processors

	r_{ips}	r_{flops}	r_{clock}	s_{cache}	b_{mem}	b_{com}
1993	200	100	100	64	16	400
1997	800	400	200	256	128	800
2000	3200	1600	400	1024	512	1600

by 1997 and a further factor of 4 improvement by 2000, the number of processors needed to calculate a 16k × 16k SAR image in 10 s will drop to 16 by about 1997 and to 4 by about the year 2000. As multiple-CPU workstations are becoming common it is likely that by 2000, SAR processing will be possible on a high-end modestly parallel workstation. Alternatively, moderate-size parallel systems of 64 processors with 100 Giga-op processing speeds and 8 Gigabytes or larger memory will be available in the time frame of the year 2000. Such systems will have the ability to analyze many images simultaneously with average processing times of less than 1 s, or will have the possibility of carrying out more advanced calculations on considerably larger images.

The key issue for future MPCs will not be processor speed, but rather memory cost and I/O performance, which will likely not experience the same improvement in cost/performance as processor speed. Although the memory requirement will likely drive total system costs, increased processor speed will allow more operations per byte of data, thus enabling use of computationally intensive algorithms, with a corresponding improvement in image fidelity. I/O performance will also be a critical issue. At one image per 10 s, the 4-processor system of the year 2000 mentioned above will require an I/O bandwidth of $2 \times 2 \times 256$ MB/10s (2 bytes per image, times 2 for read/write), or about 100 MByte/s I/O capability with 50 MB/s of archival storage bandwidth. Such I/O capacity is available commercially now, but will likely be a significant fraction of total system cost for a 4-processor system in the year 2000.

3.4 Custom SAR Processors

In this section, the memory, bandwidth, and processing requirements of the FFT portion of a SAR calculation are calculated. The silicon area required to support these requirements is determined and some alternative organizations are explored.

This study indicates that a special-purpose SAR processor constructed from custom LSI processor chips and standard DRAM chips with a total parts cost of less than $100K can generate a 16K $\times$ 16K SAR image in 1 s. The cost of such a machine is dominated by the cost of the memory to hold the problem ($52K). Thus cost is not significantly reduced by increasing latency.

Cost increases gradually as processors are added to reduce latency, T, until at $T = 0.1$ s the problem becomes memory bandwidth limited and cost goes as $1/T$. At $T = 8$ ms, the problem becomes communication bandwidth limited and cost goes as $1/T^{1.5}$. A practical lower bound on latency with modern technology is $T = 100\mu$s.

A special-purpose processor using commercial, off-the-shelf FFT chips can achieve performance similar to a full custom design at a somewhat higher parts cost. However, the design complexity of the "glue" required to interface off-the-shelf parts is comparable to the design complexity of the full-custom machine. Thus there is little advantage to using off-the-shelf parts.

A 16K $\times$ 16K SAR image can be generated in 10 s on a \$2M, 64 node, general-purpose massively parallel processor (MPC). This is a factor of 200 less cost-efficient than a \$100K, 1 s, special-purpose processor. While some of this factor is due to comparing parts cost with system price, most is due to the mismatch between conventional MMPs and the SAR problem. A conventional processor chip can perform only a single operation per cycle and has a cycle time slowed by the need to support high-precision (64-bit) arithmetic. In contrast, a special-purpose processor can perform tens to hundreds of arithmetic operations per cycle and can be tailored to the 24-bit precision required by the SAR problem.

Operating multiple slow machines, such as commercial workstations, in parallel to achieve high throughput but with high latency increases cost significantly as more total memory is required by this approach. Also, most

conventional workstation networks will not support the 800 Mbits/s bandwidth required to support a throughput of one image each 10 s.

3.4.1 Required Memory, Bandwidth, and Processing

Consider a model problem with the following parameters:

N	=	$16K$	Number of cells in one dimension (assume the same number in range and azimuth)
b_i	=	8 bits	Bits per input sample
b_o	=	8 bits	Bits per output sample
b_t	=	16 bits	Bits per twiddle factor
b_a	=	24 bits	Bits accumulated
T	=	10s	Interval between images

The system is characterized by

P Number of processors
R Block size - radix of FFP done entirely within the processor without a memory reference

The memory required to hold the problem input is $M_i = N^2 b_i$ (2 Gbits). During the computation $M_a = 2N^2 b_a$ (12 Gbits) are used to hold the intermediate values. $M_o = N^2 b_o$ (2 Gbits) are required to hold the output image. Only 2K twiddle factors are required although they may have to be replicated. The entire memory requirements will be slightly greater than $M = N^2(b_i + b_a + b_o)$ (16 Gbits).

The transpose requires moving 1–1/P of the data to other processors. For $P > 1$, half of the accumulated data must cross the bisection of the machine giving a required bisection bandwidth of $B_t = N^2(b_i + b_o)/2T (\sim 200$ Mbits/s)

of required bandwidth. Summing these gives the total required bisection bandwidth $B_b = N^2(2b_a + b_i + b_o)/2T(\sim 800$ Mbits/s).

If the processor has sufficient register storage (3R b_a-bit registers) it can perform a radix-R FFT without intermediate memory access. This requires loading R input values (and some number of twiddle factors which will be ignored) and storing R results. The entire data set must be both loaded and stored each lg(R) stages out of the 2lg(N) stages giving a required local memory bandwidth of $B_m = 8N^2 b_a cl(N, R,)/T$, where $cl(N, R)$ =ceil(lg(N)/lg(R)). (A reasonable value for R is 128 which would give a required bandwidth of 9.6 Gbits/s.)

The ratio of memory capacity to bandwidth is $(b_i+b_a+b_o)T/(8b_a cl(N, R))(\sim$ 1 s). For a comparison a standard 16 Mbit (4M $\times$ 4) DRAM chip has a page-mode bandwidth of 80 Mbits/s (4b $\times$ 20 MHz) and a capacity to bandwidth ratio of 0.2 s.

If the problem is partitioned over more than N processors, data must be exchanged between the processors after each lg(N^2/P) stages. These exchanges involve mostly local interprocessor communication with a small fraction of traffic crossing the bisection. This gives a required local communication bandwidth of $B_1 = 4N^2 b_a cl(N, N^2/P)/T$. (For N^2/P of 128, the required bandwidth is 4.8 Gbits/s.)

The radix-R FFT can be performed as lg(R)/2 radix-4 stages. Each stage requires 4 complex multiplies by twiddle factors ($b_t x b_a$) and 12 complex adds to accumulate the results. In terms of integer operations, this is 16 multiplies

and 32 adds. The total arithmetic bandwidth required is $B_x = 4N^2lg(N)/T$ multiples/s. (1.4G multiplies/s) and $B_+ = 8N^2lg(N)/T$ adds (2.8 G adds/s.)

To summarize the requirements of the full 2-D FFT calculation:

M	=	$N^2(b_i + b_a + b_o)$	16 Gbits
B_b	=	$N^2(2b_a + b_i + b_o)/2T$	$\sim$ 800Mbits/s
B_m	=	$8N^2b_acl(N,R)/T$	9.6Gbits/s
B_l	=	$4N^2b_acl(N,N^2/P)/T$	4.8Gbits/s for$N^2/P = 128$, if$N \geq$ P)
B_x	=	$4N^2lg(N)/T$	1.4G multiplys/s
B_+	=	$8N^2lg(N)/T$	2.8G adds/s

3.4.2 Silicon Area Required

Silcon-chip fabrication processors are described in terms of their "minimum linewidth". The conventional unit of length λ is set at 0.5 times the minimum linewidth. For example, s 0.5 μm fabrication process would have $\lambda = 0.25\mu$m.

The silicon area required to support the SAR processors described in the previous sections can be described in terms of the following information:

A_d	=	$100\lambda^2$	Area of a DRAM bit
A_s	=	$1K\lambda^2$	Area of SRAM bit
A_r	=	$3K\lambda^2$	Area of a register bit
A_+	=	$10K\lambda^2$	Area of an adder bit
A_c	=	$1.6G\lambda^2$	Area of a chip (1993)
A_{cf}	=	$6.4G\lambda^2$	Area of a chip (1997)
A_{cff}	=	$25G\lambda^2$	Area of a chip (2001)
f	=	100MHz	Operating frequency (1993)
f_f	=	200MHz	Operating frequency (1997)
f_{ff}	=	400MHz	Operating frequency (2001)
f_p	=	$2f$	Bandwidth per pin

f_{pm}	=	20MHz	Bandwidth per pin of commodity DRAM
f_{pmf}	=	100MHz	Bandwidth per pin of fast DRAM (sync)
p	=	200	Signal pins per chip
p_m	=	4	Data pins of commodity DRAM
p_{mf}	=	16	Data pins of fast DRAM (sync)

The area required for the memory to hold the problem is $A_m = MA_d(1.6T\lambda^2)$. This sets a minimum cost on a SAR system to handle a problem of this size with any throughput (assuming that the data is not swapped from a lower-cost mass storage device). In today's technology this memory can be packaged in $C_m = MA_d/A_c$ chips (1024 chips). The memory can be packaged in $C_{mf} = MA_d/A_{cf}$ chips (256 chips) in 1997 and $C_{mff} = MA_d/A_{cff}$ (64 chips) in 2001.

The arithmetic is of relatively low precision (24 bits) and can be performed on a redundant carry-save number representation which eliminates the need to propagate carries. A 24-bit integer carry-save adder has an area of 24 A_+(240Kλ^2) and a Booth-recoded 24 $\times$ 16 carry-save multiplier has an area of 192A_+ (1.9Mλ^2). Even unpipelined, the maximum logic depth through the multiplier Wallace trees is 10 gates, about 5 ns in a 1993 technology. To be conservative, we assume that each arithmetic unit is used once per cycle with an operating frequency of f. The required number of adders is $n_+ = B_+/f$ (28 adders) and the required number of multipliers is $n_x = B_x/f$ (14 multipliers). An aggressive design could cycle the arithmetic units (particularly the adders) multiple times in a single clock cycle to reduce the number of required units.

The area required to implement this arithmetic logic is $A_a = 24n_+A_+ + 192n_xA_+$ (34 Mλ^2). Some additional area would be required for address

generation logic. All of the arithmetic logic will fit comfortably on a small fraction of one chip in 1993 technology. A single chip, however, will not support the bandwidth required.

Providing 6R b_a-bit registers per processor requires area $A_R = 6RPb_aA_r(\sim 56M\lambda^2$ per processor for R = 128).

The off-chip memory bandwidth required by the processing chips (unless all memory is on the processing chips) is B_m. With a bandwidth of f_{pm} per memory pin, the number of memory data pins required is B_m/f_{pm} (480 pins). If the memory is implemented with conventional DRAM, it will take a minimum of $C_{pmb} = \text{ceil}(B_m/f_{pm}p)$ (3) processor chips and at least $C_{mb} = \text{ceil}(B_m/f_{pm}p_m)$ (120) memory chips to provide adequate bandwidth. For 1993 technology, the processor chips are bandwidth limited while the memory chips are capacity limited. By 2001 the memory system will be bandwidth constrained if a conventional interface is used; however, a high-bandwidth DRAM interface (e.g., RAMBUS or Sync-DRAM) would lower the bandwidth limit to $C_{mfb} = B_m/f_{pmf}p_{mf}$ (24) chips, fewer if the bandwidth of the fast DRAMs, f_{pmf}, scales with technology.

The interprocessor communication requirement for a machine with $P \leq N$ is determined by the bisection bandwidth required for the corner turn. If an $n-$dimensional cartesian mesh (n is typically 2 or 3) is assumed as the network, the pins per processor required are $2nB_b/(f_pP^{(n-1)/n})(16/P^{1/2}$ for n =2) and the total pins required are $2nB_bP^{1/n}/f_p(16P^{1/2}$ for $n = 2)$. For very large numbers of processors, $P > N$, the pins required for local bandwidth are $2B_l/f_p$ (48 pins). Both of these bandwidth pin requirements are modest.

The major demand on pinout is memory bandwidth because of the relatively low per-pin bandwidth of conventional memory chips.

3.4.3 Alternative Designs

This section explores some possible designs for a SAR processor tailored for performance.

Commodity DRAM-based SAR Processor. The most economical approach to construct a SAR processor is to use the cheapest available memory chips, commodity DRAMs, and the minimum number of processor chips to meet the throughput requirement. For the model problem above (16K × 16K FFT in 10 s) using 1993 technology, the system would have the following characteristics:

1. 4 processing elements.
2. Each processing element contains 1 processor chip and 256 16 M × 1 DRAM chips.
3. The DRAM chips are multiplexed 2:1 onto 128 data lines into the processor chip (this gives 512 DRAM data lines which is greater than the required 480). This interface also requires 12 multiplexed address lines, 2-column strobes, a row strobe, and a write enable (16 signals). The total signal count for the memory interface is 144. It may be necessary to provide separate addressing for subsets of the memory.

If this is the case, each separately addressed subset adds 16 memory interface signals.

4. Each processor chip has an 8-bit 200 MHz channel (1.6 Gbits/s) to each other processor chip (3 channels out, 3 channels in) for a total of 48 inter-node signals. This gives 4 times the required bisection bandwidth.

5. Each processor chip contains 16 24-bit carry-save adders and 8 16 $\times$ 24-bit carry-save multipliers (20 Mλ^2) along with an address generation unit. This gives more than twice the required arithmetic bandwidth.

6. Each processor chips contains 1024 24-bit registers (72 Mλ^2).

7. Each processor chip contains a 64 Kbit instruction cache (reloadable from the DRAM) (64Mλ^2). Simple instruction sequencing logic reads long instruction words from this cache to control operation of the chip.

8. Each processor contains a 4-bit 200 MHz input channel and a 4-bit 200 MHz output channel. Provision could be added to refresh a video display out of the output region of memory.

9. Each processor contains a switch connecting the arithmetic units and register files. At a minimum, the switch should provide 4 global 24-bit buses that span the width of the arithmetic units and register files. The switch can be specialized for the FFT computation (50 Mλ^2).

The processor chip has a total of 200 signal pins, adding power, ground, and clock pins will bring the total to about 300. It has a total area of 206 Mλ^2 making it easily realizable as a custom chip or standard cell design,

but difficult as a gate array. A system with 8 or 16 processors with fewer arithmetic units each would be quite feasible for gate array implementation.

The estimated parts cost of this minimal SAR processor is \$52,800 packaging, power supplies, assembly, and test should add 25% to this number. The major cost is \$51,200 for 1024 16 M $\times$ 1 DRAMs at \$50 each. The remainder is \$800 for 4 processors at \$200 each and \$800 for circuit boards and miscellaneous components. The processor chips are smaller than the DRAM chips (206 Mλ^2 vs. 1.6 Gλ^2) but cost more because they are lower volume parts with higher pinouts.

The throughput of the system can be increased and the latency reduced by adding more processors at a modest cost until the memory becomes bandwidth constrained. In this realm, the system cost is $S_1 = 52,000 + 8,000/T$. The memory becomes bandwidth constrained with conventional DRAMs when $C_{mb} = C_m$ or ceil$(8N^2 b_a cl(N,R)/T f_{pm} p_m)) = MA_d/A_c$. For conventional DRAMs, this occurs when $T = 1.2$ s. This gives a system with a cost of \$58,700, still memory dominated. For high bandwidth DRAMs (e.g., sync DRAMs), T can be reduced to 0.06 s before the memory is bandwidth limited. For high bandwidth DRAMs, the cost equation is $S_{1h} = 52{,}000 + 6{,}000/\mathrm{T}$. At the point, $T = 0.06$ s, where the system becomes bandwidth limited the cost is \$152,000 and is dominated by processor cost.

As technology scales, the system will become less expensive and will become bandwidth limited at a larger T. In 1997 technology, the minimal system will need only 256 64M DRAM chips at perhaps \$100 each and 4 processor chips which are half as expensive and twice as fast for a cost

equation of $S_{1f} = 25,600 + 2,000/T$. This system will become bandwidth limited at $T = 4.8$ s with conventional DRAMs and at $T = 0.24$ s with high-bandwidth DRAMs. In 2001, the system will require 64 256M DRAM chips at $200 each and improved processor chips giving a cost equation of $S_{1ff} = 12,800 + 500/T$. It will be bandwidth limited at $T = 20$ s with conventional DRAMs and at $T = 1$ s with high-bandwidth DRAMs.

High-Bandwidth DRAM System: The characteristics of a high-bandwidth DRAM-based system using 1993 technology near the point where the DRAM becomes bandwidth contained (T = 0.06 s) are:

1. 512 processing nodes.

2. Each processing node contains one processor (similar to that described above) and 2 1 M × 16 synchronous DRAMs. The RAM interface requires only 32 data lines, 10 multiplexed address lines, and 3 control signals (45 signal pins).

3. Each processor has 6 bidirectional 8-bit ports operating at 200 MHz to support a 3-D torus interconnection (6 × 2 × 8 = 96 signal pins). In a 512-node 8 × 8 × 8 × system, the network bisection is 64 channels × 2 directions × 8 bits × 200 MHz = 200 Gbits/s which comfortably exceeds the requirements for 128 Gbits/s at $T = 0.06$ s.

Beyond the point at which the DRAM becomes bandwidth constrained, reducing system latency requires replicating both processor chips and memory chips. In this region, the cost equation becomes $S_2 = \$9,144/T$.

As the latency is reduced, the channel widths must double each time the number of processors is increased by a factor of 8 to maintain adequate global bandwidth. A channel width of 16 is required at 1K nodes, 32 at 8K nodes, and 64 at 64K nodes. Channel widths greater than 16 bits exceed our chip pinout limitations. In this case, the machines will become global bandwidth limited and their performance will increase as the 2/3 power of the number of nodes. This limit is hit at $T = 8$ ms, $P = 4$K nodes. Beyond this point, the cost equation is $S_3 = 820/T^{3/2}$.

Single Processor/Memory Chip: At $P = 16$K nodes, the memory requirement per node is 1 Mb which can be implemented with SRAM on the processor chip in 1993 technology. At this point a single-chip node can be built eliminating the memory bandwidth bottleneck. In 1997, 4 Mb SRAMs on the processor will be feasible and single-chip nodes can start at $P =$ 4K nodes. In 2001, 16 Mb on-processor SRAMs can be used in 1K node machines.

As on-chip arithmetic capability can be easily extended, the performance of machines built from single-chip processing nodes will be entirely limited by inter-node bandwidth. The equation for S_3 above applies in this realm as well as with the coefficient reduced by 1/2 as the memory chips are no longer required.

Minimum Latency Design: For very large numbers of processors, the ultimate latency limit is set by the time required to distribute data. Assuming a 2-input arithmetic operation can be performed in one cycle, the

time required to perform the arithmetic operations for a 16K $\times$ 16K FFT composed of 14-stages of radix-4 FFTs is 56 clocks or 0.56 μs at 100 MHz.

The latency of each communication operation is proportional to the distance across the machine, $P^{1/3}$ or 2^{10}, the time to transfer the required data is proportional to $N^2/P^{2/3}$. If $N^2 = P$, this is also proportional to $P^{1/3}$. The constant factor here is about 4, so about 2^{12} cycles ($\sim$ 40μs) are required to perform the communication. Thus, the minimum latency for the entire operation is about 41 μs. In practice, the number of processors would be reduced to 2^{21} to balance the communication and computation times. This would give a latency of about 100 μs.

3.4.4 Latency, Throughput, and Cost

The graph, Figure 3-1, shows the relationship between latency, T, and cost for SAR processors implemented in 1993 technology. It is assumed that in all cases, the throughput is $1/T$. As long as the memory is capacity limited (rather than bandwidth limited), it is inefficient to solve multiple problems in parallel to give a throughput higher than $1/T$. This increases the memory requirements which dominate cost. It is more efficient to keep memory constant and increase the processing.

The chart has three regions of interest. From a latency of 10 s down to 0.1 s, the cost of the system is dominated by the memory required to hold the problem and is largely insensitive to latency. Over these two orders of magnitude in performance, cost is only increased by a factor of two. From

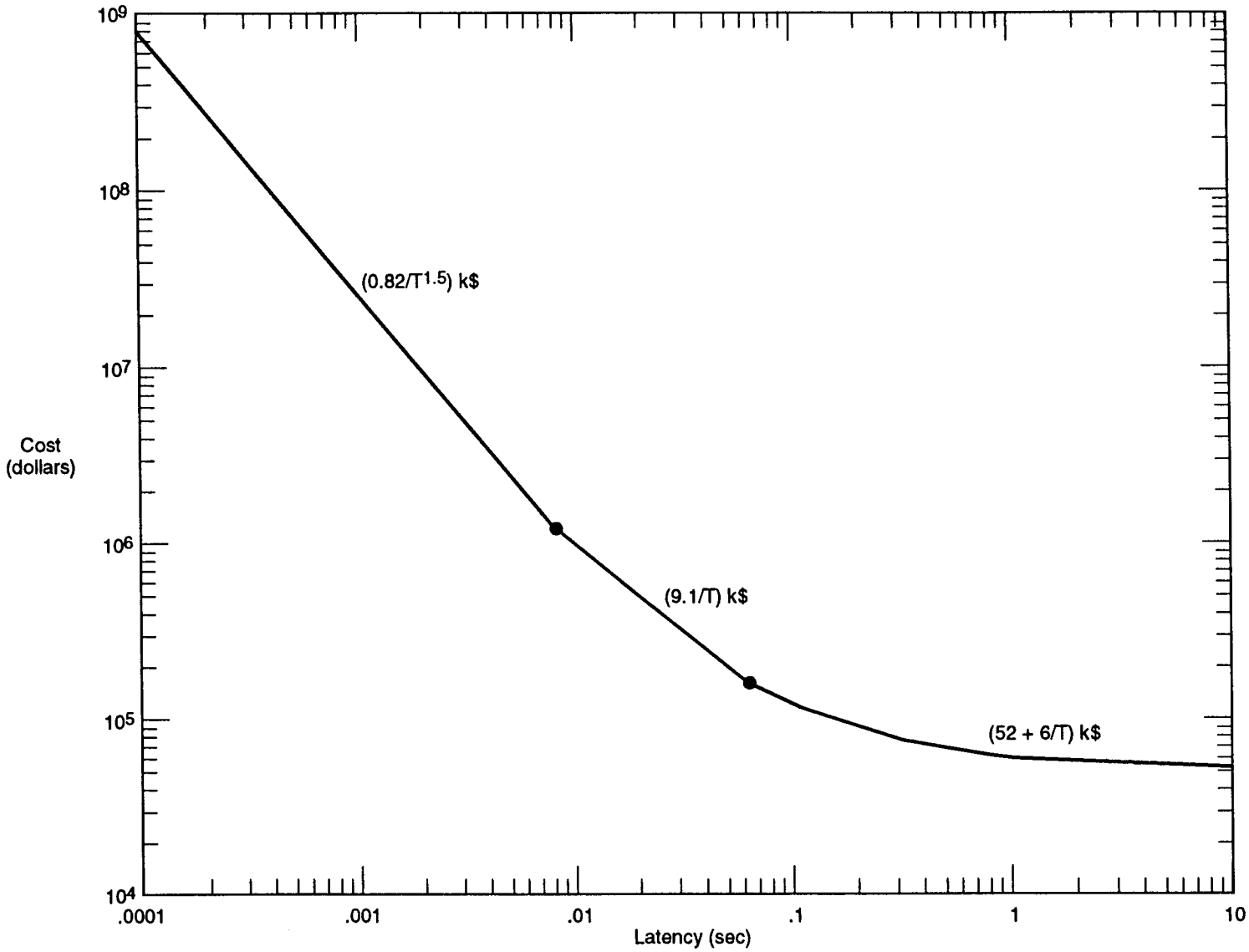

Figure 3-1. Cost as a function of latency for SAR processors implemented in 1993 technology.

Table 3.5. Commercial DSP-Based Design

Manufacturer	Part	Bits	T(1K) μs
Sharp	LH9124	24	90
Plessy	PDSP16510	16	48
Austek	A41102	24	400
TRW	TMC2310	16	514
LSI Logic	L64280	24	144
Array	A66110	16	131
AT&T	DSP32	32	3500

0.1 s down to 0.008 s, the machine is processor limited and cost increases proportional to throughput, $1/T$. Below 0.008, the machine is communication limited and cost increases as $1/T^{1.5}$. Communication limits latency to be no less than about 50 μs. However, higher throughput machines can be built.

3.4.5 Commercial DSP-Based Design

Table 3.5 shows the capabilities of contemporary commercial FFT chips. Three of the chips offer 24-bit precision while the remainder provide only 16-bits. For the fastest 24-bit part, the Sharp LH9124, a 1K complex FFT can be performed in 90 μs. With a single Sharp part, a 16K FFT should take less than 3 ms, and the full 16K $\times$ 16K should take about 100 s. Thus a machine built from 16 of these parts would be capable of solving the model problem in 10 s.

A general-purpose DSP chip, the ATT DSP32, is included for comparison.

General-purpose DSP chips are microprocessors with some special features for signal processing. They are easily programmable for a wide variety of functions. However, their performance is more than an order of magnitude slower than the specialized FFT chips.

A machine built from commercial FFT chips would require a number of semi-custom chips or programmable logic devices (PLDs) to perform address generation, memory interface, inter-processor communication, and control functions. It is possible that a general-purpose DSP chip could perform some of these functions. Compared to the full-custom solution, using commercial FFT chips requires 16 vs. 4 processing chips and the need for some number (probably 3 or 4) additional support chips per processor chip. For $T = 10$ s, however, cost is still dominated by memory and thus the cost of the commercial FFT solution is comparable to the cost of the full custom approach. Because of the large number of support chips required, the development cost for the commercial FFT solution is no less than that required by the full custom solution.

3.4.6 Commercial Multiprocessor and Multicomputers

The SAR calculation can be performed on commercial multicomputers. However, the efficiency (performance/cost) is less than that of a machine using specialized FFT chips.

Consider the Cray T3D MPC based on the DEC Alpha chip. To compute the model 16K $\times$ 16K problem in 10 s requires 4.2 Gops/s of arithmetic per-

formance. Each Alpha has a peak performance of 150 MFlops; derating this to 75 MFlops for FFTs, about 64 Alpha processors are required to perform this computation. (Compare with 4 custom chips.)

While most MPCs are optimized for 64-bit floating point, most also support 32-bit FP which is adequate for the SAR calculation. To store the 256M point complex image in 32-bit FP requires 16 GBits or 2 GBytes of memory, or 32 MBytes of memory per node. A machine with 64 MBytes per node is required to hold input data and code as well as the in-process transform.

The bisection bandwidth of a $2 \times 2 \times 2$ partition of a T3D is 2.4 GBytes/s, well above the required 800 Mbits/s.

The major problem with using a general-purpose MPC for the SAR calculation is cost. At upwards of \$30K/node, a 64-node MIMD system would cost \$2M vs. \$53K for a full custom system with the same performance (T=10 s). At $T = 1$s, a \$20M 640-node MPC compares unfavorably with \$60K parts cost for a custom system. While this is comparing system price to parts cost, the message is still clear. The result is not very different for SIMD machines, which may have a further problem of insufficient memory. General-purpose MPCs cost an order of magnitude more than special-purpose processors for the SAR calculation because, as with the general-purpose DSP chips, their processors are 10-100 times less efficient than specialized FFT processors. Also, at the lower latencies, the ratio of processor to memory in an MPC is unbalanced for the SAR problem. Large MPC systems have more memory than is required to hold the problem and hence cost more than a system with a memory size matched to the problem.

3.5 Brute-Force SAR Processing

Consider the problem of directly computing an image from raw SAR data after range compression without use of an FFT by convolving the raw data with the point-spread function for each point of the image. Computing the image in this manner eliminates all phase error. The brute-force computation requires over 1,000 times $(N/lg(N))$ as much computation as the conventional transform method for a 16K $\times$ 16K image. However, the brute-force computation is feasible with contemporary VLSI technology. Moreover, it requires less memory bandwidth and less total memory than the FFT-based approach.

3.5.1 Brute-Force Convolution

Let the range-compressed SAR data be $a(t,s)$ and the output image be $b(x,y)$. A single point reflector at location (x,y) produces an impulse with a delay of

$$d(s,x,y) = \left((s-x)^2 + y^2\right)^{\frac{1}{2}} \sim y + \frac{(s-x)^2}{2y} \tag{3-103}$$

in the return corresponding to position s in the compressed SAR data, a, giving a point spread function of

$$P_{xy}(s,t) = \delta(t-d)e^{i\omega 2d/c}. \tag{3-104}$$

A brute-force method for computing the image is to explicitly convolve P_{xy} with the compressed SAR data, a, to generate each point (x, y) of the image.

$$b(x, y) = \sum_s a(s, d) e^{-i\omega 2d/c}. \tag{3-105}$$

This is a sum in only the s-direction as there is only a single non-zero value of P_{xy} for each s.

For an $N \times N$ image, N complex multiply-adds are required to compute each point b(x,y). Same number, $n << N$, of additional operations will be required at each point to compute the distance function, d, using a DDA, (digital differential analyzer) and to linearly interpolate $a(s)$ between the two values of t nearest d. Thus, the total number or arithmetic operations to directly compute image b is less than $8N^3$, 32 Tera-ops for a 16K $\times$ 16K image. This is in addition to the $N^2 lg(N)$ (4 Gops) operations required for range compression. For comparison, the FFT-based approach to SAR requires about 8 Gops for a 16K $\times$ 16K image.

Brute-Force 16K $\times$ 16K Image Takes 1,000 Chip-Seconds with 1993 Technology

A 24-bit integer multiplier takes about 2 Mλ^2 of area and an adder takes 0.25Ml^2. Assuming equal numbers of multipliers and adders, a 1993 0.8μm chip with area of 1.6 Gl^2 can hold over 370 arithmetic operators and still devote three-quarters of its area to memory and interconnect. Operating at 100 MHz this gives a total performance of 37 Gops per chip. Thus, it would take about 950 chip-seconds to compute the brute-force SAR, say 100 chips for 10 s.

Table 3.6 Chip Second Requirements

	Area	Freq	Units/Chip	Ops/Chip-s	Chip-s
1993	1.60E + 09	1.00E+08	370	3.7037E+10	949.98
1997	6.40E + 09	2.00E + 08	1481	2.963E + 11	118.75
2001	2.50E + 10	4.00E + 08	5787	2.3148E+12	15.20

Table 3.6 shows how the number of chip-seconds required decreases over time. This table is actually a little pessimistic since it only accounts for decrease in line size and not increase in chip dimensions.

Sufficient Bandwidth

The brute-force calculation, if done in along-track (x-first) order has very good locality of reference. All of the points at the same range (y) compute their values from the same range (t) band in the *raw* data. Thus, if the chips have sufficient internal storage to hold one range band, a new row of input data will only need to be input once per row of points—viz., the raw data will only need to be loaded once. The memory bandwidth demand in this case is $N^2(b_a + b_o)/T$ (1.6 Gbits/s for a 16K $\times$ 16K in 10 s). This is less than the amount required for the FFT-based approach because each data point is loaded exactly once and no intermediate results are written to storage. The bandwidth requirements of the pulse-compression FFT still remain and are in addition to this amount.

The computation should be partitioned across the processors in the along-track direction. That is each processor holds a contiguous range of x and s. The only interprocessor communication required is to sum the contributions,

one per processor, for each point. The total bandwidth here is $N^2 P b_a/T$ (60 Gbits/s) or $N^2 b_a/T$ (600 Mbits/s) per processor. For the model problem, this is less than one 8-bit bus at 100 MHz.

The number of points in the t direction that must be retained in on-chip memory is $N^2\Theta/8$ where Θ is the beam angle. Relative to the range, the width of the synthetic aperture is $\sin\Theta \sim \Theta$ while the maximum width of range required to cover all data from a single point is $1 - \cos(\Theta/2) \sim \Theta^2/8$. $N\Theta/8$ points of each column must be retained for a total of $N^2\Theta/8$. Thus, ~50 Mbits of fast storage is required distributed over 100 processor chips. This amounts to 500 Kbits/chip which is feasible using SRAM in a 0.8 μm process. At $1K\lambda^2$ per bit, this takes 500 $M\lambda^2$ of area, about 1/3 of a modern 0.8 μm chip.

The chips internally require modest communication resources. Each chip is partitioned into a number of units each with its own RAM that hold and processes a portion of the along-track (s) dimension. The only communication required is a tree-structured sum to add up the contributions from each partition on chip.

3.6 What Number of Parallel Processors Are "Right" for SAR?

SAR reconstruction algorithms have been implemented on traditional supercomputers, such as Crays, and are beginning to be implemented successfully on massively parallel machines with $N_p = 10^2$ to 10^3 processors. One

might wonder whether "more" processors is inevitably "better" in any quantifiable sense, or (for that matter) whether $N_p = 1$ (or few) is better?

As an example of how to answer such a question, on very general grounds, let us define "better" to be "cheaper" in the sense of production throughput per invested capital dollars. (Other definitions are, of course, possible: a real-time system might need latency, or processing time, minimized regardless of the cost.)

Define the following quantities:

$$N_p = \text{Number of processors}$$

$$\alpha = \text{Fraction of processing that is parallelizable}$$

so that $0 \leq \alpha \leq 1$.

$$C_1 = \text{Cost per processor}$$
$$C_2 = \text{Cost of sufficient memory to process an image.}$$

In terms of these quantities, the time required to process an image scales as

$$T \propto (1 - \alpha) + \alpha / N_p.$$

According to the time value of money, the throughput cost scales as the product of the capital cost and the time to process an image,

$$\text{Cost} \propto [(1 - \alpha) + \alpha / N_p][C_1 N_p + C_2].$$

Minimizing this throughput cost with respect to N_p gives the result

$$N_{p,min} = \sqrt{\frac{\alpha}{1 - \alpha} \frac{C_2}{C_1}}.$$

It is instructive to put in plausible values for the quantities that enter on the right. The fractional parallelization α is likely in the range 0.95 to 0.99, with the upper value corresponding to a rough estimate of the contribution of (non-parallel) I/O alone. C_2 is the cost of on the order (say) few $\times$ 16,000 $\times$ 16,000 $\times$ 4 bytes = few $\times$ 10^9 bytes of memory.

At \$100/Mbyte, this is few $\times$\$$10^5$. For massively parallel machines, the cost C_3 of a single processor is likely in the range \$$10^2$ to \$$10^4$.

We then get a range for $N_{p,min}$ of roughly

$$25 < N_{p,min} < 500.$$

The number of processors $N_{p,min}$ is expected to increase over time due to two effects. First the parallelizable fraction $\propto$ will increase and second, the ratio of processor cost (dollars per MIPs) to memory cost (dollars per megabyte) will continue to decrease at about 20% per year.

3.7 What Computer Architectures Will Do SAR Processing?

SAR reconstruction algorithms have been implemented on special purpose hardware and recently on massively parallel machines. One might wonder if, as time passes, SAR processing will use more and more parallelism, or less and less.

One might look for the architecture that maximizes operations per dollar per second. One might instead look at the number of operations required for

conventional SAR processing, and ask what architecture is needed to provide that much calculation in a reasonable amount of time.

Computational Load of Conventional SAR Processing

In a SAR data stream, assume that the input is RA samples, R in range and A in azimuth. Conventional processing is essentially A Fourier transforms in range, a matrix transpose, and then R Fourier transforms in azimuth. Let k be the multiplier that translates complex Fourier operations into machine operations. Then the operation count is

$$kAR \log R + \text{cost of transpose} + kAR \log A = kAR \log AR + \text{cost of transpose.}$$

The transpose is essentially free on a shared memory machine, but adds about 50% on a machine with lots of processors that don't share memory.

We take $k = 10$, for definiteness. This should be within a factor of 2 of a more precise estimate, and it fits the results of simple experiments on an SGI workstation. A SAR mapping image that is one kilometer square with a sample every meter has $A = R = 1,000$, and this is $2 \cdot 10^8$ operations. If we assume that the processing requires 8 bytes per sample, this image requires about 8 megabytes. A much larger image, 10 kilometers in azimuth and 100 kilometers wide, would take about $3 \cdot 10^{11}$ operations. If each complex sample is 8 bits, as above, this image takes about 2,000 megabytes, which is within the range of current high-performance scientific workstations.

Machines of this class currently do about 20 million operations per second. At this rate, the smaller of our two images would take 10 seconds on one

processor, and the larger would take 15,000 seconds on one processor and about 2,000 seconds on an 8 processor shared memory machines.

Speculating about how rapidly performance will improve normally gives at least a factor of 2 every two years. This conservative rate gets us to 160 million operations per second by 1999. The first image now takes a couple of seconds. The second image requires about 2,000 cpu seconds, which would be 250 seconds on an 8 processor machine. The cost today of a machine with eight 20 mip processors and two gigabytes of memory would be about $500,000, at least half of which would be for memory. Memory will cost less per byte in 1999.

A more radical view is that performance will improve by a factor of two every year. Then the second image would take 250 cpu seconds in 1999, which is 30 seconds on an 8 processor machine. This is real time for a radar moving 1,200 km/hr.

This argument can be run backwards. In 1999 we expect that 8 or 16 processor machines with gigabytes of memory will be $500,000, or less in current dollars. These machines will do between 1,200 and 10,000 million operations per second.

Table 3.7 can be used to estimate the suitability of shared memory multiprocessors for SAR processing. The column headed *AR* contains the number of samples per image. This is directly translated into memory, at 2 bytes per sample for input, and 8 bytes per sample for processing. The columns under "CPU Seconds" give the number of CPU seconds required to do the processing at various MIP rates. The final column, labeled "Big," gives the

Table 3.7. By the end of the century, conventional computers will be able to produce quite large SAR images in a few minutes. More powerful computers will be needed only for what are currently special purposes.

AR	Ops	CPU-Seconds at						Big
		20 mips	50 mips	100 mips	200 mips	500 mips	1000 mips	
$1\ 10^{6}$	$1.99\ 10^{8}$	$1.0\ 10^{1}$	$4.0\ 10^{0}$	$2.0\ 10^{0}$	$1.0\ 10^{0}$	$4.0\ 10^{-1}$	$2.0\ 10^{-1}$	$1.2\ 10^{-2}$
$2\ 10^{6}$	$4.19\ 10^{8}$	$2.1\ 10^{1}$	$8.4\ 10^{0}$	$4.2\ 10^{0}$	$2.1\ 10^{0}$	$8.4\ 10^{-1}$	$4.2\ 10^{-1}$	$2.6\ 10^{-2}$
$5\ 10^{6}$	$1.11\ 10^{9}$	$5.6\ 10^{1}$	$2.2\ 10^{1}$	$1.1\ 10^{1}$	$5.6\ 10^{0}$	$2.2\ 10^{0}$	$1.1\ 10^{0}$	$7.0\ 10^{-2}$
$1\ 10^{7}$	$2.33\ 10^{9}$	$1.2\ 10^{2}$	$4.7\ 10^{1}$	$2.3\ 10^{1}$	$1.2\ 10^{1}$	$4.7\ 10^{0}$	$2.3\ 10^{0}$	$1.5\ 10^{-1}$
$2\ 10^{7}$	$4.85\ 10^{9}$	$2.4\ 10^{2}$	$9.7\ 10^{1}$	$4.9\ 10^{1}$	$2.4\ 10^{1}$	$9.7\ 10^{0}$	$4.9\ 10^{0}$	$3.0\ 10^{-1}$
$5\ 10^{7}$	$1.28\ 10^{10}$	$6.4\ 10^{2}$	$2.6\ 10^{2}$	$1.3\ 10^{2}$	$6.4\ 10^{1}$	$2.6\ 10^{1}$	$1.3\ 10^{1}$	$8.0\ 10^{-1}$
$1\ 10^{8}$	$2.66\ 10^{10}$	$1.3\ 10^{3}$	$5.3\ 10^{2}$	$2.7\ 10^{2}$	$1.3\ 10^{2}$	$5.3\ 10^{1}$	$2.7\ 10^{1}$	$1.7\ 10^{0}$
$2\ 10^{8}$	$5.52\ 10^{10}$	$2.8\ 10^{3}$	$1.1\ 10^{3}$	$5.5\ 10^{2}$	$2.8\ 10^{2}$	$1.1\ 10^{2}$	$5.5\ 10^{1}$	$3.4\ 10^{0}$
$5\ 10^{8}$	$1.44\ 10^{11}$	$7.2\ 10^{3}$	$2.9\ 10^{3}$	$1.4\ 10^{3}$	$7.2\ 10^{2}$	$2.9\ 10^{2}$	$1.4\ 10^{2}$	$9.0\ 10^{0}$
$1\ 10^{9}$	$2.99\ 10^{11}$	$1.5\ 10^{4}$	$6.0\ 10^{3}$	$3.0\ 10^{3}$	$1.5\ 10^{3}$	$6.0\ 10^{2}$	$3.0\ 10^{2}$	$1.9\ 10^{1}$
$2\ 10^{9}$	$6.18\ 10^{11}$	$3.1\ 10^{4}$	$1.2\ 10^{4}$	$6.2\ 10^{3}$	$3.1\ 10^{3}$	$1.2\ 10^{3}$	$6.2\ 10^{2}$	$3.9\ 10^{1}$
$5\ 10^{9}$	$1.61\ 10^{12}$	$8.1\ 10^{4}$	$3.2\ 10^{4}$	$1.6\ 10^{4}$	$8.1\ 10^{3}$	$3.2\ 10^{3}$	$1.6\ 10^{3}$	$1.0\ 10^{2}$
$1\ 10^{10}$	$3.32\ 10^{12}$	$1.7\ 10^{5}$	$6.6\ 10^{4}$	$3.3\ 10^{4}$	$1.7\ 10^{4}$	$6.6\ 10^{3}$	$3.3\ 10^{3}$	$2.1\ 10^{2}$
$2\ 10^{10}$	$6.84\ 10^{12}$	$3.4\ 10^{5}$	$1.4\ 10^{5}$	$6.8\ 10^{4}$	$3.4\ 10^{4}$	$1.4\ 10^{4}$	$6.8\ 10^{3}$	$4.3\ 10^{2}$
$5\ 10^{10}$	$1.78\ 10^{13}$	$8.9\ 10^{5}$	$3.6\ 10^{5}$	$1.8\ 10^{5}$	$8.9\ 10^{4}$	$3.6\ 10^{4}$	$1.8\ 10^{4}$	$1.1\ 10^{3}$

number of seconds required to do the processing on a 16 processor machine with 1,000 mip processors sharing memory. For machines that don't share memory, the times should be multiplied by about 1.4, to account for the transpose time.

Consider a plane flying at 900 km/hr, which is a kilometer every 4 seconds. Suppose we want one kilometer wide images (in azimuth), computed in real time. (Actually delayed one frame time.) In 4 seconds our 1999 computer with 8 processors could do between 5 and 40 billion operations. There is enough computing power at the low end for 20,000,000 samples, and at the high end for about 160,000,000 samples. The slower machine would support one meter samples in a square 4 kilometers on a side. The faster machine would support the same size image, but at 3 samples per meter.

3.8 Massive Mapping Project

For wide area mapping, I/O bandwidth and storage are at least as important as raw processor speed. As an example of a future massive mapping capability, consider a project to map the earth land-surface with a SEASAT-like SAR. Relevant characteristics are:

SEASAT characteristics:

		SEASAT
Swath Width (km)	W	100
Azimuthal Resolution (m)	δx	23
Range Resolution (m)	δr	20

Other quantities:

		Nominal
Fraction of earth surface	f_{earth}	0.3
Radius of earth (km)	R_{earth}	6400
Orbital Period (minutes)	T_{orb}	90

Let N_{image} be the total number of images required to map the earth surface, R_{image} be the required rate of image formation for realtime mapping, and R_{data} be the required data rate (assuming complex image and 2 bytes per pixel). Then in terms of the quantities defined above:

$$N_{image} = 4\pi R_{earth}^2 \left(\frac{1}{W^2}\right) f_{earth} \sim 15000 \left(\frac{W}{100 \text{ km}}\right)^{-2} \left(\frac{f_{earth}}{0.3}\right)$$

$$R_{image} = 2\pi R_{earth} \left(\frac{1}{W}\right)\left(\frac{1}{T_{orb}}\right) \sim \left(\frac{1}{13.5s}\right)\left(\frac{W}{100\text{km}}\right)^{-1}\left(\frac{T_{orb}}{90\text{min}}\right)^{-1}$$

$$R_{data} = 2R_{image}\left[\frac{W^2}{(\delta x)(\delta r)}\right] \sim (3.7MB/s)\left(\frac{T_{orb}}{90\text{min}}\right)^{-1}\left(\frac{W}{100\text{km}}\right)\left(\frac{\delta x}{20\text{m}}\right)^{-1}\left(\frac{\delta r}{20\text{m}}\right)^{-1}.$$

For a SEASAT-like SAR, a full surface map is readily accomplished and requires only 15000 images, 14 seconds processing time per image, and an I/O rate of 3.7 MB/s.

Future SARs are expected to be multi-spectral, polarimetric, and have higher resolution. As an agressive goal, we evaluated the requirements of

a system that could store one million 16K $\times$ 16K images at one image per second. As described in earlier, MPC systems which process on average of 1 image per second are commercially available as high- end parallel systems. Alternatively, instead of fully reduced images, range-compressed data can be archived, reducing the computational requirements prior to archiving.

One image per second implies 2x256 MByte/s at 2 bytes per image. One million images will require 512 Terabytes of storage. Such capabilities are possible using commercially available equipment. Specifically, a system can be designed based on high-speed digital tape recorders. Current ID-1 tape technology allows sustained read/write speeds of 50 MB/s. Ten drives in parallel can be used to achieve 500 Mbyte/s write capability, comparable to that needed for recording one image per second. The largest current tape capacity is about 100 Gbyte for an ID-1 cartridge, requiring 5000 tapes to archive approximately 1 million images. Commercially available tape robot technology allows access to a large tape archive at about 5-10 s per cartridge.

The total cost of the hardware for such a system is in the range of 5-10M$ (12 drives at 250K$ per drive, 5000 tapes at $100 per tape cartridge, and 2M$ for an archival tape robot). System costs should drop as digital video recording technology becomes widely adopted.

4 NOVEL METHODS IN SAR EXPLOITATION

4.1 Moving Targets

Measurements of moving objects present a fundamental problem for SAR, because the number of unknowns exceeds the number of measurements available to a single SAR platform. Consider, for example, an airborne early warning radar where the unknown target velocities are comparable to the motion of the target aircraft itself. Synthetic aperture radar measures the range R to a target and also, through evolution of phase $\alpha = \frac{4\pi R}{\lambda}$, the time history of the range. Under the assumptions of constant radar and target velocities, the range can be written as

$$R = \left[(R_o + U_r t)^2 + U_{az}^2 t^2\right]^{1/2} \tag{4-1}$$

where R_o is the initial range and U_r, U_{az} the initial relative radial and azimuthal velocities

$$\begin{aligned} U_r &= \mathbf{r}_o \cdot (\mathbf{U_t} - \mathbf{V}) \\ U_{az} &= \mathbf{r_o} \times \mathbf{z} \cdot (\mathbf{U_t} - \mathbf{V}) \end{aligned} \tag{4-2}$$

where $\mathbf{r}_o = \mathbf{R_o}/R_o$ is the unit vector in the initial radar-target direction, $\mathbf{U_t}$ the target velocity, and $\mathbf{V} = V\mathbf{x}$ the aircraft velocity. Thus the range (Equation (4-1)) is a function of only three quantities which synthetic aperture

radars normally determine by range gating to find R_o and measuring phase rate of change

$$\frac{d\propto}{dt} \approx \frac{4\pi}{\lambda} U_r \qquad \frac{d^2\propto}{dt^2} \approx \frac{2\pi U_{at}^2}{\lambda R_o}. \tag{4-3}$$

In normal synthetic aperture radar, it is assumed that the target velocity is zero and there are only two unknowns to determine (X_o, Y_o) —the horizontal target position coordinates. Standard SAR processing algorithms determine these coordinates from the data stream.

But a moving target has 4 unknowns: X_o, Y_o and two horizontal components of $\mathbf{U}_t$. Range and phase measurements can not determine them all. In particular, one can not determine the target direction unit vector $\mathbf{r}_o$ and so an accurate determination of U_r

$$U_r = U_{tr} - V\cos\theta \qquad \cos\theta = \hat{\mathbf{r}}_o \cdot \hat{\mathbf{x}} \tag{4-4}$$

still leaves the well-known ambiguity between target radial velocity and bearing angle to target.

There are three possible approaches to obtaining the fourth observational datum.

1. Use real-aperture, monopulse techniques to determine target bearing. With this approach, the target image features will all be resolved with full SAR capabilities, the actual location will depend on monopulse resolution.

2. Invoke *à* priori knowledge concerning the direction of the target velocity e.g., motion along a known highway or railroad, or a motion direction

relative to target image features. Specifically, a vehicle or aircraft image will indicate a front and a back. It is highly likely that the aircraft is moving from back to front.

3. Simultaneous measurements from two separated SARs.

We shall discuss these approaches below.

Computational processing of SAR signals from scenes with moving targets is more complex than standard SAR processing because of the need to determine the unknown azimuthal velocity. The result must be displayed in a three-dimensional space. Fortunately, for many moving target applications, the desired spatial and doppler resolution is not as high as standard SAR maps. The following example is illustrative. Suppose a UHF AWACS radar with 20m range resolution and $\tau_o \cdot PRF \approx 3000$ where τ_o denotes the scan period. Then one could consider 10 independent frames in azimuth (each of width 36°) and 50 frames in range with 512 × 1024 data points per frame. A complete azimuthal scan is composed of 500 separate images, each with $N_d = 500k$ data points capable of being imaged by a separate processor. The number of operations N_{ops} needed to investigate N_{az} azimuthal velocity hypothesis per computer in one azimuthal scan is

$$N_{ops} \approx 4.10^7 N_{az}. \tag{4-5}$$

For the scanning AWACS radar a reasonable number is $N_{az} \sim 10$. It follows that a processor capable of 40 Megaflops-characteristic of current work stations- would be required to create the image within a 10 sec scan period. Thus processing for MTI is highly parallelizable but each processor must have

1 megabyte of storage. The specifics of SAR processing for radial velocity U_r in a radar with a staggered PRF remain to be given.

The number of azimuthal velocity elements is expected to be small for an azimuthal scan radar, but will be large for conventional SAR images. We find that the azimuthal velocity spacing δU_{az} is

$$\delta U_{az} \approx \frac{r_o \lambda}{U_{az} t_o^2} \tag{4-6}$$

where t_o is the coherent illumination time for a target. Equation (4-6) has a simple interpretation. Recall that $U_{az}\ t_o$ is the length of the synthetic aperture. Thus Equation (4-6) is simply the statement that the resolution element in azimuthal velocity correspnds to passage through an azimuthal resolution cell in a coherent illumination time. For azimuthal scan radars, $t_o < 1$ sec and $\delta U_{az} \sim U_{az}$.

But for conventional SAR imagery where $t_o \sim r_o \lambda (D U_{az})^{-1}$ where D is the physical antenna size, one finds

$$\frac{\delta U_{az}}{U_{az}} = \frac{D^2}{r_o \lambda} << 1 \tag{4-7}$$

and many azimuthal velocity hypotheses are needed. This is the cause of the common observation that SAR processing smears moving targets.

Our anticipated computational advances would enable one to compute an image for each azimuthal velocity, therefore identifying the presence of moving objects in a scene. Consider an aircraft x-band radar with desired resolution $\Delta x \approx D/2 = 0.5$ m. Then for $r_o \sim 20$ km, $U_{az} \sim 150$ m/sec

$$\delta U_{az} = .25\,\mathrm{m/sec} \tag{4-8}$$

and roughly $N_{az} \approx 200$ azimuthal velocity resolution cells are required to accommodate vehicle traffic. A latency time of less than 0.1 sec, expected in future computational capabilities, will permit one to generate 200 images, each for a particular choice of azimuthal velocity within 20 secs. Thus modern computation will enable one to identify all objects moving at vehicular speeds. But, the location of these vehicles in the image will still suffer positional uncertainty associated with radial velocity. In brief, it is possible to image moving objects and to determine their range, but almost all azimuthal positional accuracy, apart from real aperture resolution, is lost. Put another way, the radial velocity spread δV_r across a scene[1] is

$$\delta V_r = \frac{y_1 - y_2}{r_o} V \sim 30 \text{ m/sec} \tag{4-9}$$

for $(y_1 - y_2) \sim 4$ km.

Thus for each azimuthal velocity, one must try several radial velocities to bring the imaged object onto the scene, because 30 m/sec is just a fraction of the possible radial velocity.

If the number of moving objects is limited, the computational load will be limited if they are first identified at a coarse spatial resolution and consequentially at a coarse velocity resolution, and with finer resolution applied to identified objects.

A second approach to mapping moving objects is to apply *à* priori knowledge. For example, if one believes that a moving object is on a highway, one simply selects the radial velocity needed to place the object on the highway

[1]The ratio $V/r \sim 7.5 \cdot 10^{-3}$ sec^{-1} is almost identical for satellites and aircraft.

in the azimuthal coordinate. A search through azimuthal velocities is still needed to identify the object. Once the azimuthal velocity is found, a consistency check that the velocity lies along the highway is possible. If this check does not work out, another highway should be selected. Let us point out that the radial velocity uncertainty associated with a azimuthal position $\Delta y \sim 5$ m uncertainty in placing an object on the highway is only $\simeq 4$ cm/sec. Combined with Equation (4-8), this leads to highly accurate velocity directions for each postulated azimuthal position.

All coordinates of moving objects can be determined by two simultaneous SAR images. In fact, one needs only one SAR transmitter. The second unit can be a receive-only vehicle, and difference SAR processing, such as worked out for the Battlefield SAR illuminator (see Section 6.3), implemented. Simple range-gating puts any object at the intersection of two circles. Usually, one intersection can be ruled out by real aperture considerations, giving a precise location of the target. Velocities can then be determined by the considerations of the previous paragraph.

4.1.1 Future SARS

A desirable future SAR capability is the detection and imaging of moving objects in SAR scenes. What requirements will this place on our computational and radar hardware? First, the system must be able to accommodate the doppler shifts associated with moving objects, for example $\pm$ 50 m/sec for vehicular traffic and $\pm$ 300 m/sec for subsonic aircraft. Equation (4-9)

indicates present systems are designed to roughly $\pm$ 30 m/sec. Given this doppler capability, then the computer hardware needs to be able to process $\sim$ 500 separate images for each SAR scene. Moving objects will appear at appropriate radial and azimuthal velocities, but the azimuthal coordinate of the object will be completely unknown. Nonetheless, for the correct azimuthal velocity and radial velocity accurate to $\approx$ 20 m/sec, the moving object will appear with full spatial resolution and at an accurate range, but with a totally arbitrary azimuthal location.

A second simultaneous SAR observation suffices to determine the azimuthal position, at the intersection of two constant-range curves. Thus future SAR installations might well consider configurations with an illumination transmitter and an additional separate receiver that needs only very modest receive antennas. Such configuration, coupled with anticipated computational advances to achieve short latency, in principle can determine moving targets positions and velocities to SAR-level precision.

4.1.2 SAR Processing

The possibility of using airborne SAR to detect moving targets on the ground was first discussed by Raney [21] in 1971 in which he studied the effects of target motion on SAR images. Two more recent papers, one by Freeman and Currie [22] in 1987 and one by Chen and McGillem [23] in 1992 have studied this problem. First we will examine airborne SAR examples of their work by the technique of Freeman and Currie. Following this we

will briefly discuss the results of Chen and McGillem. Figure 4-1 shows the geometry between an airborne SAR and moving point target. The range between target and platform as a function of time is given by

$$\begin{aligned} R(t) &= \{(Vt - x)^2 + y^2 + h^2\}^1/2 \\ V &= \text{radar velocity}. \end{aligned}$$

Defining time $t = t_o$ to be the time at which the target is broadside to the platform $R(t)$ can be expanded on a series about $t = t_o$. Neglecting higher order terms the range variation between target and platform is

$$R(t) = R_o + v_r(t - t_o) + a_r + |V'|^2)(t - t_o^2)/2.$$

With this expression for range delay between target and platform it is possible to determine the target signature

$$s(t) = \sigma_1 g(t)\exp(jy_1)\exp\{4R(t)/\lambda\},$$

where σ_1 and y_1 are target cross-section and phase terms (which can be ignored for present purposes).

$$g(t) = g\{(v - x_o')t\}$$

is the two-way azimuth antenna pattern, corrected for target velocity in the direction of the aircraft track. For uniform antenna illumination

$$g(t) = [\sin\{l(t)\}/\beta(t)]^2$$

and

$$\beta(t) = d(V - x_o')t/\lambda R_o.$$

Now

$$s(t) = \text{sinc}^2\{\beta(t - t_o)\}\exp\{j2kv_r(t - t_o).\exp\{jy_2(t - t_o)\}^2$$

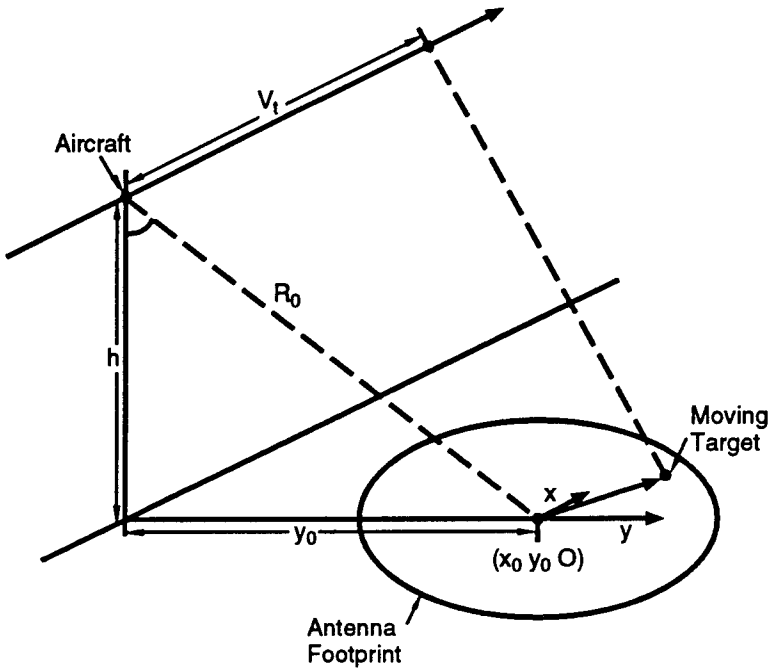

Figure 4-1. Geometry between airborne SAR and moving point target.

where

$$k = 2\pi/\lambda \text{ and } y_2 = k(|V'|^2 + a_r R_o)/R_o$$

and $s(t)$ represents the history of a moving point target, as seen just prior to azimuth compression. The first term is the azimuth antenna pattern weighting which will be expanded or contracted in width, depending on the time the target spends within the antenna beam. The second term is a Doppler shift resulting from the target velocity in the radial direction v_r. This term causes the target to be displaced in the azimuth direction in the final image. The third term is the quadratic phase variation between target and platform, containing contributions from the motions of both. This term can lead to a defocusing of the target image.

In one form of azimuth SAR processing signals from stationary targets on the ground are convoluted with a reference function which is a replica of the signature of a stationary point target. The bandwidth of waveforms received from stationary ground targets is $B = 2V\Theta/\lambda$ where Θ is the $3dB$ beamwidth of the azimuth antenna pattern.

The PRF of the transmitted frequency must be high enough to account for the Nyquist criteria for the signal bandwidth B. It is common for airborne SAR to use a PRF which is significantly greater than B, usually to improve the final signal to noise performance. In this case there will exist regions in the frequency domain outside the interval $[-B/2, +B/2]$ which contains returns from moving targets. These signals correspond to targets with radial velocity such that their Doppler shift is sufficient to take them outside the clutter bandwidth B of stationary targets. For example, consider the case when PRF $= 4B$ in which there are bands outside the clutter

bandwidth B and centered on $\pm$PRF/2 and $\pm$PRF/4. One approach is to pre-filter the received data prior to azimuth compression using a bandpass filter centered on a band outside the clutterband which is centered on zero frequency. Following the bandpass filter down sampling occurs by a factor of 2 or 4 which shifts the remaining signals onto zero Doppler. These signals can then undergo conventional azimuth compression involving convolution with a reference function centered on zero Doppler. Since the processing of over-sampled SAR signals often involves a pre-filter followed by subsampling, the difference between regular SAR and moving target processing would be only in the choice of the pre-filter band location in the frequency band. It should be noted that in moving target processing the normal clutter signals are removed by filtering, and the Doppler shifted MTI signals remain.

Figure 4-2 shows a fully focused conventional SAR image of M1/M6 motorway interchange which is situated near Rugby in England. In this image the azimuth direction runs horizontally from right to left parallel to the SAR flight path. A map of the imaged region is shown in Figure 4-3 and many common features can be identified. Figure 4-4 shows an example of an MTI image which was obtained by pre-filtering the radar data used to produce the SAR image of Figure 4-2. The pre-filter used was centered on the $\pm$ PRF/2 band followed by subsampling and the usual azimuth compression process. Geometry and scaling of the two images are identical so that they can be directly compared. Moving targets can be seen as bright features against a noise background. Good cancellation of stationary targets and clutter background has been achieved and some of the very bright features which occur along the length of the motorway in Figure 4-2 are not seen in Figure 4-4.

Figure 4-2. Conventional SAR image of the M1/M6 interchange near Rugby in England.

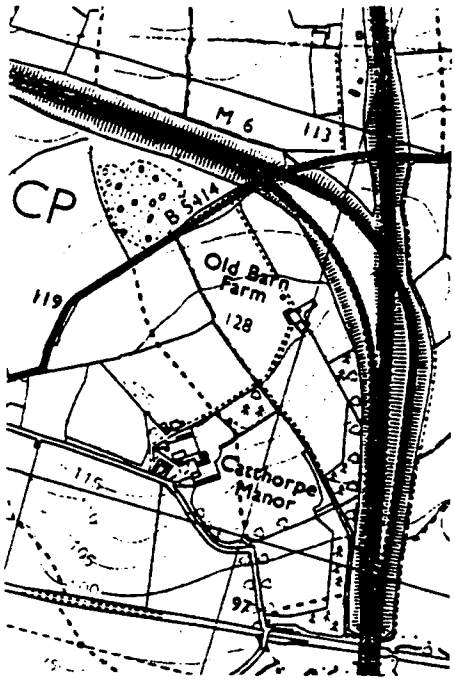

Figure 4-3. Map of the M1/M6 interchange. (Reproduced from the Ordnance Survey Map with the sanction of the Controller of H.M. Stationery Office "Crown Copyright Reserved").

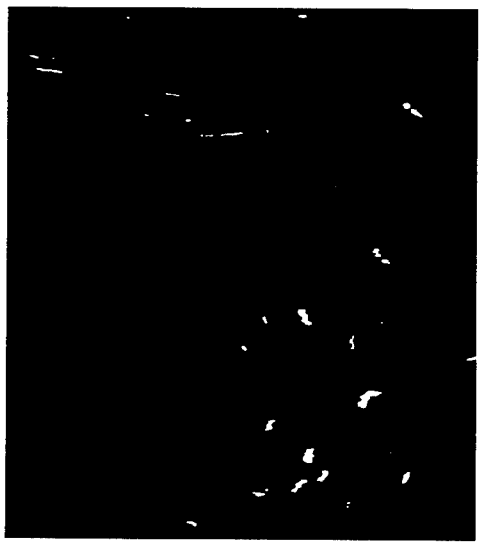

Figure 4-4. SAR image with MTI corresponding to the PRF/2 MTI band.

Freeman and Currie's method of imaging only moving targets with an SAR system with a significant degree of oversampling and hence excess Doppler bandwidth has been discussed. This method has the advantage that both the MTI and the SAR ground mapping can be done at the same time by providing two sets of pre-filters prior to azimuth compression.

An alternative method for detection of moving targets has been discussed by Chen and McGillem [23]. This method shows promise of placing moving targets at correct locations. In this method one first transforms to the frequency domain. Then one locates the band outside the narrow frequencies around the origin corresponding to stationary targets and clutter. The center frequencies of the moving target band must be determined. Next each outlying MTI band must be translated to the origin. Finally the resulting signal must be converted back to the time domain and correlated with a reference function of the conventional SAR. The correlator output will show a pattern in which the maximum amplitude is near the correct target location. Repeat for each separate moving target summing all the translated spectra together before converting to the time domain.

4.1.3 Ground Targets and Their Shadows

We discuss here one area in which the availability of great processing power and speed can very usefully extend the abilities of relatively low-powered space-based and UAV-based SARs, namely the detection of moving

ground targets (tanks, armored personnel carriers or APCs, missile transporters). These targets are fast in a specific sense: the dwell time T_o of the moving target on any one pixel is shorter than the SAR coherent integration time T_I. For a target of length l in the direction of motion and velocity u, the dwell time is defined as

$$T_o = l/u. \tag{4-10}$$

A target 5m long moving 10 m/sec has a dwell time of 0.5 sec, short compared to typical coherent integration times which range from one to a few tens of seconds. (Recall that the coherent integration time is related to the virtual antenna length L_A by $L_A = VT_I$, where V is the SAR velocity, and that the ground resolution Δx at range R is $\Delta x \sim (\lambda/L_A)R$, so high spatial resolution requires long T_I. For an X-band low earth orbit LEO SAR with $\lambda = 3$ cm, $V = 7$ km/sec, a ground resolution of 1m at range R of 10^3 km requires $T_I \approx 4$ sec.) We do not consider here truly fast targets, such as planes, cruise missiles, and rockets.

The point is, of course, that when $T_o < T_I$ the moving-target image is smeared, causing the target-to-clutter ratio to go down. (By clutter we mean the essentially stationary background scene.) In the limit $T_o << T_I$ a pixel momentarily covered by the target has a target cross-section $\sigma_T^{(u)}$ related to the stationary target pixel cross-section $\sigma_T^{(o)}$ by

$$\sigma_T^{(u)} = \sigma_T^{(0)}(T_o/T_I). \tag{4-11}$$

If this goes below the threshold ratio of σ_T/σ_c, where σ_c is the clutter cross section, the target is smeared to invisibility, and this is the problem we want to attack.

First we note that it really makes sense to go after the moving target's shadow as well as after the target itself. The reasons are:

1. A stationary shadow has a contrast ratio of σ_c/σ_n, where σ_n is the noise-equivalent cross section coming from receiver noise, ionospheric disturbances, etc. This ratio is a large and relatively unchanging value.

2. The shadow, while smeared by motion, is (essentially) at the correct ground position of the target, but the target itself is displaced in azimuth because of the extra Doppler shift it produces. This shift in azimuth displacement is

$$x^{(u)} - x^{(o)} = \frac{\lambda R}{2V}\Delta f_D = \frac{\lambda R}{2V}(\frac{2U_R f_c}{c}) = \frac{RU_R}{V} \qquad (4\text{-}12)$$

   where $\Delta\, f_D$ is the extra Doppler shift produced by the radial component U_R of target motion, and $f_c = c/\lambda$ is the central SAR frequency. This shift can be large; for $U_R = 5$ m/sec, $R = 10^3$ km, it is 700 m.

3. By use of processing which simultaneously looks for both the moving shadow and the target, the probability of detection can be raised and the probability of false alarm lowered.

We will now discuss, in general terms only, two possible means of detecting fast targets. One is based on (coherent or incoherent) superposition of subaperture scenes, each processed at a fraction of the usual coherent integration time, while the other requires some form of autofocus algorithm to recover and remove a quadratic phase error in slow time, similar in principle to the phase errors coming from errors in knowledge of platform motion.

The emphasis will be on detection of fast targets, not on imaging them. Once a moving target has been detected, further processing can sharpen the image to resolve the target. It is useful to divide the problem this way, because in many scenarios it will be of great interest merely to know that there are moving targets. For example, a battlefield commander might want to know whether there is a column of vehicles moving along a certain road, which could be studied more closely by other means in order to distinguish, e.g., tanks from APCs. Algorithms already exist for sharpening the image of already-detected, but moving targets (e.g., Stuff [1993]; Wackerman [1993]), such as a docked ship rolling from side to side.

One might ask whether all of this is necessary, and whether it is possible to use the SAR in some more conventional way as an MTI radar. For SARs with sufficient power (e.g., a large aircraft like JSTARS) to produce a detectable return from a pulse short compared to the dwell time is certainly possible, but space-based and UAV-based SARs are limited in the amount of power they can transmit, and they might be able to produce an acceptable S/N or S/C ratio only by integrating coherently over a good fraction of T_I. For example, a space-based SAR might have a pulse repetition frequency (PRF) of $10^3 - 10^4$Hz, with each chirp pulse lasting only $10^{-4} - 10^{-5}$ s. Any one pulse easily freezes the target in range, but there is inadequate signal to recover the target. Our theme here is that processing can make up for the SAR's lack of power.

Our considerations below will be on the hypothesis that the whole field of regard is illuminated at any instant by the SAR, that is, that this field has size (λ/D)R where D is the real SAR antenna aperture and that the SAR is

operated in spotlight mode. For $D = 10$ m, $\lambda = 3$ cm, $R = 1000$ km the field of regard is 3 km across. The search rate is clearly no more than the area of regard divided by T_I, say, a few km^2/sec, which is small but still potentially useful. The utility of great processing power is to keep this small search rate from being degraded by processing per spotlight frame requiring a time long compared to T_I.

4.1.4 Subaperture Processing

This scheme can use either coherent or incoherent multi-look processing. The idea is to form a number of images N at a coherent integration time which is a fraction $1/N$ of T_I; one then superimposes the images with offsets corresponding to a possible target velocity $\vec{u}$, that is, an offset of $(J/N)\mathrm{T}_I\ \vec{u}$ for the $J\ \overset{th}{-}$ subaperture image. In so doing, the azimuthal resolution goes from Δx to $N\ \Delta x$, but the full resolution can be recovered in principle if the subaperture images are superposed coherently. If the full resolution is not recovered (incoherent processing), one does not want to let $N\ \Delta x$ be bigger than the target size l. On the other hand, the new integration time T_I/N should resolve the pixel in time, which means that the dwell time l/u is comparable to T_I/N. Put together, these requirements show that for a given N, the target velocity u which can be detected is of order

$$u \approx N^2(\Delta x/T_I). \tag{4-13}$$

For $\Delta x = 1$ m, $T_I = 4$ sec, $N = 6$ will be useful against targets moving ≤ 9 m/s. This quadratic dependence means that large values of N are not

necessary. On the other hand, the incoherent processing gain with N looks is N, assuming random clutter.

If subaperture scene correlations are to be computed with FFT, it makes sense to choose $N = 2^M$ for some integer M (perhaps $M = 3, N = 8$) since the data needed for correlation at a resolution scale $N\Delta x$ are a subset of the data set at resolution Δx which go into the FFTs.

We will not go into detail on correlation algorithms, Gabor filters, and other motion-detection algorithms (e.g., Jähne [1991]). These should be implemented in such a way that, with a given hypothesis for $\vec{u}$, the correlation between the shadow and the target size is accounted for, with consideration of the azimuth shift (3).

4.1.5 Frequency-Domain Processing

As mentioned earlier, fast-time pulses even before compression are adequate to freeze the target in range. So we need only consider processing on the slow (azimuth) time scale. Our considerations will be both brief and general, so we do not discuss here the interaction of the motion-detection algorithm with all the other SAR algorithms needed in the real world (e.g., motion compensation). So the problem is just this: let $F(R, x, t)$ be the complex reflectivity of a moving target at range R and azimuth distance x, both of which are functions of slow time. Then after fast-time processing (compression, deramping, etc.), the signal for the SAR processor to deal with

is

$$\int dx F(R,x,t) \exp\left(\frac{2i\omega}{c}\frac{xVt}{R_o}\right) \tag{4-14}$$

where V is the SAR velocity (along x), R_o is the central range, and $\omega/2\pi$ is the center frequency of the SAR. To the target signal is to be added a similar return based on the clutter, with reflectivity $F_c(R,x)$ assumed independent of t. The simplest case to analyze, and the only one we deal with explicitly, is to write

$$F(R,x,t) = F(R, X - U_x t) \tag{4-15}$$

where $F(R,x)$ is a window (or top hat) function of length l in x, and the target velocity is U_x in the azimuthal variable. Generally, a target will have a component in range U_R, as well, so that R in Equation (4-15) is a function of the slow time, but we will set $U_R = O$. (This component U_R is not to be confused with the relative SAR-target range velocity, which is essentially $(x/R_o)V$ with V being the SAR velocity; of course, the relative SAR-target range velocity must not vanish in order to get the SAR to function.)

Under the hypothesis $U_R = O$, substitution of Equation (4-15) into Equation (4-14) yields

$$\int d\xi F(r,\xi) \exp\left(\frac{2i\omega}{c}\frac{t}{R_o}(\xi + U_x t)\right) \tag{4-16}$$

with $x = \xi + U_x t$. We introduce a spatial wave number q and a spatial chirp rate A via

$$q = \frac{2\omega}{c}\left(\frac{Vt}{R_o}\right), A = \frac{cU_R R_o}{4\omega V} \tag{4-17}$$

and Equation (4-16) is

$$\int d\xi F(R,\xi) e^{iq\xi + iAq^2} \tag{4-18}$$

As t ranges from O to T_I q changes from zero to a maximum value Q, which sets the azimuthal resolution:

$$Q = \frac{2\omega}{c}(\frac{VT_I}{R_o}), \Delta x \approx Q^{-1} \cdot \tag{4-19}$$

If it were not for the phase factor $\exp(iAq^2)$ in Equation (4-18), the slow-time signal would be just the Fourier transform of the target, which could be recovered with resolution as given in Equation (4-19). The quadratic phase error is, however, enormous when $T_o << T_I$. To see its effect, note that the inverse Fourier transform of Equation (4-18) involves the kernel

$$K(\xi\prime, \xi) = \frac{1}{2\pi}\int_o^Q e^{-iq(\xi\prime-\xi)+iAq^2}. \tag{4-20}$$

At $A = 0$, this is just a sine function of the required resolution. For $A \neq O$, the method of stationary phase shows that K is non-zero in the range

$$|\xi - \xi\prime| \leq 2QA = U_R T_I \tag{4-21}$$

and falls sharply to zero outside this range, at least if $Q^2A >> 1$. Since $Q^2A \sim U_R T_I/\Delta x$, this quantity is indeed large. So according to Equation (4-21) the target is smeared over a length large compared to the true length.

The problem now is the same in principle as that designed to be solved by autofocus algorithms (e.g., Curlander and McDonough [1991] [7]): remove a quadratic phase error by multiplying the Fourier transform of target plus clutter by e^{-iAq^2}. Of course, in so doing, the clutter instead of the target gets smeared. The usual autofocus algorithms form subaperture image correlations, and thus are the phase-coherent versions of subaperture processing discussed in Section 4.4. The best value of A is determined by some sort of

image intensity correlation between successive images. Another possibility is to use some simple measure of sharpening based on a reasonably high power of the intensity, such as Muller–Buffington where the figure of merit is the integral of the squared intensity. One might have to amplitude-limit the intensity to avoid spurious maxima associated with bright stationary speckle. This speckle, whose Fourier transform gets multiplied by e^{-iAq^2} during processing, becomes smeared out and thus has an effective correlation length long compared to the target length l.

In fact, intensity-based figures of merit are not likely to be very effective, since the critical length $A^{1/2}$ is not large compared to the target length l (for an X-band SAR, with $u_R = 10$ m/s, we find $A^{1/2} \approx 10$ m), and the figure of merit does not change much as the trial A is varied.

Better is an edge-detection algorithm. We have already noted in connection with Equation (4-18) that if we multiply this received SAR signal by e^{-iBq^2} and inverse Fourier transform, the result is not the true scene $F(\xi)$, but rather an apparent (blurred) scene. (From now on we will suppress the range dependence.) The smeared clutter scene we denote by $\hat{F}_c(\xi)$, which is given by:

$$\hat{F}_c(\xi) = \frac{1}{2\pi} \int d\xi' \int dq \; e^{-iq(\xi-\xi')-iBq^2} F_c(\xi'). \tag{4-22}$$

A similar expression holds for the target scene, with $B \rightarrow A - B$. We construct the difference-operated scene

$$\Delta\hat{F}_c(\xi) \equiv \frac{1}{2}(\hat{F}_c(\xi + a) - \hat{F}_c(\xi - a)) \tag{4-23}$$

where a is a length of order the resolution Δx . If the clutter has a sharp

step of unit magnitude, that is, $F_c(\xi') = \theta(\xi')$, we find

$$\Delta\hat{F}_c(\xi) = \frac{1}{2\pi}\int \frac{dq}{q} \sin qa \; e^{iq\xi - iBq^2}. \tag{4-24}$$

Let us study $\Delta\hat{F}_c$ near $\xi = 0$, where the edge is supposed to be. The range of integration in Equation (1-15) covers q values up to $Q \approx (\Delta x)^{-1}$ [see Equation (1-10)], and a itself is $O(\Delta x)$; therefore, it is a good approximation to replace $(\sin qa)/q$ by a. Then at $\xi = 0$

$$\Delta\hat{F}_c(0) \approx a(\frac{i}{4\pi B})^{1/2}. \tag{4-25}$$

The goal, it will be recalled, is to choose $B = A$, and with $a = \Delta x$, it follows [see the remarks below equation (1-12)] that $\Delta\hat{F}_c = O((\Delta x/u_R T_I)^{1/2}) \sim 0.1$. So the clutter edges are defocused and the edge detection does not see them, while a similarly sharp edge on the moving target will give a value ≈ 1 in the edge detector.

One might wish to compare this to the defocusing of an edge in square-law (photographic) detection; a sharp edge of unit strength moving with velocity u_R will show up in our edge-detection algorithm of resolution Δx at a relative strength $\Delta x/u_R T_I$ for integration time T_I.

4.2 SAR Processing for Airborne Azimuthal Scan Radars

Many airborne military radars use azimuthal scan to effect surveillance of a large area and to revisit elements of a scene rapidly. Scan rates lie in the range 1–10 rpm. Examples are periscope radars, AWACS, and battlefield area

surveillance. These radars suffer from poor azimuthal resolution associated with a real aperture.

Advances in data processing open the opportunity for these radars to use synthetic aperture processing. This will result in large gains—characteristically a factor of 100—in azimuthal resolution, while the transmitting antenna becomes smaller and cheaper. Figure 4-5 illustrates the concept. An aircraft-borne radar has an azimuthal scan period τ_o and a beam width $\Delta\phi$. Then any given scattering object is coherently illuminated for a time

$$t_o = \frac{\Delta\phi\tau_O}{2\pi + \frac{V\tau_o y_o}{r_o^2}} \tag{4-26}$$

while it lies in the antenna main beam. (Normally, the term involving the aircraft velocity V is small and we shall neglect it in our discussion. But, in actual SAR processing, such small terms still contribute phase corrections large compared to 2π and, consequently, must be retained in the processing algorithms.) While the scattering object is coherently illuminated, the aircraft flies through a length

$$L = Vt_o = \frac{V\Delta\phi\tau_o}{2\pi} \sim 150\,\mathrm{m} \tag{4-27}$$

where the representative numerical parameters are v =150 m/s, $\Delta\phi = 30°$, and $\tau_o = 10$ s. The length L is the length available for synthetic aperture processing.

The key observation of this section is that L is much longer than the physical size of aircraft antennas—roughly by a factor of -100. It follows that SAR processing will increase the azimuthal resolution while requiring a *smaller* antenna to produce a broader real aperture beam. This scheme is

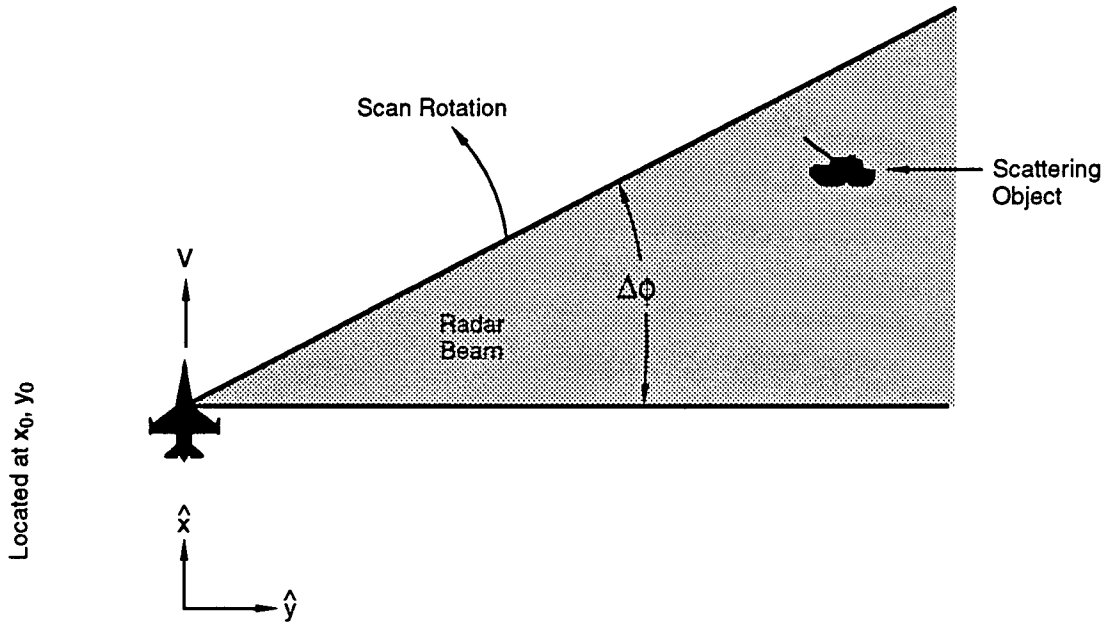

Figure 4-5. Azimuthal Scan SAR Geometry. The scattering object is coherently illuminated for a time as the antenna beam sweeps over it. While the object is illuminated, the aircraft flies through a distance $L=V\tau_0$, which is the length of the synthetic aperture.

similar to the intermittent use of conventional SAR systems in what is often called "burst" mode. In what follows, we shall investigate two applications of this principle: x-band and UHF periscope radars, and a battlefield surveillance radar. As expected, both examples promise qualitative improvements in resolution over existing systems.

4.2.1 Periscope Radars: The Case for an Azimuthal-Scan SAR

A periscope radar must continuously search the ocean surface for periscopes which emerge only briefly. A representative periscope/mast exposure is some tens of seconds. Thus periscope radars have traditionally been azimuthally scanning radars which rely on a real aperture for azimuthal resolution. On the other hand, synthetic aperture radars (SAR) have generally been implemented with side-looking beams that have no scanning capability. But the principles of SAR do not require a side-looking beam. Instead, they require that the target be coherently illuminated for a time t_o while the aircraft, with velocity V_A, flies through a distance $L = V_A t_o$ the length of the synthetic aperture. If L exceeds the physical size of the antenna, then increased azimuthal resolution will result from SAR processing. This section demonstrates that, if the antenna beamwidths of existing Navy radars are increased and the scan rate reduced, the periscope can be illuminated for a time t_o in the range 0.16 -1.6 seconds during a single scan rotation. The corresponding synthetic aperture lengths are 20 – 200 m, which greatly exceed the physical size of the antennas. These illumination times are consistent with a revisit

time τ_o = 10 sec (scan rate = 6 rpm) for azimuthal beamwidths of 0.1 -1.0 radians.

Two Navy programs are focusing on periscope radars. An Enhanced ATD seeks to upgrade the existing AN/APS-137 radar to have a user-friendly interface and to implement various discrimination algorithms which are straightforward but which require data processing capabilities that have recently become available. Most certainly, these steps should be taken. A second program has shown that, in low sea-states, periscopes can be detected by the AN/APS-145 UHF radar on the E2-C. This program seeks to study low-grazing angle returns from the sea over a range of frequencies from UHF to X-band, thereby providing a scientific basis for improving performance of both the AN/APS-137 and AN/APS-145 radars.

A common element to both programs is the use of azimuthal-scan radars which depend on real apertures to achieve azimuthal resolutions. This leads to mediocre azimuthal resolution and eliminates any doppler-velocity data. Doppler data are in fact a powerful periscope discriminant. For high-range-resolution radars, periscopes constitute a unique hard target whose radar return is short in range (less than 1 m) and exhibits little change in velocity (a guess is $\pm$ 0.05 m/sec over 1 sec). Sea spike returns, while also short in range, have a much greater doppler spread.

Hence we ask a fundamental question: "Does the requirement for azimuthal scan preclude useful doppler data processing?" Let us note that synthetic aperture radar (SAR) processing is equivalent to doppler-processing; they differ only in the way data is displayed and axes are labeled. Thus our

question reduces to: can SAR processing be used in an azimuthally scanned radar? In order to effect SAR processing, the target must remain illuminated while the airplane flies along the synthesized aperture. To make this aperture long, one can reduce both the scan rate and broaden the azimuthal beam width.

On the other hand, the need to continuously monitor the ocean sets a lower-limit on the scan rate. We shall adopt a revisit time $\tau_o \approx 10$ sec which corresponds to a scan rate of 6 rpm. Both radars operate routinely at 6 rpm.

The design issues regarding SAR processing of azimuthally scanned radars are analyzed below. We find that this mode leads to qualitative improvements in the size of the clutter patch, which is equivalent to high-accuracy doppler velocity resolution. It seems to us that the conventional SAR display is the most understandable way to present doppler data. For illustrative purposes, we shall carry out two point designs – one at X-band for parameters corresponding to the AN/APS-137 and one at UHF for the AN/APS-145. Table 4.1 gives the parameters. For the AN/APS-145 we shall carry out examples for bandwidths of 6.25 MHz and 40 MHz.

Our evaluation of SAR processing will be an adaption of standard arguments, as found in the text by N. Levanon [25]. As the azimuthal beamwidth becomes larger, the doppler spread $\Delta\nu_D$ associated with the beam width $\Delta\phi$ increases. The Nyquist theorem requires that the pulse-repetition frequency ν_s exceed twice the doppler spread

$$\nu_s \geq 2\Delta\nu_D = \frac{4V_A}{\lambda}\sin\phi\Delta\phi \tag{4-28}$$

Table 4.1 Radar Parameters, Azimuthal-Scan SAR Mode

Parameter	AN/APS-137	AN/APS-145
Frequency	9.8 GHz	430 MHz
Scan Rate	6 rpm	6 rpm
Bandwidth	500 MHz	40.MHZ
		6.25 MHz
Pulse Repetition Frequency	2000 Hz	300 Hz
Polarization	Horizontal	Horizontal
Azimuthal beamwidth	0.10 rad	0.38 rad
Elevation beamwidth	0.10 rad	0.8 rad
Antenna Gain	1000	40
Illumination time	0.16 s	0.60 s
Aircraft velocity	150 m/s	150 m/s
Synthetic aperture length	25 m	90 m
Azimuthal resolution+	20 m	125 m
Minimum radial velocity	10 cm/s	60 cm/s
Range resolution	0.5 m	7.5m
		50m
Peak Power	0.5 MW	1.0 MW
Pulse Length τ_P	0.5 ms	12.8 ms
Unambiguous range	75 km	500 km
Number of coherent pulses	320	180
Coherent signal-to-noise** ($\sigma = 1$ m^2, R=30 km)	$4 \cdot 10^3$	10^5

* The AN/APS-145 has the frequency agility to operate between 406 MHz and 446 MHz. In regular operations, it uses channels of 6.35 MHz band width.

+ Evaluated at R=30 km; linearly proportional to R.

** Noise temperature = 600°K, evaluated at 30 km, proportional to R^{-4}.

where V_A denotes the aircraft velocity. Thus, the pulse-repetition-frequency determines the maximum azimuthal beamwidth

$$\Delta\phi = \frac{\lambda\nu_s}{4V_A}. \tag{4-29}$$

The length L of the synthetic aperture is

$$L = V_A t_o = \frac{(\Delta\phi)\tau_o V_A}{2\pi} = \frac{\lambda\nu_s\tau_o}{8\pi} \tag{4-30}$$

where $t_o = (\Delta\phi)\tau_o/2\pi$ is the illumination time for a point on the sea. Then the along-track azimuthal resolution is

$$\delta y = \frac{\lambda R}{2L\sin\phi} = \frac{4\pi R}{\nu_s\tau_o\sin\phi}. \tag{4-31}$$

It is more precise to cast Equation (4-31) in terms of a resolution cell in $\cos\phi$.

$$\delta(\cos\phi) = \frac{4\pi}{\nu_s\tau_o}. \tag{4-32}$$

Interestingly, because of our Doppler requirement, the along-track angular resolution depends only on the number of coherent pules in a revisit time: $M' = \nu_s\tau_0$.

Thus SAR processing vastly increases the azimuthal resolution over real aperture processing. One need only compare the synthetic aperture lengths of Table 4.1 with the real aperture length of the AN/APS-137 (1.1 m) and AN/APS-145 (7.0 m).

How does the unknown radial periscope velocity affect this analysis? The relation between radial velocity v_r and along-track-offset Δy is

$$\Delta y = \frac{v_r}{V_A}R \tag{4-33}$$

which becomes equal to azimuthal resolution when

$$v_r = \frac{V_A 4\pi}{\nu_s \tau_o} = (v_r)_{\min} \tag{4-34}$$

where $(v_r)_{\min}$ is the velocity corresponding to the minimum resolvable doppler shift in time t_o. Thus a steady radial velocity of 10 knots (5 m/s) can result in a position offset of 1 km at R = 30 km. But as long as the radial velocity dispersion of the periscope does not exceed $(v_r)_{\min}$ in the illumination time t_o, this dispersion will not smear the azimuthal resolution computed via Equation (4-31). Table 4.1 gives values of $(v_r)_{\min}$. A practical estimate suggests that periscope radial velocity dispersion occurring within the illumination time t_o will not affect azimuthal resolution. The velocity dispersion of sea spikes is roughly 3 m/sec, so they will be spread over a number of azimuthal resolution cells, and thereby be distinguished from periscopes.

For periscope detection, one does not particularly care about the azimuthal offset resulting from radial velocity. The key contribution of SAR processing is to exploit the low velocity dispersion of the hard target and thereby achieve high azimuthal resolution. Other ocean radar targets are likely to have considerable velocity dispersion and thus be smeared over many azimuthal radar cells. Low velocity dispersion is a key discriminant for periscopes.

One should also ask whether periscope velocity will result in range walk (or azimuthal-cell-walk) in an illumination time t_o. Based on a maximum submarine velocity of 5 m/s the answer is no, but just barely so in the case of radial velocity for the AN/APS-137.

Table 4.2 SAR Performance of the AN/APS-145 with ν_s=800 Hz

Parameter Value	Value
Azimuthal Beamwidth	0.95 radians
Illumination time τ_0	1.3
Synthetic Aperture Length	200m
Azimuthal Resolution*	50m
Minimum Radial Velocity	30 cm/sec
Unambiguous Range	200 km
Coherent Signal-to-Noise*	$3 \cdot 10^5$

*Evaluated at $R = 30$ km

Our treatment has considered the periscope a hard target. In reality, radar returns from periscopes, especially at X-band frequency where the wavelength is small compared to the periscope, involve a reflection off the periscope and a second reflection off specular patches of the sea surface. Motion of the sea surface introduces phase changes into this path, which translate into doppler shifts and azimuthal smearing. At low grazing angles, the additional path length will be small and estimates indicate that doppler shifts should not exceed $(v_r)_{\min}$ of Tables 4.1 and 4.2. Briefly, the argument proceeds as follows: the extra path length ΔP associated with reflection off the sea surface is roughly $\Delta P \approx 2\text{h} \sin\theta$ where $h \sim 1$ m is the height of the reflecting patch on the periscope above the ocean surface and θ the grazing angle. Then the variation in path length associated with changes in the ocean surface height ζ will be (for $\theta << 1$)

$$< (\Delta P)^2 >= 4\zeta^2\theta^2 = 4 < S_k^2 > \frac{\theta^2}{k^2}$$

where $< S_k^2 >= B = 6 \cdot 10^{-3}$ is the mean square slope per logarithmic wave number interval, as determined by ocean measurements. The dispersion in

doppler shift associated with the time variation of extra path length is

$$\Delta\nu_d \approx \left(\frac{\partial\omega}{\partial k}\right)\left(\frac{\Delta k}{k}\right)\frac{2 < S_k^2 >^{1/2}}{\lambda}\theta \approx \left(\frac{g}{k}\right)^{1/2}\left(\frac{\Delta k}{k}\right)\frac{< S_k^2 >^{1/2}\,\theta}{\lambda},$$

where for ocean waves $\omega = \sqrt{gk}$.

Let us estimate that $k \sim \Delta k \sim \theta/h$. Then the criterion that the doppler shift dispersion be negligible during a coherent integration time t_o is

$$\Delta\nu_d t_o = \sqrt{g\ h\ B}\ \ t_o\ \sqrt{\theta}/\lambda \approx 8(\frac{t_o}{1\ \mathrm{sec}})\sqrt{\theta} < 1$$

where we have used $\lambda = 3$ cm, t_o= 0.10 s appropriate to the AN-APS 137 radar. Thus, for grazing angles $\theta < 1$ radian, we should expect little azimuthal smearing arising from doppler shift associated with ocean surface motion. On the other hand, at UHF frequencies there are direct returns from the periscope, which is comparable in size to a wavelength, and ocean displacements constitute a smaller fraction of a wavelength. Thus, the UHF radar should be less affected by time dependence of the sea surface reflection. Experimental data are needed, however.

Let us next turn to the coherent signal-to-noise estimate. The usual radar equation gives

$$\frac{S}{N} = M\frac{P_T\tau_P\sigma G^2\lambda^2}{(4\pi)^3R^4T_N} \tag{4-35}$$

where the antenna gains of Table 4.1 are based on the beamwidths needed for SAR and

$$M = \nu_s t_o = \frac{\nu_s^2\lambda\tau_o}{8\pi V_a} \tag{4-36}$$

is the number of coherent pulses. The values $\sigma = 1$ m^2, $T_N = 600$ K are assumed. Table 4.1 shows that the signal-to-noise ratio is very high, so that

cross-section degradation by radar absorbing material (at most a factor-of-100 reduction for the AN/APS-137) will still leave a healthy signal-to-noise ratio. At UHF, radar absorbing material is thought to be ineffective because the periscope size is comparable to a wavelength.

The pulse repetition frequency choice in Table 4.1 for the UHF AN/APS-145 radar is not optimum. A value $\nu_s = 300$ Hz was adopted because it is the usual PRF for this radar. Periscope SAR performance would be improved by raising this value to $\nu_s = 800$ Hz yielding an unambiguous range of 200 km—quite adequate to the ASW task. Table 4.2 shows the resultant improvements, assuming fixed average power. These parameters yield a 2500 m^2 clutter patch at 30 km.

A research program in SAR processing of periscope radar data could be undertaken with an existing AN/APS-145 radar which has an azimuthal beamwidth $\Delta\phi = 0.1$ radian. A sufficiently long illumination time will result if the antenna scan rate is slowed to 1 rpm. Of course, a revisit time of 60 seconds is too long for an operational radar, but all the other parameters of Tables 4.1 and 4.2 should be realized and enable a demonstration of the gains associated with SAR processing. With the narrow beamwidth, the nominal pulse repetition frequency $\nu_s = 300$ Hz easily satisfies the Nyquist criterion (5.1). All one needs for SAR periscope detection is to digitize the received signal at a rate exceeding 20 MHz and apply SAR processing.

In brief, we have shown that with minimal modifications—basically a *smaller* antenna with increased azimuthal beamwidth—and the addition of SAR processing, the AN/APS-137 and AN/APS-145 can be operated in a

novel mode called an azimuthal-scan SAR. Qualitative reductions in the size of the clutter patch to 10 m^2 and 2500 m^2 respectively are obtained. Given the reported very low values of $\sigma_o < 10^{-5}$ for UHF grazing angle measurements [37], both radars should have a very high signal-to-clutter ratio. Thus periscope detection is assured. Periscope discrimination should also be greatly aided because the hard-target is confined to a single range resolution cell. Radial velocity spreads exceeding the minimum radial velocity of Table 4.2 will spread other ocean returns, such as sea spikes, over several resolution cells. Additional discriminants, as set forth in the Enhanced ATD for periscope radar, of single-range-cell echos, tracking, etc. should clearly be brought to bear on the discrimination task. This is particularly so for the AN/APS-145 radar with a bandwidth of 6.25 MHz. With these parameters, the range resolution cell exceeds the size of many surface ships. In the context of discrimination, one can view the ideas set forth above as a scheme to implement doppler discrimination in an azimuthally scanned device.

We recommend further development and experimental tests of the azimuthal-scan SAR mode. Tables 4.1 and 4.2 indicate that the E2-C AN/APS-145 radar would probably be the better long-range periscope radar (R > 75 km), while the AN/APS-137 can yield highly accurate periscope position for shorter ranges. Other improvements are possible. For example, the high signal-to-noise ratio would permit subdivision of the AN-APS 137 in 4 antennas, spaced 90° in azimuth and transmitting orthogonal Costas waveforms. This would reduce the revisit time to 2.5 secs.

4.3 Battlefield Scanning SAR

High resolution battlefield scanning radars constitute a simple application of the principles of SAR processing of azimuthal scan radars. Consider an aircraft-borne X-band azimuthal scanning radar with a scan period of 40 s and an azimuthal beam width $\Delta\phi = 15°$. The coherent illumination time is then $t_a = 1.6$ s and the synthetic aperture length L $\approx$ 200 m. With a bandwidth $B = 500$ MHz, this system produces a resolution of 0.6 m $\times$ 0.6 m at a range of 10 km. An average power $< p > = 1$ kw yields a signal-to-noise ratio S/N $\approx$ 200. The PRF = 5 kHz. The Doppler shift across the scene corresponds to 40 m/s: sufficient to enable moving objects to be identified, but not located in azimuthal following the principle of Section 4.1.

The computational load calls for one 32 k $\times$ 32 k (10 km $\times$ 10 km) image every 20 seconds. If moving targets are to be identified, then the processing time per image must drop to $\approx$ 0.04 s; since roughly 500 combinations of target radial and azimuthal velocities must be tried.

Given the reasonable power requirements and small antenna size ($\approx$ 6 inch in diameter), this SAR could readily be based in an RPV. Broadcast of the (encrypted) SAR data stream would enable local users to create SAR images on the battfield within a (30 mile $\times$ 30 mile) area. These images will have the highest resolution for areas broadside to SAR aircraft/RPV.

It is reasonable that local control over its flight bearing will enable local commanders to achieve SAR imaging with a 1 minute response time.

Battlefield surveillance can also be carried out from space by satellite SAR's. An example of a stripmap mode SAR was described in Section 3.8, where we found that a modest data transmission rate of the order of 4 MB/s $\approx$ 32 bit/s is needed.

4.4 Measurement of the Atmosphere and the Ionsphere

The effect on SAR phase of the ionosphere/atmosphere system was estimated in Section 2.8. Here we will use those estimates in a positive way; a large estimate in Section 2.8 meant that SAR images would be distorted or destroyed because of phase decoherence. Here we note that a large estimate makes it feasible for SAR to be used as a measuring tool.

Any large retroreflector, whether deliberately placed or taken from a target of opportunity, provides a probe of the ionosphere. If the phase of the return from one pixel can be measured in a very short time, then the time record of that phase is an image of ionospheric electron-density fluctuations projected to that pixel. That is, at each time a line integral of the refractive-index fluctuations is obtained. A calculation of the minimum time necessary to obtain the signal-to-noise required to measure the phase should be done. It will depend on the radar power and on the physical aperture.

A strong identifier of ionospheric effects could be obtained if more than one frequency were being analysed. The ionospheric effect increases strongly with increasing wavelength. Other effects, including the neutral atmosphere,

but also including fixed path effects in a complicated environment, will have a very different dependence on radar wavelength.

It would be very exciting to the ionospheric community to have these kind of measurements made on a continuing basis. At present the available measurements come from a satellite devoted exclusively to that task (HILAT) and which also requires ground stations. Therefore the simultaneous correlations that could be obtained in both space and time would be invaluable in studying the dynamics of the ionosphere.

Monitoring the lower atmosphere also has its adherents. In this age of climate monitoring, detailed information on the scales that SAR could access are just what General Circulation Models (GCMs) need at this time. Their greatest uncertainty has to do with water vapor, and it is important that the effects measured will be sensitive to the water vapor content of the atmosphere.

We cannot tell ahead of time how valuable the SAR measurements of, for example, substantial weather events, would be, but we can say that many researchers would be eager to get their hands on the data to attempt to wring some new insight from them. One can imagine different types of looks at hurricanes, tornadoes, fronts, storms at sea, effects of islands, etc...

4.5 SAR for Measuring Land and Ocean Characteristics

4.5.1 Overview of SAR and Environment Science

Visible and IR multispectral images collected by spacecraft have been exploited for environmental science for about 30 years, but spacecraft radar images have only been available since 1978, and then with a 14 year hiatus between the 100 day mission of Seasat in 1978 and the launch of ERS-1 in July of 1992. Thus, the use of SAR for evironmental work has been hampered for lack of spacecraft data. That situation is changing fast. In the civil community ERS-1 has been joined by the Japanese JERS-1 and two more SAR instruments are planned for the joint US/Canadian Radarsat and ERS-2 from the European Space Agency (ESA). Synthetic aperture radar has two very important advantages for environmental sensing – images can be collected through clouds and at night. Visible and infrared sensors are severely limited by clouds and darkness, though thermal infrared images can be collected at night. This is because the microwave radiation used by SAR is generally at too long a wavelength to be affected by the very small water droplets in clouds. SAR is an active sensor and thus carriers its own illumination source. The longer wavelength of SAR ($\approx$ a few meters to a centimeter and less) makes it sensitive to different surface characteristics than visible or infrared sensors which operate at wavelengths in the fractions of a micron to tens of microns range. These advantages are leading to many

new observational opportunities (e.g. in the cloud covered tropics and polar night,) and new types of data, such as topographic maps from interferometric SAR (INSAR). SAR is making strong impacts in oceanography, geology, vegetation studies and other areas, as discussed below.

As we shall see below, exploitation of SAR data for environmental applications can benefit greatly from the increased computational power offered by parallel architectures. The formation of the image itself is a computation intensive task and the use of interferometric and multiple frequency and polarization data sets further increases (by an order of magnitude or more) the need for massively parallel machines to extract geophysical measurements from the SAR observations.

4.5.2 What SAR can do that "photography" can't

As discussed above, SAR carrying its own illumination source and operating at microwave frequencies can perform observations under conditions where visible and/or infrared observations are impossible. Imaging scenes at night with performance equal to daytime observations allows exploration of polar regions during the winter as well as investigation of day/night differences in ocean and vegetation processes. Perhaps a more important advantage is microwave radiation penetration of clouds. Landsat and other visible/IR sensor platforms are often so hampered by cloud cover that scenes of some regions, especially in the tropics and polar regions, are collected only a few times per year if at all. SAR allows observation on a planned schedule

without regard to cloud cover. SAR signals can often penetrate smoke, dust and fog that obscure scenes for visible/IR sensors.

A more subtle advantage is the ability to collect images with both amplitude and phase infomation (complex imagery). This allows excellent topographic measurements that can be used to detect small changes in surface shape over large regions as well as the ability to measure velocity. Since the signal source is carried with the sensor, more control of observational parameters is available in terms of geometry, frequency and polarization. This control is very useful for observing different roughness scales on the surface being observed. Below we illustrate these advantages with a few examples showing both the advantages of SAR as well as the need for processing by massively parallel machines.

At the forefront of SAR applications is the use of phase information. Fundamentally SAR image pixels have both an amplitude and a phase. The conventional SAR image plots the intensity (or amplitude squared) of each pixel and the phase is ignored. The application of phase information requires significant additional computation for useful interpretation and is thus greatly aided by faster computation.

Phase information can be used in two principal ways. First, interferometric SAR from two, slightly displaced SAR trajectories or two antennas on the same SAR platform, to obtain topographic information on the surface imaged and second, change detection by measurement of the magnitude of the complex correlation between complex SAR images collected at two different times to obtain information on surfaces that have been disturbed. The first

application allows one to make topographic maps of areas that are difficult to observe otherwise and the second allows one to observe subtle changes on the order of the radar wavelength. The two techniques are closely related. Below we illustrate the topographic application and a change detection example is given in Section 4.9 below.

4.5.3 Example Applications in Environmental Science

In this subsection we list some of the prominent environmental applications of SAR and discuss two examples in more detail to illustrate the role of computational complexity and the likely benefits of massively parallel computation. We divide the examples into two parts: land and sea.

Land remote sensing

Initially this was the primary environmental application of SAR. SAR has been used for mapping large portions of tropical countries where cloud cover or fog and mist prevent efficient mapping by other means. SAR images at a number of different frequencies have been used to map land use, soil moisture, crop or natural vegetation cover as well as estimating snow cover. Recent images of tropical rain forests show the effects of land clearing deforestation on a regular basis, unhampered by cloud cover. Currently great efforts are being made to see if SAR can be used to estimate biomass in areas where other means are difficult because of cloud cover or vegetation type.

One of the newest applications of SAR uses pairs of complex images, collected from slightly different SAR platform trajectories or from a SAR with two antennas displaced perpendicular to the flight velocity vector. The process is briefly described below.

Interferometric SAR (or INSAR) relies on well known principles of synthetic aperture radar to produce a two-dimensional map of a surface, but rather than the customary signal intensity image, $I(x, y)$, a phase difference map $\Delta\phi(x, y)$, is produced. The coordinates x, y, z are the customary horizontal and vertical directions respectively on the Earth's surface. This phase difference map $\Delta\phi(x, y)$ corresponds to echo phase maps $\phi_1(x, y)$ and $\phi_2(x, y)$ collected at two points separated by a distance perpendicular to the SAR flight path, thus a topographic map of the imaged area can be obtained. In the introductory discussion below SEASAT SAR data of ≈ 25 meter resolution are used as examples.

The phase difference map, i.e., $\Delta\phi(x, y)$, is obtained by registering the two complex SAR images collected, and then simply taking the difference of the phases associated with two complex images. It is important to obtain accurate phase estimates for each image of the pair, so some careful averaging of pixels is necessary to overcome the speckle noise inherent in SAR images.

Space-differential-interferometric SAR produces, as the basic data set, interference fringes of the type shown in Figure 4-6(a). The process of extracting topographic information from the fringe line pattern of this figure is somewhat involved and a number of novel ideas have been used to deal with the phase unwrapping problem. Work by Goldstein, Zebker, and Werner

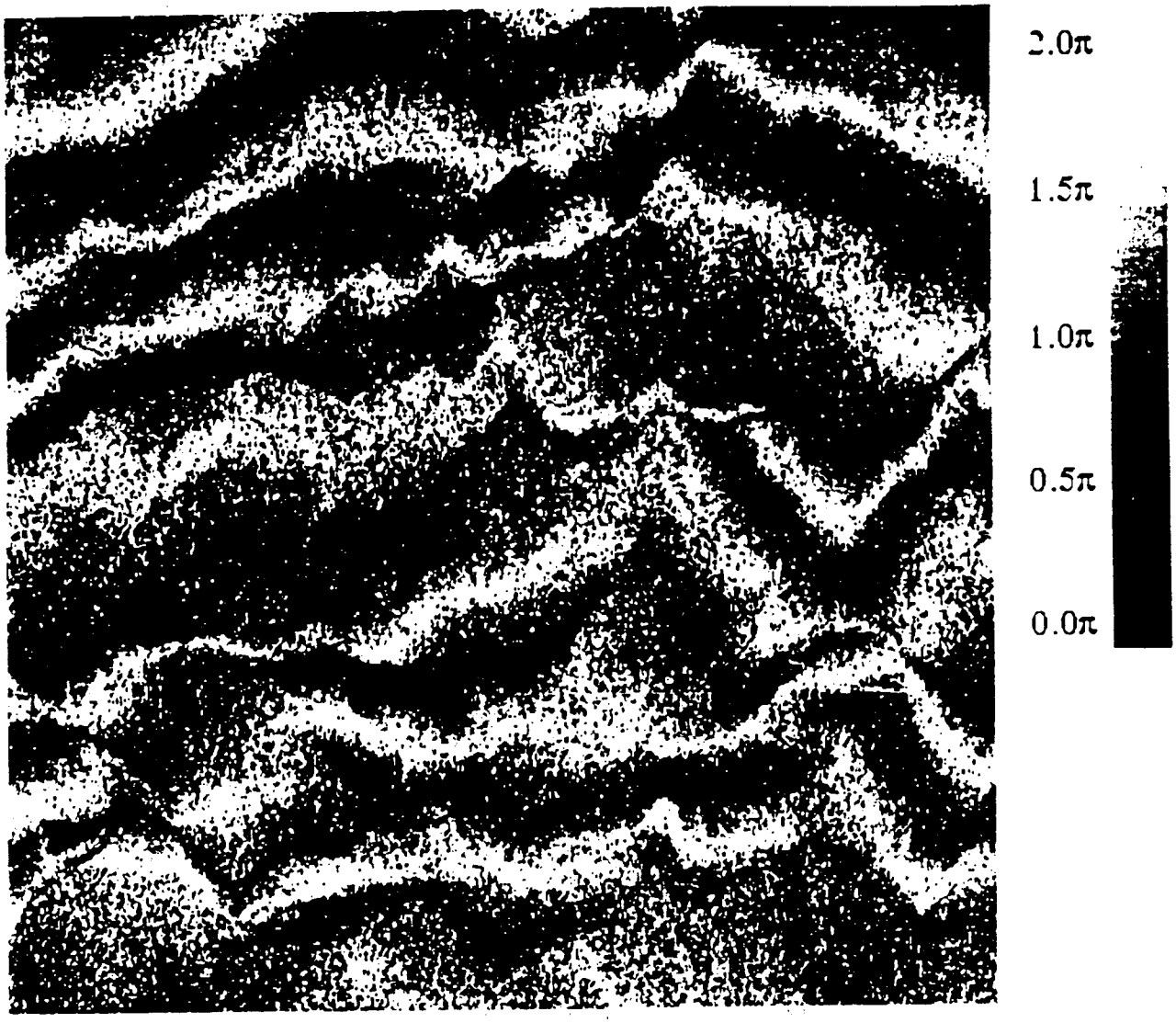

Figure 4-6(a). The phase difference map of SEASAT SAR images from orbits 1334 and 1420 when the complex SAR images are correctly registered. The spacing between the interference fringes is determined by the terrain and observational parameters, including the baseline length, i.e. the separation between the two observations. The baseline length in this case is 75 meters. The interference fringe pattern is modulated by the image terrain. (After Lin, Vesecky & Zebker, 1992)

(1988),[5] Prati et al. (1990),[26] and Lin, Vesecky, and Zebker (1992)[27] illustrates some of the ideas put forward. At present, there is no "classical" algorithm that is widely used.

Comparisons of INSAR topography and surface measurements have been made in only a few cases. Under good conditions, such as in a desert region with little vegetation, the topographic accuracy is likely to be very good; probably on the order of a few meters or less. However, in high-relief regions with large vegetation the accuracy is likely to be significantly less. For example, Lin (1992) [28] compared SEASAT INSAR topography of the high-relief area shown in Figure 4-6(a) with a USGS digital terrain map (DTM). The RMS error between the two is about 80 m. While this may seem large, one must recognize the many sources of error present. For example, the DTM is likely to have an RMS error on the order of the error quoted above. Further, the DTM is likely to be based on stereo photography from aircraft and thus gives tree-top height. This area has many large trees. The radar may penetrate somewhat into the vegetation. Further, the data used to produce the DTM was collected many years before the SAR data.

In addition to the formation of two complex SAR images, very significant data processing is required to extract topographic or Doppler information. In the case of topographic information much extra processing is required. For example, in the algorithm of Lin et al. (1992), the following operations are required:

1. Image registration (all pixels)

2. Fringe line location (significant fraction of pixels)

3. Lay over correction (some pixels, scene dependent)

4. Height extraction (all pixels)

Each of these steps requires substantial computation. The message here is that extraction of height information from INSAR multiplies the data processing load by at least a few times the original amount required to form the complex images in the first place.

In Figures 4-6(b) and 4-6(c), an INSAR topographic map of a portion of Death Valley is compared to a USGS topographic map of the same region. Although detailed comparison with surface measurements have not been made, it is thought that the INSAR topography is accurate to about a meter or two. Repeated INSAR observations deviate very little from one another.

Ocean remote sensing

SAR applications include the measurement of ocean waves (directional wave height spectra), winds, internal wave surface effects, surface film distribution, sea, ice, underwater topography (in shallow water). The measurement of ocean currents is a subject of current research. An example of ocean remote sensing that illustrates the benefits of massively parallel computing is the classification of sea ice types with multipolarization, multifrequency SAR.

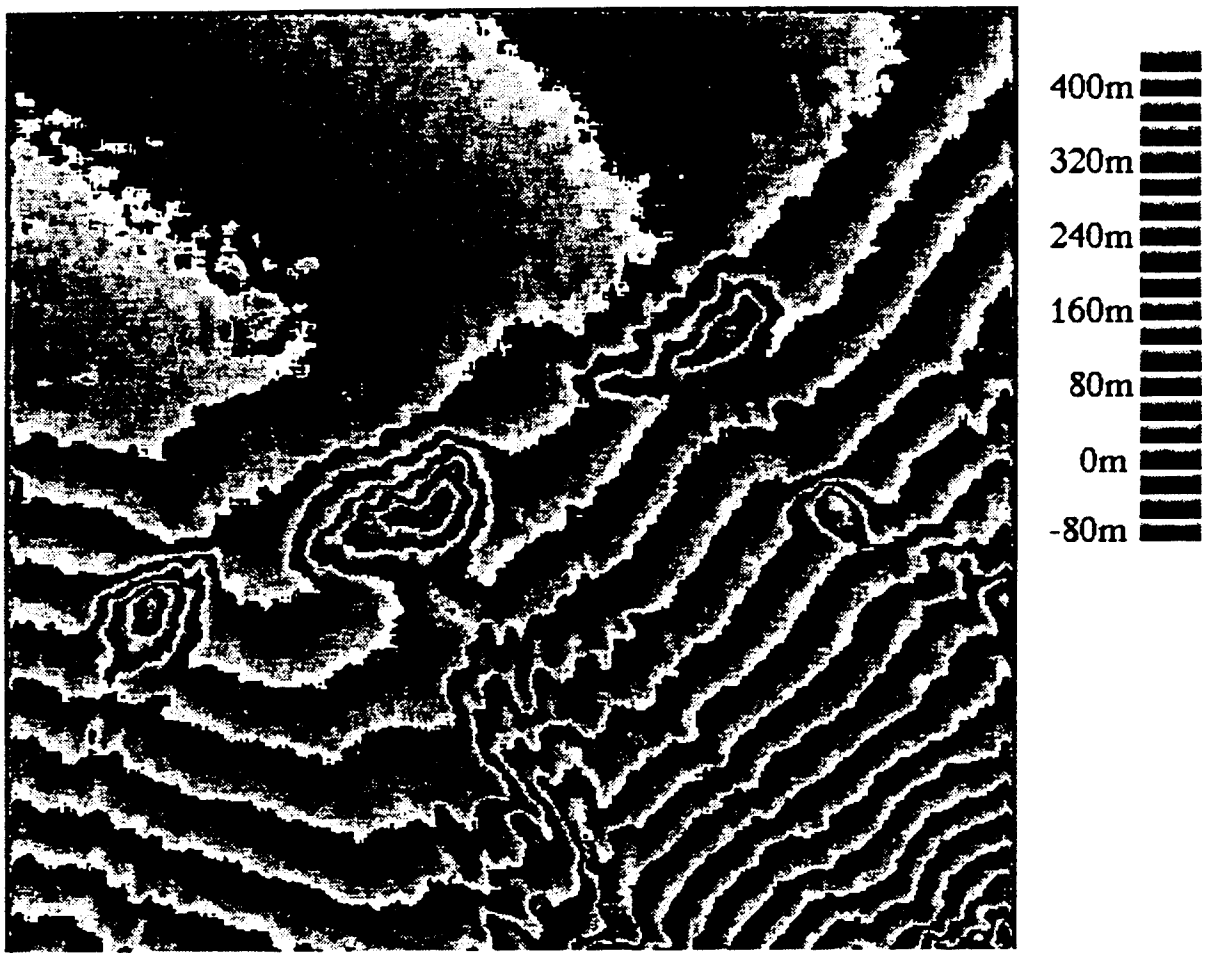

Figure 4-6(b). INSAR elevation map of area in Death Valley represented in contour form. The contour interval is 25.5 meters. After Lin (1992).

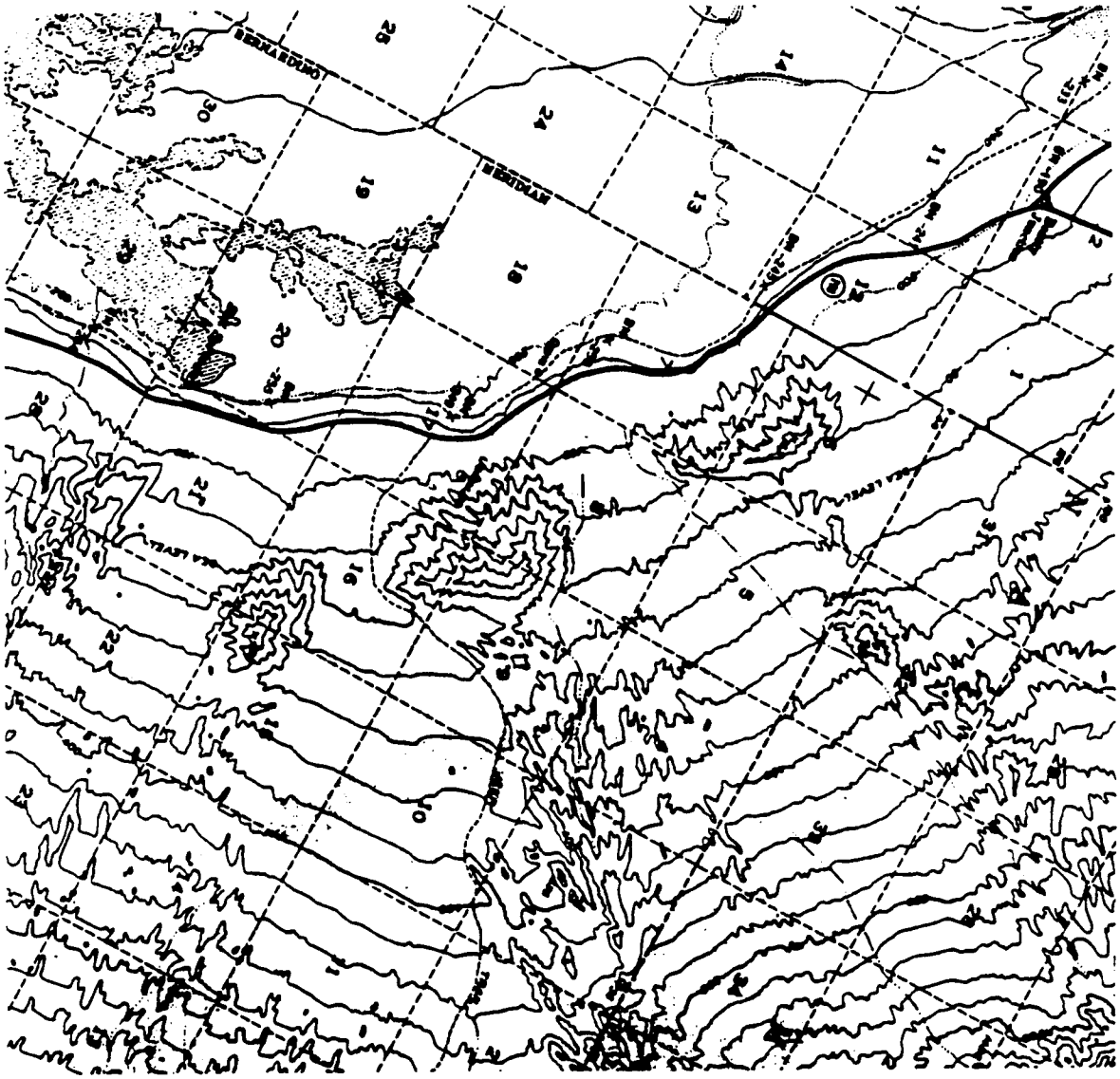

Figure 4-6(c). USGS contour map of Death Valley area shown in Figure 4-6(a). Note three small hills near center. After Lin (1992).

Sea ice covers large areas in the polar regions, affecting weather and climate as well as transportation and military operations. One element that is important for all these purposes is ice thickness which ranges from millimeters for new ice to several meters for multiyear flows. SAR can be used for ice classification and is particularly useful because observations can be made during the polar night and through the heavy cloud cover of many polar locations. Sea ice can be classified into many categories, but the main four are as follows:

1. Open water (no ice cover)
2. Thin new ice (of the order of a centimeter)
3. First year ice (from tens of centimeters to a meter or so)
4. Multiyear ice (up to several meters).

Multiyear ice has survived at least one summer melt season.

Some of the important issues in sea ice science and applications are sea ice extent (area covered) and thickness. The extent is important since an area of ocean covered with sea ice allows much less heat transfer between the ocean and the atmosphere. Further, sea ice has a higher albedo that ocean water and thus reflects more of the sun's energy back out into space. Regions covered with sea ice restrict the movement of ships and can endanger offshore engineering structures, such as oil drilling and production rigs. Ice classification is important here since the thicker multiyear ice is more likely to impede shipping and damage offshore structures. Remote sensing by synthetic aperture radar allows one to survey sea ice over very large regions and

as we shall see below classify the ice observed rather well. The simplest SAR observations involve a single frequency radar and are able to distinguish between open water, first-year ice and multi-year ice. Increased computational power allows one to use multifrequency, multipolarization radar and complex analysis algorithms to make a more accurate diagnosis of ice coverage and type adding to the science and applications value of the observations.

An excellent example of sophisticated sea ice classification is that done by Rignot and Drinkwater [51]. They used SAR images in which each pixel was represented by a vector of information containing full polarimetric (complex scattering matrix) information at three SAR frequencies P- ($\lambda \approx 68$ cm), L- ($\lambda \approx 24$ cm) and C- ($\lambda \approx 5.6$ cm) band frequencies. This yields about 18 nonredundant information channels (including amplitude and phase) for each pixel. Using subsets of this information (L- and C-band polarimetric data) and a maximum apriori classification scheme Rignot and Drinkwater produced an excellent classification map (90% accuracy) involving six classes as follows:

1. CFY = compressed first year ice
2. FYRR = first year ice with ridges and rubble
3. MY = multiyear ice
4. FYR = rough first year ice
5. FYS = smooth first year ice
6. ThI = Thin ice.

Results for an approximately 7 × 10 km ice region are shown in Figure 4-7. These images were collected by the JPL AIRSAR instrument carried on a DC-8 aircraft. Hence the angle of incidence changes from the near range (top) of the images to the far range (bottom) of the images. In the left panels we have the single polarization images at C- and L- band. In the higher frequency C-band image the multiyear flows show up as bright due to volume scattering in top of the ice. At L- band these floes appear dark. It is clear that the top or bottom left images yield only limited classification information. By using the multiple frequency and polarization information and the MAP classification scheme six well defined ice types can be reliably distinguished. The improvement is evident in the classification map at upper right in Figure 4-7. The lower right panel shows a radiometer image that also allows ice classification, but at lower resolution. Note the agreement between the two right panels.

From this we conclude that much improved scientific and applications information can be provided by advanced sensors with multiple information channels. However, it is massively parallel computation capability that will allow the data from such instruments to be reduced and analyzed on a large scale and in a timely manner so that the full fruit of the instrument can be harvested.

Atmospheric remote sensing is not one of the principal applications of SAR at the present time. However, in Section 2.7 above we discuss the phase distortion introduced by fluctuations in the ionosphere and atmospheric boundary layer within a hundred meters to a kilometer from the

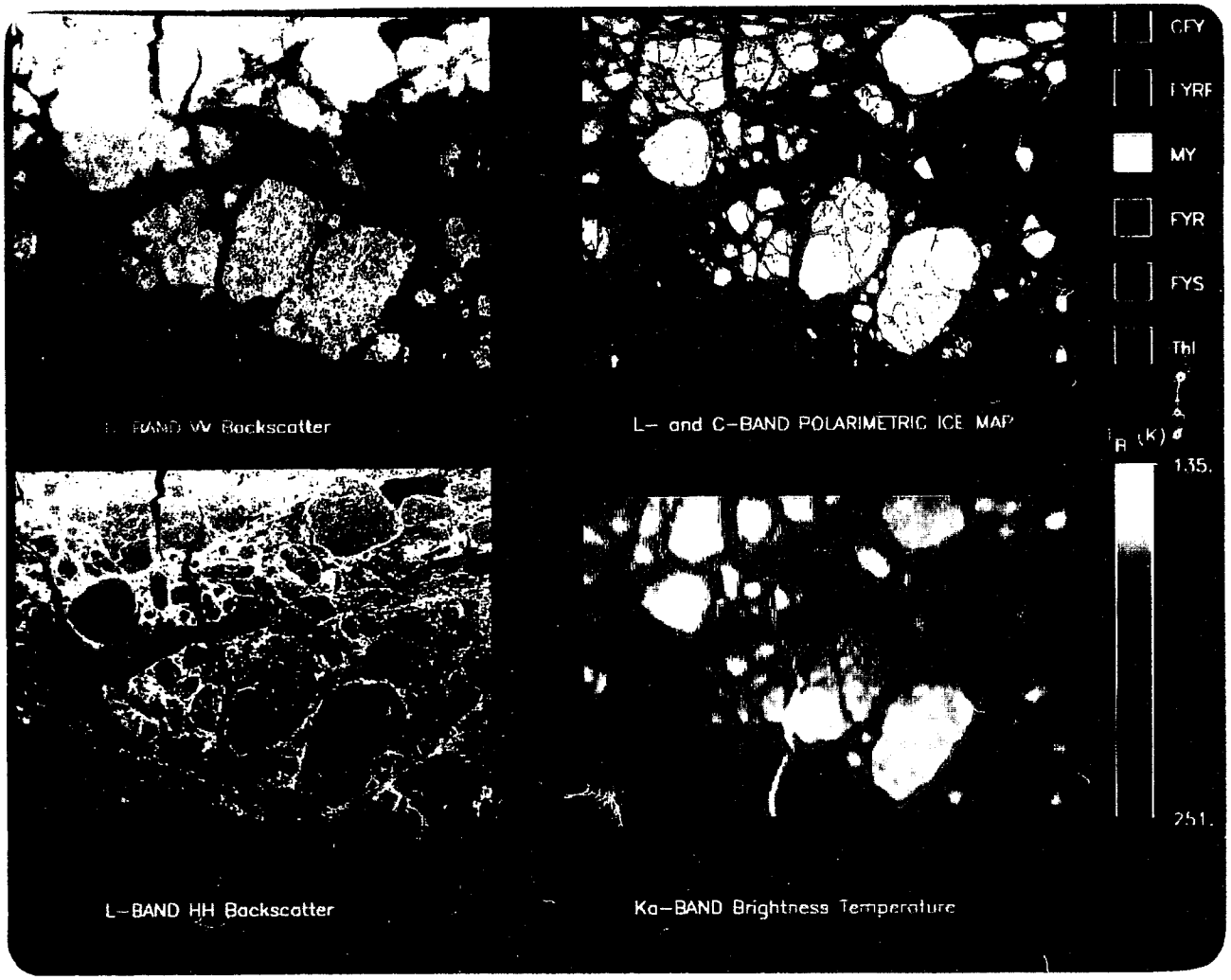

Figure 4-7 Example of coregistered C and L band SAR images of sea ice collected over the Beaufort sea by the JPL AIRSÁR synthetic aperture radar during March, 1988. The left panels illustrated the useful, but limited capabilities of either L and C band single polarization images taken alone. The upper right panel shows the sea ice classification into six types done by using fully polarimetric L and C band together in a maximum apriori classification scheme. The lower right panel shows classification data from a radiometer instrument at lower resolution. (Figure kindly provided by M. Drinkwater, Jet Propulsion Laboratory.)

surface. It may be possible to use SAR to map patterns of ionospheric irregularities and/or boundary layer turbulence.

4.5.4 Multi-frequency, Polarimetric SAR

Referring back to the example of sea ice classification we ask what the increase in computation load would be to do the classification processing. In a simple algorithm one would use the M multiple data channels for a given pixel to classify it, for example the classification might be a weighted sum of the data from all the M channels with a computation load of size $F \times M \times N^2$ where F is a factor dependent on the algorithm and N is the number of pixels along one side of a square image. Thus, the computation load would increase linearly with the number of data channels for each pixel and the area of the image. Comparing with the imaging computation loads, discussed in Section 2 above, we find that classification algorithms would typically require as much processing as the original image and probably more for advanced algorithms, e.g. texture analysis requires convolution of data with a series of masks.

Classification is often followed by segmentation in which data from other than the pixel under consideration is used. Segmentation is the process of delineating regions (segments) with uniform properties. Thus, a pixel with different properties than all its neighbors might be changed to agree with its neighbors on the assumption that noise has caused the disagreement. Segmentation algorithms have potentially heavy computing requirements as

well since a fraction m^2 of the whole image would be used in segmenting a given pixel. Typically $m << 1$, say of order 0.01 or less.

The processing load is of the order $F \times M \times N^2$ for single pixel classification and up to $F \times M \times (mN)^2 \times N^2$ if classification and/or segmentation uses a fraction m^2 of the whole image as near neighbors for each pixel during classification and or segmentation. These heavy computation requirements mean that only a few images are classified and segmented as in Figure 4 - 7. So we conclude that massively parallel processing makes possible the exploitation of high-data-dimension radars, such as the example of Figure 4 - 7.

4.6 Imaging of Underground Phenomena by SAR

While SAR is generally thought of as observing the surface of the Earth, underground phenomena can be observed in two ways. First, in very dry regions low frequency SAR's can indeed penetrate into subsurface layers of the Earth. Second, underground processes such as earthquakes can have surface signatures that are observable by SAR. Below we give two examples of these methods of probing underground phenomena using SAR.

Water has a very high dielectric constant at microwave frequencies and thus vegetation and soil, etc. usually reflect radar waves well, allowing little penetration. However, in very dry regions, e.g. deserts, the relatively low dielectric constant of very dry sand (≈ 2.5) allows significant penetration — $\approx$ a few meters at low microwave frequencies, ≈ 1 GHz. At VHF frequencies, greater penetration is possible.

An interesting example of actual underground penetration is given by Elachi et al. (1984) [29]. The Shuttle Imaging Radar - A (SIR-A) observed the Libyan Desert region in southwestern Egypt. There is no vegetation in this region since the climate is extremely dry. There is a sand layer, perhaps 2 m thick, that covers bedrock. The relative dielectric constant of this layer is ≈ 2.5 and absorption is relatively low. At the bottom of this layer is a layer of bedrock with a relative dielectric constant of about 8. Hence, the backscatter echo as observed by the SAR comes primarily from the bedrock surface, some 2 meters below the surface sands. This bedrock layer is marked by many ancient drainage channels that are not evident in photography of the area. Figure 4-8 shows an example of such drainage channels.

A wonderful example of the second method is given by Massonnet et al., (1993) [52]. Using two complex SAR images collected from very nearly the same orbital path, but 105 days apart, a phase difference map was produced as shown in Figure 4-9(a). Corrections were made to take out the effect of the slightly different orbits. So phase changes should correspond to components of changes in Earth surface elevation along the radar ray path. Within this 105 day period the magnitude–7.3 Landers earthquake took place on 28 June 1992, northeast of Los Angeles. Surface displacements of as much as 3 meters were observed on the ground. The phase difference map shows movement of the surface along the radar ray path that is 23° off vertical (incidence angle = 23°). Each cycle of phase change (black to white and back again) is equivalent to 28 mm of movement along the radar ray path. The shape of the fringe pattern is very close to that expected for this earthquake as shown in Figure 4-9(b). This synthetic fringe map was generated by using an elastic

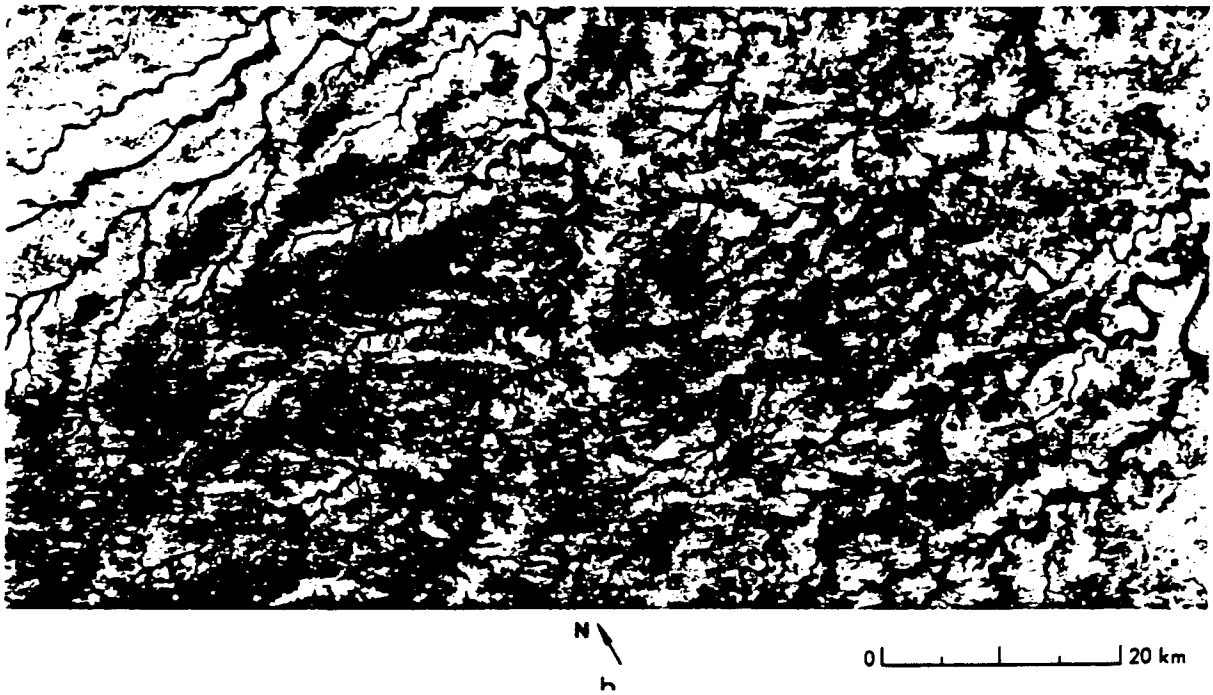

Figure 4-8. SAR image of desert region in southwestern Egypt. The drainage channels shown are not on the surface, but at a depth of about 2 meters below a dry sand surface layer. After Elachi et al. (1984).

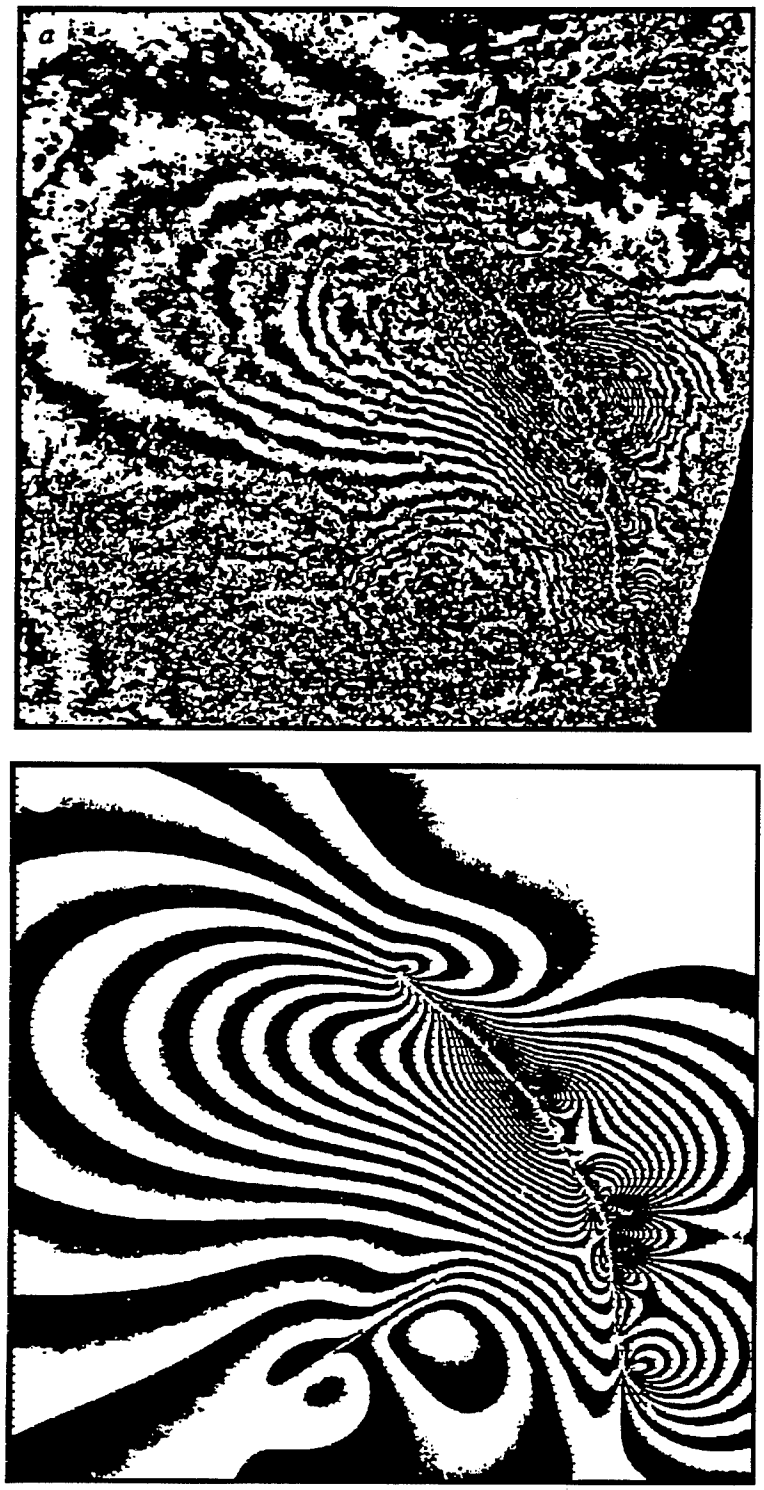

Figure 4-9. (a) the phase difference map compiled from two SAR observations, 105 days aparts with the Landers earthquake in between. Each cycle of phase (black to white to black) is equivalent to 28mm of crustal movement along the radar ray path. (b) Synthetic phase diference map computed using an elastic half-space dislocation model for the earthquake movement. Note the very close correspondence of the observed and calculated phase diference maps. (After Massonet et al. (1993)

half-space dislocation model for the earthquake. The fault along which the earthquake took place is the curved white line where the fringes begin and end. Further details are given by Massonnet et al. (1993). [52]

We think that elevation change maps, similar to that of Figure 4-9, but on smaller scales could be used to detect surface effects from underground construction. For example, shallow tunnels cause a small subsidence of the surface over the tunnel – tunnels for subway systems would be a typical example. Another interesting change that might be detected by this method would be changes in the surface induced by changes in the water table, e.g. by drilling of wells.

4.7 SAR Detection of Vibrating Objects

This section explores the possibility that low frequency vibrations of objects might be detectable using special processing of SAR signals. The effect to be explored is the change in phase path from the SAR to the vibrating object as a consequence of the mechanical oscillation of the radar reflecting surface. It will be shown that rather small amplitudes of vibration can be detected and exploited to determine the frequency of oscillation of the object under consideration. With such information, and the size of the object determined from the SAR image, it should be possible to determine the total acoustic power radiated from the object.

We begin the analysis by considering the slow-time signal returned from a target of reflectivity, F(R,x,t). As indicated in several previous sections

(e.g., Section 2.1), the received SAR signal after fast time signal processing and Fourier inversion is

$$S = \int dxdy \frac{\sigma(x,y)}{4R^2} e^{-2ikR(t)} \tag{4-37}$$

where $k = 2\pi/\lambda = \omega/c$ is the radar wave number, $\sigma(x,y)$ is the cross section of the vibrating target, and the SAR is assumed to be moving in the x-direction with a speed V. The range to the target, R(t), is normally expressed for a stationary target as:

$$R(t) = ((x_0 - Vt)^2 + y_0^2 + z_0^2)^{1/2} \tag{4-38}$$

using the coordinates shown in Figure 4-10. Note that at time t=0, the target point is located at $x=x_0$. If the target is vibrating, we must add a correction to the radar range. For purposes of illustration, let us suppose that the target is vibrating sinusoidally with a frequency ω with amplitude components (a_x, a_y, a_z). We will take the z-component of displacement to be given by a $\cos \Omega t$ so that the range to the target becomes

$$R(t) = ((x_0 - Vt - a_x \cos \Omega t))^2 + (y_0 - a_y \cos \Omega t)^2 + (z_0 - a_z \cos \Omega t)^2)^{1/2} \tag{4-39}$$

$R(t)$ for the target point can now be linearized to obtain the exponential term describing the phase of the received SAR signal:

$$R(t) \approx R_0 - \frac{x_0 VT}{R_0} + \frac{V^2 t^2}{2R_0} - A \cos \Omega t \tag{4-40}$$

where

$$A = (a_x\, x_0 + a_y y_0 + a_z\, z_0)/R_o \tag{4-41}$$

$$R_0{}^2 = R_x{}^2 + R_y{}^2 + R_z{}^2 \tag{4-42}$$

and we assume that A << x_o and x_o << R_o.

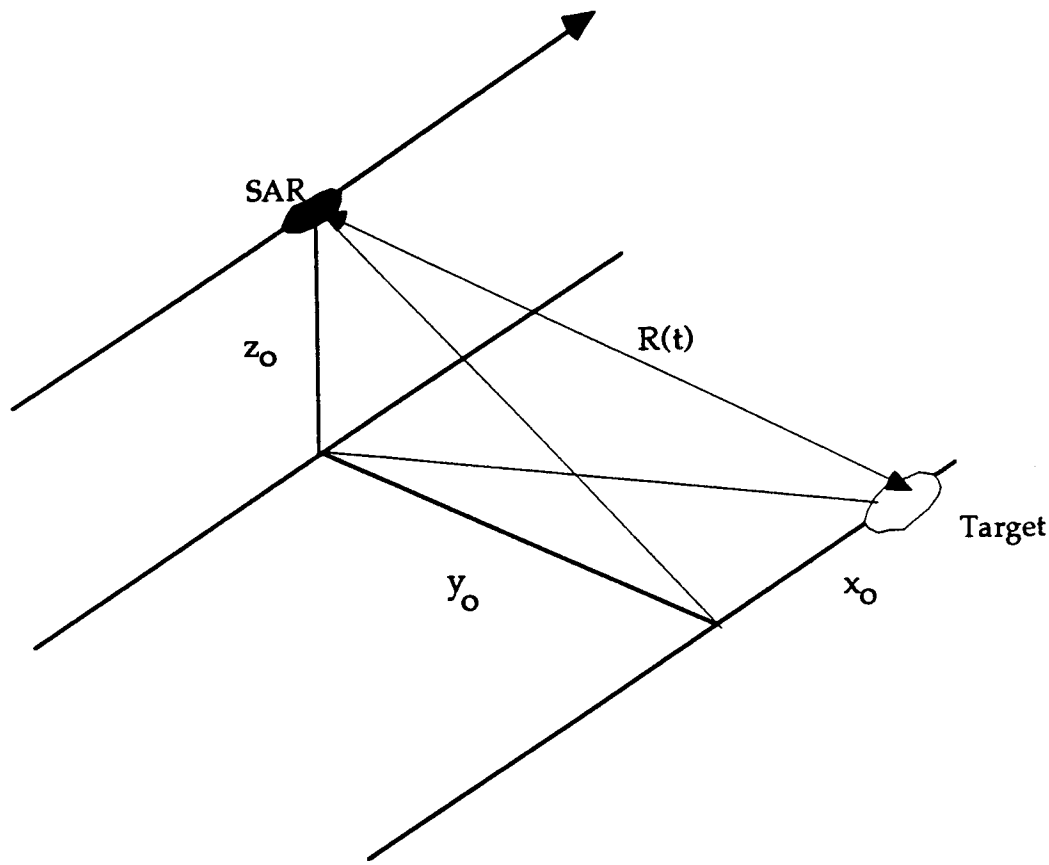

Figure 4-10. Geometry of SAR Observations.

Substitution of Equation (4-40) for $R(t)$ into Equation (4-37) gives the result

$$S = \int dxdy \frac{\sigma(x,y)}{4R^2} e^{-2ik\left(R_0 - \frac{x_0 Vt}{R_0} + \frac{V^2 t^2}{2R_0} - A\cos\Omega t\right)}. \tag{4-43}$$

The exponential in this expression can be split into two portions: the usual stationary target expression and that due to the added effect of the vibration. This gives

$$S = e^{-2ikR_0} \int dxdy \frac{\sigma(x,y)}{4R^2} e^{-2ik\left(-\frac{x_0 Vt}{R_0} + \frac{V^2 t^2}{2R_0}\right)} e^{2ikA\cos\Omega t}. \tag{4-44}$$

The last term in the integrand of Equation (4-43) can be re-expressed in terms of a Bessel series expansion:

$$e^{2ikA\cos\Omega t} = \sum_{N=-\infty}^{N=+\infty} (i)^N J_N(2kA) e^{iN\Omega t} \tag{4-45}$$

where N is an integer. Using Equation (4-44), we can write the result as

$$S = e^{-2ikR_0} \int dxdy \frac{\sigma(x,y)}{4R^2} e^{-2ik\left(-\frac{x_0 Vt}{R_0} + \frac{V^2 t^2}{2R_0}\right)} \sum_{N=-\infty}^{N=+\infty} (i)^N J_N(2kA) e^{iN\Omega t}. \tag{4-46}$$

This result provides insight to the effect of the vibrating object. Often, the dominant contribution will be that corresponding to zero frequency shift ($N = 0$). The zeroth order Bessel function $J_0(2kA)$ introduces no extra phase shift relative to that produced by the moving SAR radar illuminating a non-vibrating target. However, higher order Bessel function contributions to the received signal will come at the multiples NΩ relative to the instantaneous SAR frequency ω.

The magnitude of these contributions will depend upon the dimensionless ratio $2kA$ which is the argument of the Bessel functions in the infinite series. Examination of this term for typical values of the wavelength of the SAR and

Table 4.3 Values for Argument of Bessel Function*

λ (cm)	a = 0.1 mm	a=1 mm	a=10 mm
1	$6.28\text{x}10^{-2}$	$6.28\text{x}10^{-1}$	6.28
3	$2.09\text{x}10^{-2}$	$2.09\text{x}10^{-1}$	2.09
5	$1.26\text{x}10^{-2}$	$1.26\text{x}10^{-1}$	1.26
10	$6.28\text{x}10^{-3}$	$6.28\text{x}10^{-2}$	$6.28\text{x}10^{-1}$

* z_0/Ro=0.5*

the amplitude of typical vibrations and radar wavelengths shows that there are no simple approximations to $J_N(2kA)$ for large or small arguments. This is illustrated in Table 4.3.

Generally speaking, the amplitude effect of the vibrating surface will be introduced both through the magnitude of each Bessel function term, $J_N(2kA)$, and the phase. However, the term $J_0(2kA)$ has no phase shift and contributes substantially to the radar return, except near zeros. The higher order terms have both an amplitude impact and phase effects. Examination of the arguments of the exponentials of Equation (4-44) shows that the phase due to the various terms can be written as

$$\phi = \left(\frac{2kV}{R_0}\right)[x_0 \pm \frac{N\Omega R_0}{2kV} - Vt\ /\ 2]t. \tag{4-47}$$

When one considers that target location is often done via phase methods, it is apparent that contributions to the signal will appear in positions which are shifted by a distance

$$\Delta x = \pm\frac{N\Omega R_0}{2kV}. \tag{4-48}$$

The result is that radar energy reflected by the vibrating target is Doppler shifted, giving rise to a decrease in total reflected energy attributed to the

target identified by σ(x,y) (a "shadow" effect) and the addition of radar energy to enhance the apparent cross sections of targets at $\sigma(x \pm \frac{N\Omega R_0}{2kV}, y)$.

As an example consider a satellite SAR such as ERS-1. Magnitudes for Δx are given in Table 4.4, shown below for $N = 1$ to 4 at various low frequencies of vibration. The above results show that the phase shifts

Table 4.4 Values Δx

N	Ω = 60 Hz	Ω = 600 Hz	Ω = 6000 Hz
1	187 m	1.87 km	8.750 km
2	374 m	3.74 km	37.4 km
3	560 m	5.60 km	56.0 km
4	748 m	7.48 km	74.8 km

R_0 = 780 km V = 7.7 km/sec λ = 6 cm

introduced by the vibrations of the target are substantial, they are located symmetically with respect to the SAR received Doppler shifted signal, and the amplitude of the target has the possibility of being significantly distorted from that expected for a stationary surface.

For the present purposes, it is important to note that not only will substantial energy will be shifted away from the "core" of the target into symmetrical "wings", but that there is a coherency between the wings themselves, set by the vibration frequency. Thus, a vibrating target is surrounded by a symmetrical pattern of phase coherent "wings" extending to either side of the target frequency. If the target has several principal modes of vibration, these added wings will also be present in the radar signal with different phase coherence.

Detection of a vibrating target can be implemented in digital form by

correlation methods. Figure 4-11 illustrates the technique in frequency coordinates. Since it is known that there will be equal contributions above and below the SAR Doppler-received frequency corresponding to the location of the target, one can imagine that a digital filter method could be developed to obtain measures of symmetrical frequency shift on either side of the Doppler shifted signal. While a few eigenmodes of vibration would likely be present, coherent processing of the entire signal would be needed to find the full spectrum of vibrations.

Some caution must be taken with this method, however. As shown in Figure 4-11, it is possible that the Doppler shifted signal components may extend beyond the bandpass of the radar receiver, i.e., the Doppler shifted signal may be placed outside of the ground area of the SAR image. This may place an upper limit on the detectable frequencies of vibration for particular SAR systems.

It is clear that much calculation will be needed to detect and to extract information about vibrating objects that appear in SAR images. However, massively parallel computers are ideally suited to this task. The main computation is a convolutional filter, easily implemented with the FFT methods discussed in Section 2.

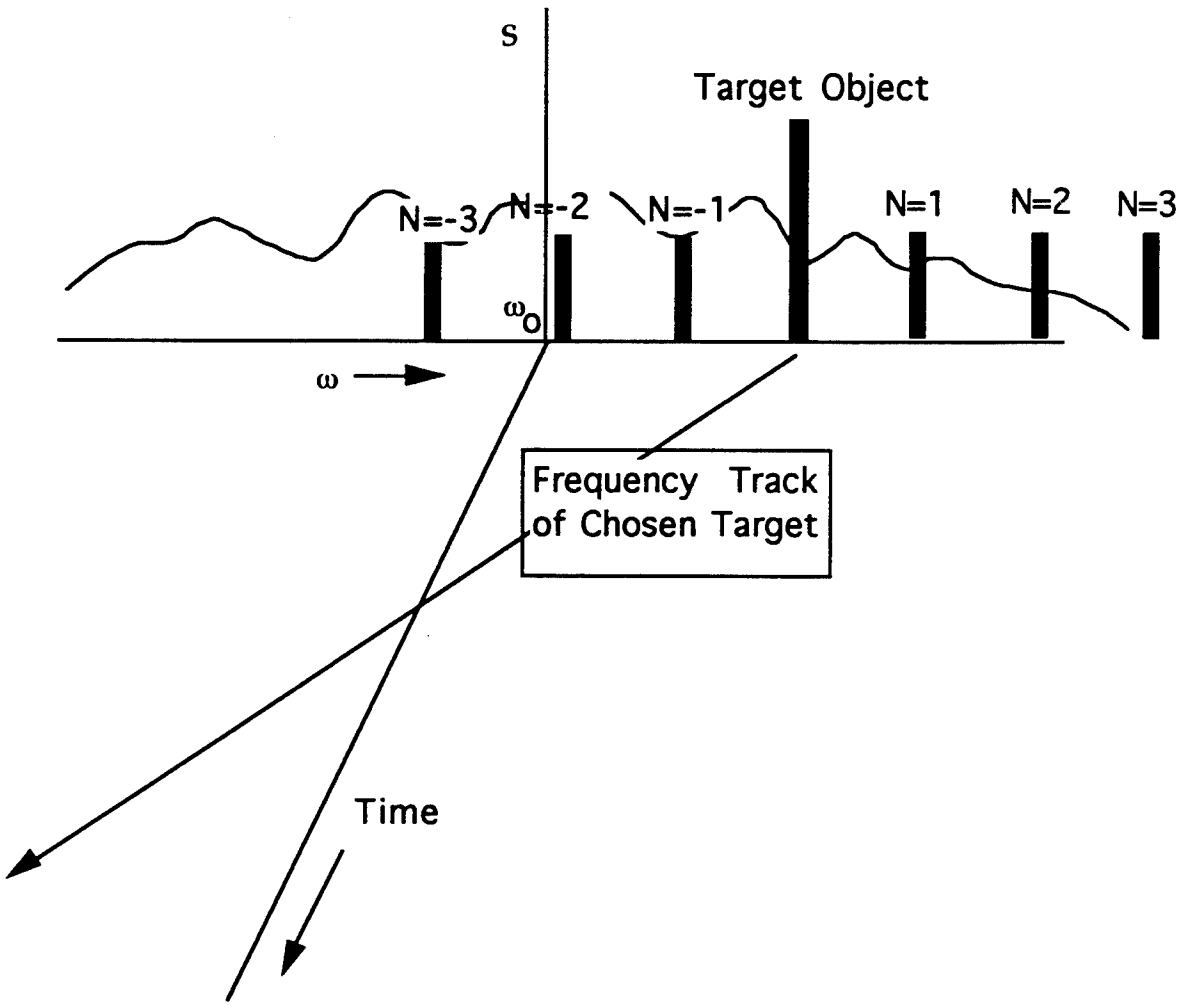

Figure 4-11. Doppler shifted signal components.

5 SAR COUNTERMEASURES

In another 1993 JASON study on Automatic Target Recognition (ATR) we considered a range of countermeasures against SAR (and other sensor) detection and characterization. For the convenience of the reader, we repeat here the relevant material on SAR CCD (camouflage, concealment, and deception. SAR presents a very special set of CCD vulnerabilities, a number of which can be overcome by using one or more extra sensors along with the SAR.

5.1 Concealment and Nets

Concealment from an X-band SAR under a canopy of foliage is relatively easy to do, but is substantially more difficult against an L-band radar. Lincoln Labs, JPL, and others have successfully demonstrated foliage penetration with 3-frequency SARS (for example, L-, C-, and X-band), but with conventional technology these are cumbersome, requiring separate feeds or antennas for each frequency.

Purely absorptive radar nets are available, but these are not necessarily the most effective, since the radar nets are designed for homogeneous absorption. Better would be inhomogeneously patterned nets (but without points and edges giving glints), somewhat along the line of conventional camouflage patterning, but we are not aware that any have ever been tried.

Since SARs can be operated fully polarimetrically, care must be given to matching the response of concealment measures to polarimetric detection. Lincoln Labs has demonstrated that terrain responds rather differently from man-made objects in general.

It is, of course, possible to reduce the radar cross-section of an object very considerably over a range of aspect angles by providing a radar-opaque cover composed of a few simple planes set at various angles. However, edges and corners will still show up, and at some angles enormous glints will appear.

5.2 Signature Diversity and Anti-Simulation

This is an especially fertile field for use against SARs, because SAR cross-sections of a single object vary enormously with aspect angle. This variability comes from the presence of many bright points on man-made objects, which contribute to a target signature with a large number of speckle points and from variable multi-bounce geometries depending on the local target environment. Lincoln Lab studies [30] show that the speckle pattern of vehicles tends to decorrelate over an aspect angle difference of a few degrees. Signature diversity is easily produced by the more-or-less random addition of bright glint points to a target, and by concealment of ones that are already present (e.g., by removing a bracket).

Unless the added bright features are on outriggers, to make smaller targets appear to be bigger ones, addition or subtraction of glint points will not change the overall apparent size of targets. However, it is a peculiarity of SAR

that moving glint points on a target can make it appear to be larger than it really is, at least in the azimuth direction of the SAR. The reason is that these moving glint points, if they have a velocity component along the range axis, give rise to a Doppler shift which is interpreted as an azimuth displacement by the SAR algorithm. In formulas, the standard formula relating Doppler frequency f_D to azimuth displacement x is

$$f_D = \frac{2Vx}{\lambda R}$$

where V is the SAR velocity, λ the wavelength, and R the range. Thus any source of Doppler yields an x-displacement:

$$\Delta x = \frac{\lambda R}{2V} \Delta\ f_D. \tag{5-2}$$

For target motion along R with velocity U_R,

$$\Delta f_D = \frac{2U_R}{c}\ f_c \tag{5-3}$$

where f_c is the SAR center frequency; then

$$\Delta x = \frac{RU_R}{V}. \tag{5-4}$$

A space or air-based SAR typically has $R/V \sim 100$ s (e.g., $R = 10^3$ km, V=7 km/s) so $U_R = 1$ cm/s produces Δ x= 1 m.

The velocity U_R is necessarily periodic, if the moving point is to stay attached to the target. If it is desired to produce a false image only on one side of the target, one can provide the SAR with a velocity of only one sign, by making the moving target object bright on one side and dark on the other, and moving it along a straight line and turning the mover by 180° at velocity reversal, or by moving it along the circumference of a circle. As long as the

period of the motion is less than SAR integration time (a few to a few tens of seconds) no oscillation will be seen. The amplitude of the motion should not be larger than a resolution cell, or the false image will be dimmed by blurring, in proportion to the number of pixels it passes through.

False images can also be produced by a vibrating membrane. To illustrate, consider the slow-time return of a target of reflectivity $F(R, x, t)$; the received SAR signal after fast-time processing and Fourier inversion is

$$S = \int d\,x\,d\,y\,F\,e^{2i\omega R/c} \tag{5-5}$$

where the range variable R is expressed in terms of ground-plane variable x,y (x is the azimuth variable) and height z:

$$R = \left((x - Vt)^2 + y^2 + z^2\right)^{1/2} \tag{5-6}$$

and V is the SAR velocity. Now suppose that

$$z = z_o + \mathrm{a}\ \cos\Omega t; \tag{5-7}$$

then

$$\frac{2\omega R}{c} \simeq \frac{2\omega R_o}{c} - \frac{2\omega V x t}{R_o c} + 2\frac{z_o k a}{R_o}\cos\Omega t \tag{5-8}$$

with $k = \omega/c$ as the SAR wave number, and irrelevant terms in the expansion have been dropped. Then Equation (5-5) becomes, after dropping irrelevant phases,

$$S = \Sigma_N \int d\,x\,d\,y\,i^N\,J_N(\epsilon)\exp\left(\frac{2i\omega V X}{t}R_o c - iN\Omega t\right)\,F \tag{5-9}$$

where J_N is a Bessel function and $\epsilon = \frac{2z_o k a}{R_o}$. One sees that the Nth term of Equation (5-9) is equivalent to a target displaced in x by Δx:

$$\Delta x = \pm\frac{N\Omega R_o}{2kV}. \tag{5-10}$$

Putting in numbers, with $R_o = 10^3$ km, $V = 7$ km/sec, $\lambda = 2\pi/\mathrm{k} = 3$ cm, we find

$$\Delta x \text{ [m]} \simeq 30\, N\, \Omega \text{ [rad/sec]}. \tag{5-11}$$

Of course, the strength of the Nth term is $J_N(\epsilon) \sim \epsilon^N$ if $\epsilon << 1$; usually, one will want only the $N = 1$ term to be important. Note that the vibrating membranes necessarily yields symmetrically displaced false images at $\pm\Delta x$.

W. A. Nierenberg has pointed out that such moving parts to fool radars are quite well-known; metallized pinwheels have been used by motorists to confuse police speed radars.

5.3 Decoys and Jamming

Decoys. Conventional vehicle decoys, available on the world market, strive for visual deception and are lightweight, made of wood or fiberglass. As such they are not good radar decoys, but addition of a lightweight metallized skin and metal attachments to serve as glint points is feasible. As already mentioned in connection with signature diversity and antisimulation, one need not make all decoys look alike and strive for a perfect match with a true target; it is better to present a diversity of signatures, and if desired to add glint points to targets to make them look like decoys. Note that, unless a SAR system is capable of interferometric height determination on a wholesale basis, decoys can be made flat and still be very useful.

Jamming. Jamming a SAR is not easy if careful attention is paid to guarding the details of the SAR waveforms (center frequency, chirp rate,

waveform coding, etc.); this is true even for low-powered SARs, which take advantage of the need for a long coherent integration time to get resolution by adding perhaps thousands of returns coherently over a large bandwidth (hundreds of MHz). For example, a 100W X-band UAV SAR at 30 km from a 1 m^2 target of backscatter coefficient 0.01 may produce an average return of only 10^{-8}W from that target, but by integrating over 3×10^4 pulses with a time-bandwidth product of 10^4, the effective target power is 3 W. That is, a broadband white-noise jammer has to be much more powerful than 3 W to jam even a single pixel, and there are millions of pixels to be jammed. Jamming could be much more effective if it were matched to the chirp pulse, but this can be denied—even with full knowledge of the SAR characteristics–by using coded waveforms for the chirp pulses. For example, Costas codes (as discussed elsewhere in this report) with hundreds of different orthogonal forms are available.

6 SAR OF THE FUTURE

In principal, SAR techniques rely only on high-total-bandwidth transmissions to achieve range resolution and a time-varying transmitter-target-receiver path to achieve resolution in a second dimension. In practice, implementation has concentrated on simple time waveforms and collocated transmitters and receivers. Future SARs can exploit different waveforms and geometries to realize new opportunities for radar imaging.

This section introduces some representative opportunities in waveforms and in configurations with separated transmitters and receivers. In discussing such opportunities, it is assumed that the new computational capapabilities discussed in Section 3 are available.

6.1 SAR Waveforms: Introduction

In its decade of development, SAR has moved from being a mere theoretical concept to being practically its own engineering discipline. It is natural, in such a history, that engineering choices, made at a certain stage of technological development, become sanctified as design principles, and that, possibly, very different ways of doing SAR remain unexplored.

One possible such area is that of SAR waveforms. Modern SARs virtually always have a repetitive waveform, with an identifiable pulse repetition frequency (PRF) chosen, among other factors, to avoid range ambiguity over

a desired range region. Likewise, the waveforms for each pulse are very often variants on frequency swept, linear-in-time FM ramps. This is because such waveforms map the SAR inversion problem neatly into 2-dimensional FFTs. As will be shown below, however, the linear FM chirp waveform has poor correlation properties. We can do much better with other waveforms with some increase in processing complexity.

For some comtemplated systems, constraints on the acceptable PRF become important design limitations, one of the long poles in the tent. Also, one can think of applications where waveforms as regular as FM ramps are undesirable, either because of cross-talk between multiple systems in-band, a desire for reduced (or less specific) signatures, or for other reasons. As a result, we will examine several possibilities for SAR waveforms.

6.1.1 Stochastic SAR Waveforms

In this section we want to outline a very different way of possibly doing SAR. The proposed method, which we call "stochastic SAR" has no PRF. The transmitted waveform consists of continuously transmitted (in-band) white noise, so peak and average power are identical, and the waveform reveals nothing about intended capabilities. Within limits, multiple overlapping SARs can operate in the same band.

The required property of the continuous, random (or psuedo-randon) transmitted signal is that it have a 'noise-like' auto-correlation function. For example, let $T(t)$ be the transmitted complex phasor of the SAR at time t,

that is, the transmitted complex amplitude "unwound" by the band center frequency. To keep the transmitted power as nearly constant as possible (this is not required, but rather only illustrative), we might have

$$T(t) = T_0 \exp[i\ z(t)] \tag{6-1}$$

where $z(t)$ is a band-limited randomly varying phase. That is, the two-point autocorrelation function for T,

$$\langle T(t)T(t+r)\rangle \tag{6-2}$$

should be T_0^2 at $t = 0$ and decrease smoothly and rapidly to zero for τ greater than some $\tau*$, the characteristic correlation time (whose inverse approximates the channel bandwidth).

We can now employ the theoretical equations and processing techniques of Chapter 2 (see Section 2.1, etc). We have not worked this technique out in all detail, so it should be considered only "the idea for the idea" or (as we intend) more of an existence proof that there may be very non-traditional way of accomplishing SAR design goals. Note that transmitter tubes need not be particularly stable in phase and amplitude, provided one can accurately measure the complex amplitude of what is transmitted.

6.1.2 Deterministic Coding

The high-power R.F. sources used in a space illuminator can handle amplitude, phase, or frequency modulation to obtain wide-bandwidth waveforms. Wide bandwidth and long duration signals are required for range

and Doppler resolution. Performance of such signals can be judged by the ambiguity function of the waveform. The ambiguity function is defined as the absolute value of the envelope of the output of a matched filter when the input to the filter is a Doppler-shifted version of the original signal to which the filter was matched. The filter is matched to a signal at the nominal center frequency and at a nominal time delay. The two parameters of the ambiguity function are time delay τ and frequency shift ν. Ideally, one would like the output signal to peak at $\tau = 0, \nu = 0$ and to be zero everywhere else. An exact realization of this "thumbtack" ambiguity function is not possible, but approximations are available. The 'stochastic' waveform of the previous section is one example. Another such approximation, the Costas array waveform, will be discussed below. Some form of large time–bandwidth product is needed to provide system sensitivity through increased energy per radiated signal.

Waveforms which have proven useful in radar include linear FM chirps, pseudo random bi-phase coded signals, linear and nonlinear chirps, and frequency hop coded signals. Bi-phase coded waveforms do not have good ambiguity functions unless the codes can be run continuously without providing dead space for receiving. Linear and nonlinear chirp waveforms can provide good time (range) sidelobes but particularly for linear chirps result in relatively poor frequency discrimination. The Costas waveform can overcome these difficulties. Consider a step chirp waveform signal as shown in Figure 6-1a. The horizontal axis, representing time, is divided into N contiguous sections of length T and the vertical axis represents frequency. Each row represents a discrete frequency. The N frequencies are equally spaced. Note

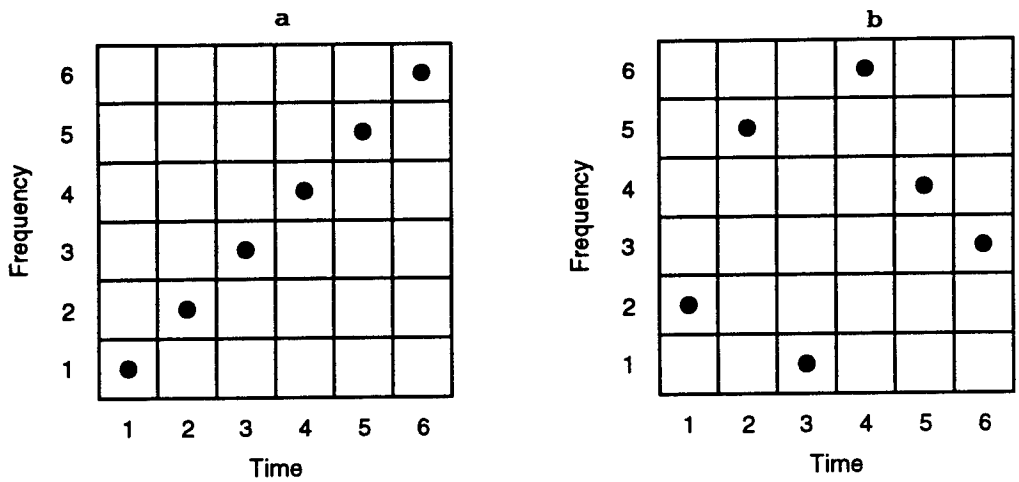

Figure 6-1. Binary matrix representation of (a) quantized linear FM and (b) Costas.

that the quantized linear FM signal belongs to a family in which there is only one transmission per column and per row. This means that at any given time slot only one frequency is transmitted, and each frequency is transmitted only once. There are other possible frequency hopping sequences that belong to this family. The hopping order strongly effects the ambiguity function of these signals. If a thumbtack shape is considered ideal, then the staircase sequence resembling the continuous FM is the worst possible choice.

John Costas suggested a new criterion for selection of hopping sequences that yields ambiguity functions that approach the ideal thumbtack. Frequency hopping signals allow a simple procedure that results in a rough approximation of their ambiguity function. This is possible because the cross correlation between signals at different frequencies approaches zero when the frequency difference is large relative to the inverse of the signal function. The ambiguity function, at any given coordinates, is an integral of the product between the original signal and a replica of it, shifted in time and frequency according to the delay and Doppler coordinates of the function. Thus a good idea of the shape of the ambiguity function can be obtained from overlaying a binary matrix representing the signal upon itself and shifting one relative to the other according to the delay and the Doppler. At each combination of the shifts, the number of coincidences between points of the fixed and the shifted matrix represent the relative height of the ambiguity function. If we perform such an exercise on the signal represented by the matrix in Figure 6-1b, we find that except for the zero shift case, when the number of coincidences is N, we cannot find any combination of shifts that will yield more than one coincidence. This is the criterion for Costas sequences; namely,

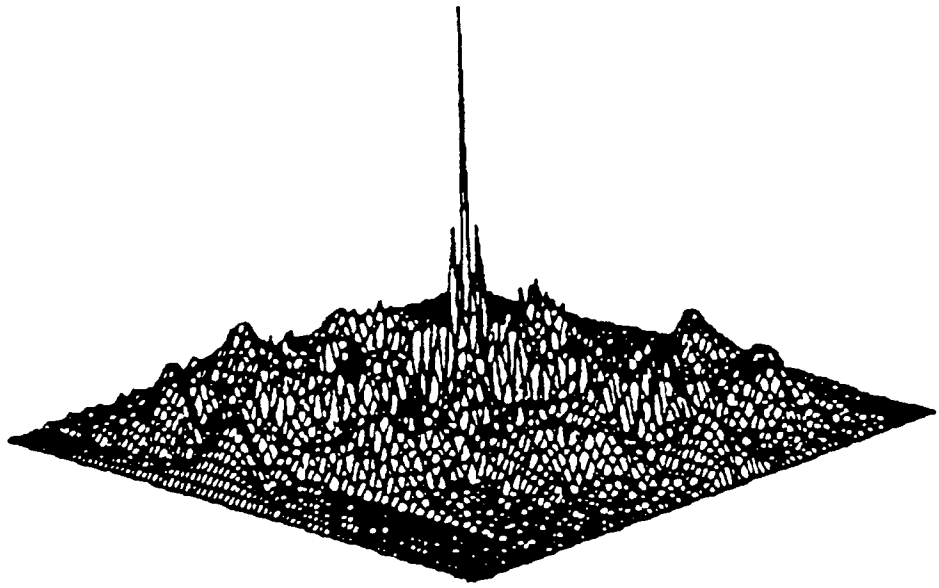

(a)

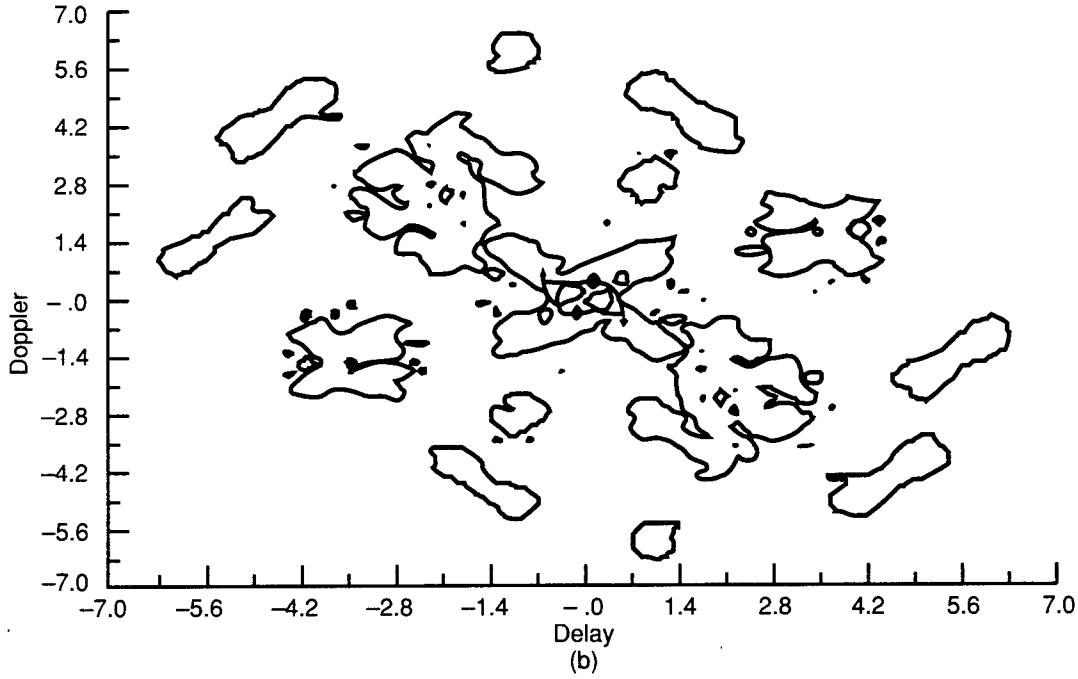

(b)

Figure 6-2. The ambiguity function of a length-7 Costas signal (coding sequence 4, 7, 1, 6, 5, 2, 3). (a) 3-D view. (b) Contour plot.

those sequences of frequency hopping that will yield no more than one coincidence. The ratio between the main lobe and the pedestal is approximately N. However, the pedestal is not smooth; it has a few peaks higher than $1/N$ and many deeps in other locations within the pedestal. In order to lower the pedestal, it is necessary to increase N, the number of frequencies used. This will shift the volume away from the vicinity of the main lobe by lowering and widening the pedestal.

Families of frequency hop codes with a small number of coincidences in their auto and cross–ambiguity functions have been of interest to the designers of multi–user radar and sonar systems, as well as multiple–access spread–spectrum communications systems. Costas array achieve nearly ideal auto–ambiguity functions, but one has difficulty finding a family of such codes with good cross–ambiguity functions. Recently Maric and Titlebaum have found an interesting family of codes based on number theoretic concept of cubic congruences. They show that for about 50 percent of the prime numbers, families of full codes exist which have at most, two coincidences for any time–frequency shift in their auto–ambiguity functions. They define a cubic frequency hop code for a finite field J(p) by the placement operator; $y(k) = ak^3$ (mod p). An example of two cubic codes for $p = 11$ is shown in Figure 6-3. Prime less than 500 of the form $p = 3n + 2$ are shown in Figure 6-4 [31]. (Note error for prime 37.) For one prime, the code performance is true for a whole class of cubic codes (a class consists of $p - 1$ codes). Extremely easy construction makes these attractive for use in radar systems with frequency hop coding.

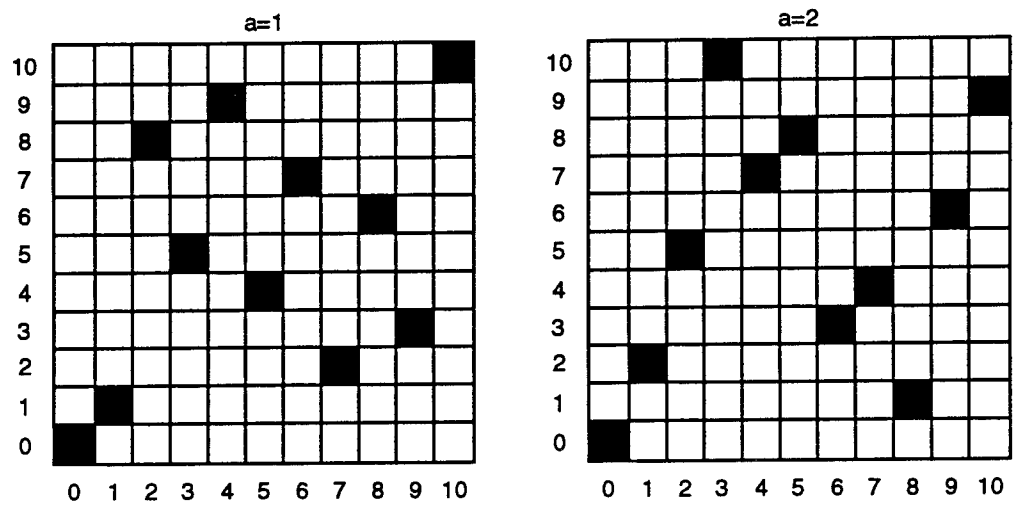

Figure 6-3. Example of two cubic codes for $p = 11$.

5	71	173	269	401
11	83	179	281	419
17	89	191	293	431
23	101	197	311	443
29	107	227	317	449
37	113	233	347	461
41	131	239	353	467
47	137	251	359	491
53	149	257	383	
59	167	263	389	

Figure 6-4. Primes less than 500, of the form $p = 3m + 2$. This table has an error in that 37 is prime, but not of the form $p = 3m + 2$, and should not be on the list.

Costas/Maric Coded Waveforms Applied to SAR

The process for generating a synthetic range profile using coded pulses can be summarized as follows:

1. Transmit a series of bursts of narrowband pulses, where each burst consists of n pulses stepped in frequency by a Costas/Maric time frequency code.

2. Set a range–delayed sampling gate to collect I & Q samples of the targets base band echo response.

3. Store the quadrature components of each of the n echo signals from each transmitted burst. Each stored echo burst of data approaches the equivalent of the instantaneous discrete spectral signature of the target if burst times are short relative to target aspect change.

4. Compute an inverse discrete Fourier transform (IDFT) of the resulting set of n complex frequency components of each echo burst to obtain one or more n-element synthetic burst. Repeat the process for N bursts to obtain N slant range profiles.

The coded stepped–frequency waveform removes the requirement for both wide instantaneous bandwidth and high sampling and analog to digital (A/D) rates.

Slant range resolution with coded step–frequency waveforms in place of chirp waveforms is obtained synthetically using an IDFT process. Cross–range resolution can be obtained as in chirp pulse compression radars by coherently integrating range-resolved echo signals obtained during the real beam dwell time. Transmission of coherently related pulse–to–pulse frequency–stepped waveforms in a series of bursts, with n pulses per burst, produces sets of n echo signals, which are the frequency–domain measurements of reflectivity data from each burst. The n complex values per burst, sampled at a given viewing angle in each coarse range–cell position, are transformed by using the IDFT to yield the n-element synthetic range profile in that course range cell.

2 Meter Range Resolution (along the earth) Using Costas/Maric Code

The following parameters are an example of a Costas/Maric code for a low-earth-orbit satellite SAR with 1.4 m $\times$ 4.7m resolution and a swath of 134 km. Each burst uses a different Costas-code so that returns from different bursts are not confused.

For a depression angle of 45 degrees, resolution of 2 m along the earth requires slant-range resolution of $\Delta r_s = 2/1.414 = 1.414$ m.

$n = 59$ code length (Figure 6-5)

$\Delta f =$ Frequency Step

$T_1 = 1/(\Delta f) =$ Chip duration

$n(\Delta f) = c/(2\Delta r_s) = 106$ MHz Total bandwidth of waveform

$nT_1 = n^2/(n\Delta f)$ Code duration (burst duration) $= 32.45\ \mu$ sec

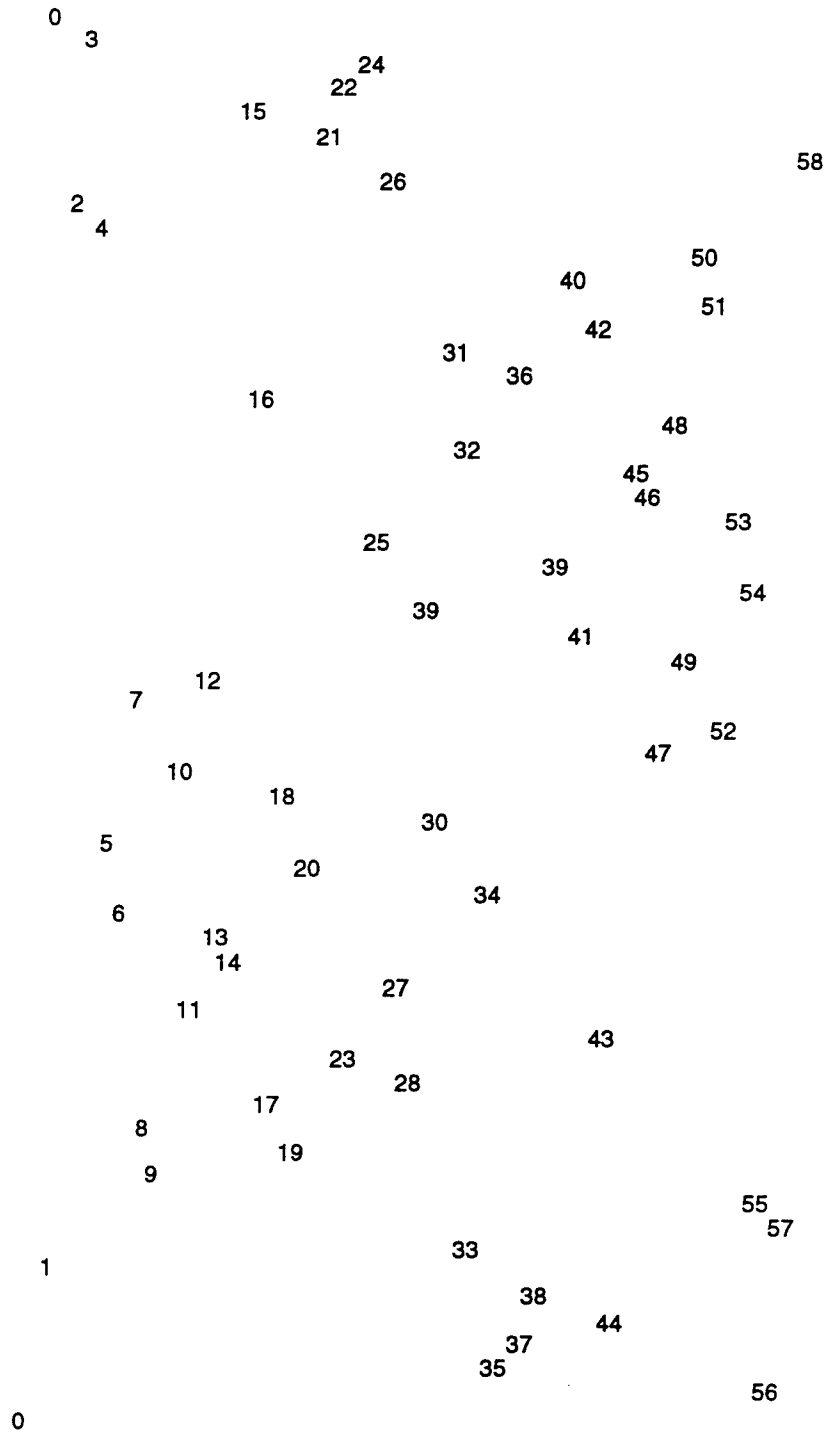

Figure 6-5a. Example 1 of a Maric/Costas code of length 59.

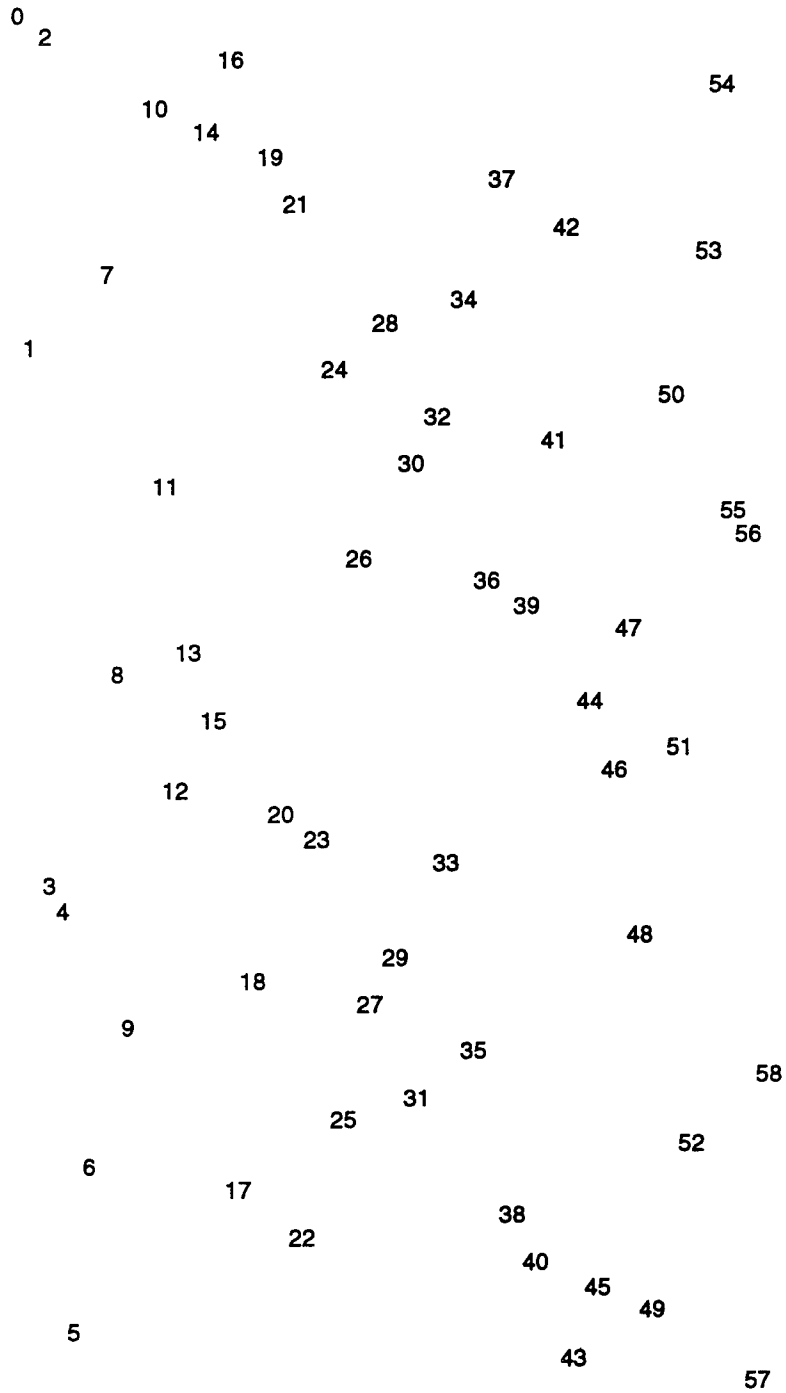

Figure 6-5b. Example 2 of a Maric/Costas code of length 59.

Assume PRF $\approx$ 1500 bursts per second

then PRI $\approx$ 1/1500 = 666.67 μsec pulse repetition interval

and time interval for receiving echoes = 666.67-32.45 = 634.22 μs

range interval for receiving = 666.7(150)=95 km

ground interval for receiving = 95(1.414)= 134 km

unambiguous PRF = 2 $v_{p/L}$ = 1500 per sec

v_p = 7 km/s orbital velocity

L = 2 v_p/1500 = 9.3 m radar real aperture

Along track resolution = L/2 - 4.7 m

Shown in Figure 6-5 are two examples of length n=59 Maric/Costas codes.

Pulse-Code Modulation by Cyclic Difference Sets

The stochastic SAR approach discussed earlier in this section suggests a somewhat different implementation approach in which the stochastic waveform is replaced by a deterministic waveform having pseudo-random properties. A specific type of easily-generated pseudo-random array is described below.

Terminology

A (v, k, λ) cyclic difference set has v elements, k of which have value +1 and $v - k$ have value -1. If $D = d_1 \ldots d_k$ is the collection of elements with value +1, then the congruence, $d_i - d_j = \propto \pmod{v}$ has exactly λ solution pairs. Generation rules for many (v, k, λ) sets are known with the properties: $(v, k, \lambda) = (4t-1, 2t-1, t-1)$ with t an integer, e.g., Hadamard sets. (Leonard D. Baumert, Cyclic Difference Sets, 1971).[32]

Basic Concept

There exist large classes of (v, k, λ) cyclic difference sets that are pseudo-random (i.e., half-filled $k \sim v/2$, uniform spatial frequencies, uniformly redundant). Once a pulse repetition time, T_{rep} and a frequency bandwidth, B_R, have been determined, choose a large cyclic difference set with order, $v \leq 2 \times T_{rep} \times B_R \equiv v_{band}$. Pulse-code modulate the band-limited signal with the cyclic difference set (analogous to bi-phase Barker codes, see e.g., Levanon, Radar Principles)[25]. That is, if V_j is the jth element of the (v, k, λ) set, then the modulation function is:

$$s(t) = \sum_{n=0}^{v-1} s_n(t - n\frac{T_{rep}}{v})$$

where

$$s_n(t) = \begin{array}{ll} V_n, & \text{if } 0 \leq t \leq \frac{T_{rep}}{v} \\ 0, & \text{otherwise.} \end{array} .$$

Correlation of the transmitted signal with a time-shifted template has approximately uniform cross-correlation for the zero-mean B_R limited signal. Signals would be transmitted bistatically so that problems with "gaps" are circumvented. The signal pattern could be repeated periodically and continuously with period T_{rep}. This is a pseudo-random analog to the "stochastic" approach, and is just the usual pulse-code modulation approach.

Choosing $v \leq v_{band}$ leads to signals which have frequencies that are predominantly multiples of $v/(2 \times T_{rep})$. An option is to choose v much greater than v_{band}. Modulation would then be an averaging process over several ($\sim v/v_{band}$) adjacent elements of the cyclic difference set. Specifically, the initial modulation function $s(t)$ would be the same as above, but passed

through a low-pass filter with cutoff B_R. In this case, the modulated signal can contain significantly more frequency content than for $v \leq v_{band}$, but should have similar (better?) cross-correlational properties. This possibility needs more investigation.

Numbers

For X-band (10 GHz) and pulse repetition frequencies of 1 kHz, cyclic difference sets of order $v \leq 10^6$ are needed. This should be no problem to generate off-line and require < 1 MB storage (1-bit per element). The limitations are imposed by the hardware implementation of the pulse-code modulation scheme. Note that the cross correlation of a perfect pulse-code modulation scheme has sidelobe values $\sim 1/v$, i.e.,

$$C_p = \sum_{n=0}^{v-1} V_n V_{n-p} \sim \begin{cases} v, & \text{if } p = 0 \\ 1, & \text{if } p \neq 0. \end{cases}$$

Topics for further investigation

1. The return from a given scatterer must be $\geq T_{rep}$, yet close enough to T_{rep} that pulse numbering ambiguities do not occur.

2. Which long cyclic difference sets are easiest to compute?

3. Are there pseudo-random arrays that can tolerate gaps and still maintain desired cross-correlation properties?

6.2 Geosynchroneous-Orbit Bistatic SAR

Many different types of SARs will be made feasible, or have their performance greatly enhanced, by future advances in processing. We discuss the prospects for "bistatic" SAR, focusing the discussion on last year's JASON proposal [33], [34] to study a large SAR illuminator in GEO orbit, which could serve a variety of receive-only as well as transmit-receive SARs in LEO satellites, aircraft, UAVs, and weapons platforms. We call the GEO SAR illuminator a public-service SAR, because it can serve many clients, in the intelligence, military, and scientific communities, just as GPS does (and, just as with GPS, coded waveforms help to deny SAR use to unwanted clients). Within limits, a client can tailor a receiver to his own needs for resolution, coverage, revisit time, and so forth. Many clients will find that they are able to afford SAR systems driven by the GEO illuminator, while they could not afford a stand-alone systems. Such systems can not be rigorously bistatic because a time-varying transmit-target-receive path length is necessary for SAR processing.

The following bullets describe the contents of this section:

- The JASON 1992 SAR work will be updated by consideration of slightly different SAR parameters;
- A discussion of instant interferometric SAR in which some of the low-altitude SAR receivers can transmit also, so that their receivers can acquire two phase-coherent images simultaneously or do three-dimensional terrain maps;

- An account of previous experiments [35], and future prospects [36] for bistatic SAR acquisition of aircraft targets, using a GEO illuminator and low-altitude or ground-based receivers at distances of two or even hundreds of km from the detected aircraft.

Description of 1992 Public-Service SAR work

We will be brief here; further details can be found in [34]. The basic point of a SAR illuminator in GEO is that its beam, illuminating an area of packages 100 $\times$ 100 km, is available virtually instantaneously anywhere over a substantial part of a hemisphere of the earth, and that the SAR receivers at much lower altitudes are relieved of the need to carry transmitter power and batteries. This is not an important issue for a manned aircraft, but is for satellites and high-altitude long-endurance UAVs. Both manned aircraft and UAVs might make good use of the stealth opportunities arising from operating in receive-only mode. On the other hand, an aircraft or possibly a satellite which has a SAR transmitter/receiver compatible with the GEO illuminator can receive signals from both transmitters illuminating the same scene, and do phase-coherent interferometry or (incoherent) stereo imaging with no wait to make a second pass over the scene. In either case, the motivation is to get theater-sized SAR coverage with short revisit time, because many receive-only SARs can be fielded and because of the possibility of instant interferometry. Of course, the ability to take multiple SAR images, and short revisit times, are only made worthwhile if processing latency can keep up, which is where massively-parallel processing comes in.

6.2.1 Public-Service SAR Parameters

The following three charts, Figures 6-6 through 6-8, (the first of which is taken from [33]) give possible examples of parameters for a GEO transmitter as well as lower-altitude receivers. The coherent integration time, not really a transmitter parameter, is listed on the transmitter chart to indicate the coherency requirements that the transmitter must be ready to support. A target cross-section of 0.01 m^2 is more or less appropriate to a 1 m target, but the transmitter bandwidth will support resolution of 0.3 m or better; this simply requires choosing the right receiver parameters. We are aware of, but will not detail here, the special problems of this sort of bistatic SAR: For example, the illuminated patch is much bigger than the ambiguity free range swath, suggesting the use of Costas/Maric codes (see Section 6.1.2). All such problems have solutions aided by fast processing; e.g., tagged (coded) range chips can remove ambiguities.

The GEO illuminator is power-limited, because of the expense of producing power in GEO. It is instructive to compare the GEO-illuminator average power density of $\sim 8 \times 10^{-7}$ W/m^2 with what could be produced by an aircraft or LEO satellite; to illuminate a range-unambiguous area 30×30 km at this level would require about 3 KW average prime power at 25% efficiency. This is far from a trivial power level for a LEO satellite or UAV. Saving the cost of such power on many receivers is an extremely important aspect of the Public-Service SAR.

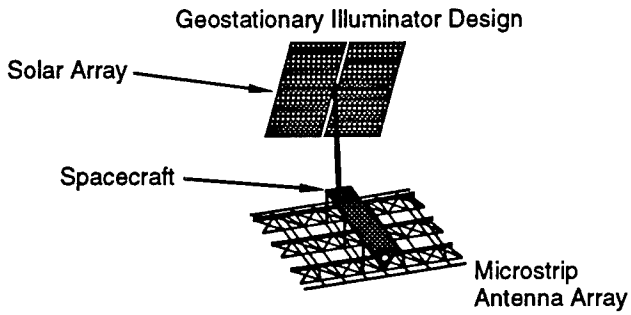

Antenna size = 5 x 5 m
Operating wavelength = 3 cm ⇒ Number of antenna elements ≈28,000

X–band module peak power = 17W
Peak power required = 80 kW ⇒ Number of transmit modules ≈5,000

Average transmitt power ≈8 kW
Transit module efficiency ≈25% ⇒ ≈32 kW DC power required
≈24 kW thermal cooling requirement

Solar array of 140 sq m would supply power using GaAs cells (in geostationary orbit solar array would seldom be in eclipse); 25 sq. m radiating at 400K would do thermal cooling to 3K space

Current state of the art: SIR–C antenna (Ball Aerospace)

Figure 6-6. GEO illuminator design concept, using a phased-array antenna. (from Callan et al. 1993)

GEO Transmitters

Peak radiated power P_T	80 kW
Average radiated power (duty cycle 0.1)	8 kW
Area of regard A	$(100 - 200\ km)^2$
Frequency	10 GHz
Bandwidth B	1 GHz
PRF	10^4 Hz
Compression ratio rc	10^4
Coherent integration time T	4 – 40 sec
Radiating aperture	25 – 100 m^2
Target cross-section σ	$0.01 m^2$

Integrated power from target $P_I = \dfrac{P_T \sigma\ (PRF)\ r_c T_1}{A}$

P_I = 7.5 – 75W (200 x 200 km), 30 – 300W (100 x 100 km)

Figure 6-7. GEO illuminator parameters.

Receivers

$$\text{Received Power } P_R = \frac{P_I A_R}{4\pi R_{TR}^2}$$

(A_R = receiver aperture, R_{TR} = target-receiver range)
Noise power $P_N = kT_RB = 4 \times 10^{-12}$W (receiver temperature T_R = 300 K)
S/N = P_R/P_N = 20 db
Example: Δx = 1m, T_I = 10 sec, 100 x 100 km

LEO Satellite: R_{TR} = 500 km, A_R = 16 m^2
Aircraft: R_{TR} = 100 km, A_R = 0.6 m^2

Figure 6-8. Possible bistatic receiver parameters.

Aside from cost savings, a benefit to aircraft and UAV SARs from receive-only operation is the possibility of stealthy operation of the receiver.

In an ideal world, the more power available to a SAR the better. Power is important to a SAR for resolution, since (all other things being equal) a SAR spatial resolution Δx require power scaling like $(\Delta x)^{-3}$.

Even the power levels we discuss are too low to enable such SARs to be good moving-target detectors of ground vehicles, because the needed integration time is too long to freeze the target. However, as discussed in Section 4.1, advances in processing to the point where a single SAR image can be processed in a fraction of the coherent integration time allow for effective moving-target searches, which require many images to be formed for moving targets in certain speed ranges.

6.2.2 Instant Interferometry

We now discuss an application of bistatic SAR involving the GEO illuminator and a transmit-receive SAR, to form two phase-coherent images simultaneously. This, of course, requires that the transmit-receive SAR acquire both the direct and target-return GEO transmission, as well as its own transmission return, with appropriate time multiplexing.

There are cases where instant Interferometry is not wanted, as in coherent change detection where the two SAR images are separated by at least

the time it takes for change to occur. However, these concepts overlap for interferometric detection of moving targets.

A simplified bistatic geometry is shown in Figure 6-9, with the transmit-receive SAR at altitude H and distance x from a ground target. Assume the SAR velocity is in a direction perpendicular to x (in or out of the paper). The angle above the ground of the GEO beam, called α, is essentially the colatitude. The phase of the low-altitude SAR is set by reception of a direct pulse from the GEO illuminator, so the phase difference to be detected is $\Delta\phi = k(R_2 - R_1)$. For fixed H and α, simple geometry implies that

$$\Delta\phi \;=\; k((H^2 + x^2)^{1/2} - x\cos\alpha - H\sin\alpha). \tag{6-3}$$

Suppose the target moves with velocity u; then

$$\Delta\,\phi \;=\; ku(\cos\beta - \cos\alpha)\,. \tag{6-4}$$

One can work out for oneself various examples; for X-band radar, β should be fairly close to α to avoid too large phase change in a reasonable integration time.

Another application is in three-dimensional terrain mapping. Here we suppose that $H \;=\; H(x)$, so the terrain is sloped. Then from Equation (6-3)

$$\frac{\partial}{\partial x}\Delta\phi \;=\; k(\cos\beta - \cos\alpha \;+\; \frac{\partial H}{\partial x}(\sin\beta - \sin\alpha)). \tag{6-5}$$

For reasonable terrain slopes and equation, it is not hard to reconstruct terrain elevation from the phase difference.

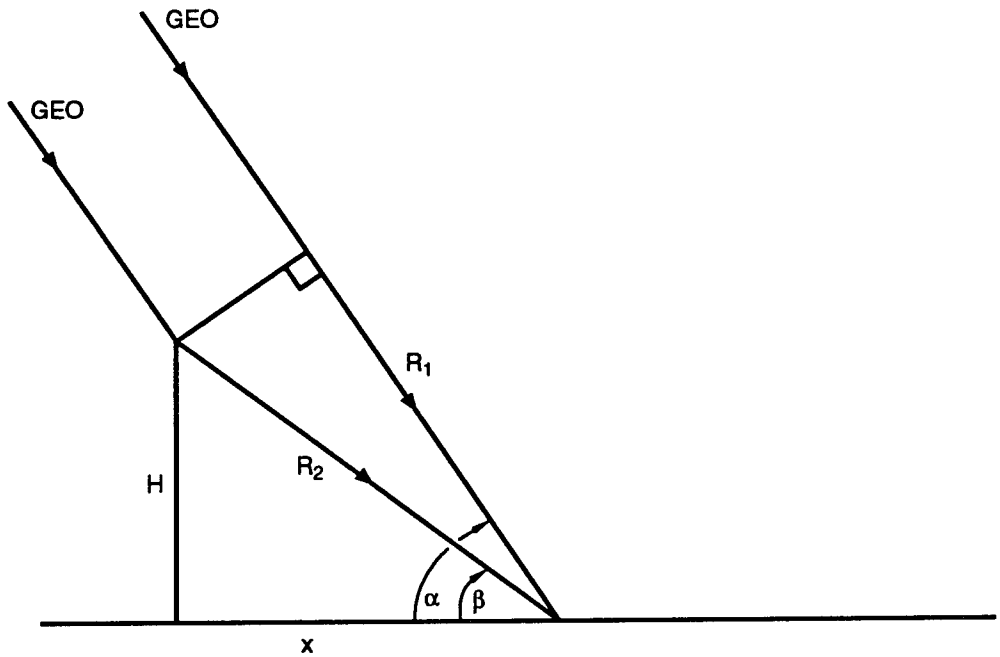

Figure 6-9. Bistatic geometry for GEO illuminator and second SAR at height H, ground distance x from target.

6.2.3 Incoherent 3-D SAR

This is another way of making 3-D measurements on a single pass, using a transmit-receive SAR and differential GPS. The measurement accuracy is limited to that attainable by differential GPS, say 1-3 m. There are favorable and unfavorable geometries for this approach, but in general it is less constrained than the interferometric approach.

The idea is simple. Non-static SAR has SAR spatial resolution in two dimensions only; these lie in the slant plane, which contains the SAR velocity vector and the range vector. In the perpendicular direction, one gets only real-aperture accuracy, far worse than 1-3 m. If, however, the SAR images are taken of the same scene, but with very different slant planes, then the full 3-D scene can be recovered. The accuracy is limited to the accuracy to which the two slant planes' geometries are known, which is where differential GPS comes in. Differential GPS not only gives the SAR position accurate to 1-3 m; it gives, perhaps even more importantly, its velocity accurate to a few cm/ sec.

Normally, with a monostatic LEO SAR, one must wait some time to get the right passes and slant plane geometries. With a GEO illuminator and transmit-receive LEO (or aircraft) SAR, the whole thing can be done at once.

Finally, we note that this accuracy can be translated into 1-3 m absolute accuracy in all three dimensions, relative to a surveyed differential GPS ground beam which can be hundreds of km from the observed scene.

6.2.4 Bistatic Detection of Aircraft

The possibility of bistatic SAR detection of moving aircraft with, e.g., stationary ground receivers has long been recognized, and an experiment along these lines was conducted in 1977 [35] at the Aerospace Corporation. The transmitters were low-power (~ 40 W) GEO communications satellites, like DSCSII and NATO III B, the targets were commercial aircraft at Los Angeles International Airport, and the signals (direct and reflected) were received on a roof-mounted antenna in El Segundo, a few km away. Aircraft were successfully detected with coherent integration times in the range 0.05-0.1s. Figure 6-10 shows a typical Doppler history; the large RCS fluctuations are due to specular scattering "glints" from smooth areas, dihedrals, etc. on the aircraft. More recently the Aerospace Corporation, in collaboration with Wright Labs, conducted a 1993 experiment on bistatic SAR along the lines previously discussed: a GEO illuminator, and a receive-only aircraft SAR to image ground targets. The illuminator was again a GEO communications satellite (DSCS III, with a power of 40 W at a center frequency of 7.5 GHz), and the receiver was a C-135 aircraft with a 26" antenna for receiving ground reflections.

In addition, the Aerospace people have, independently of our discussion, proposed a dedicated GEO SAR illuminators with solar-cell power in the range 100-1,000 W and a 10-m mesh antenna. A notional sketch is shown in Figure 6-11. This illuminator is low-power compared to our proposal, and therefore could not perform at a resolution of ≤ 1 m at the ranges we desire, but is still useful against aircraft, as Figures 6-12 and 6-13 shows. We

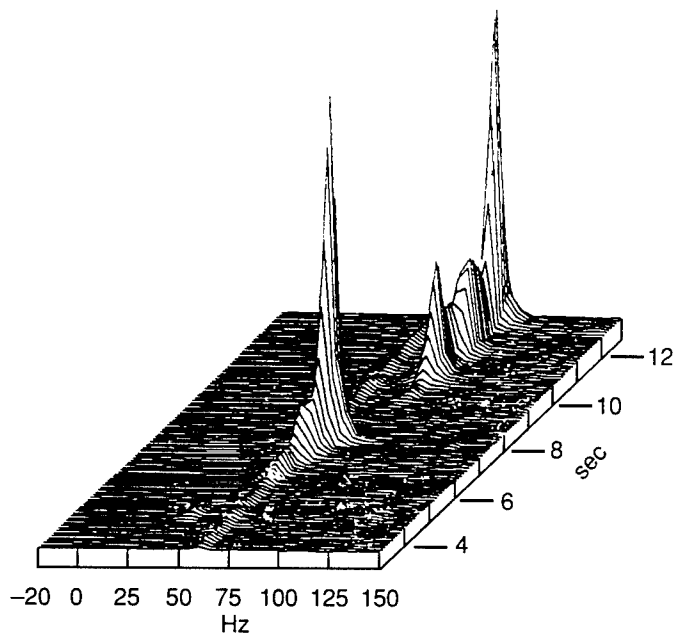

Figure 6-10. Incoming aircraft spectral sequence; NATO III B transmitter, 7–point smoothing. (from Avrin, 1980).

Bistatic Radar Illuminator Satellite

1000 W transmitted power, 10 m diameter deployable mesh antenna, gallium arsenide solar array/nickel hydrogen battery electric power system

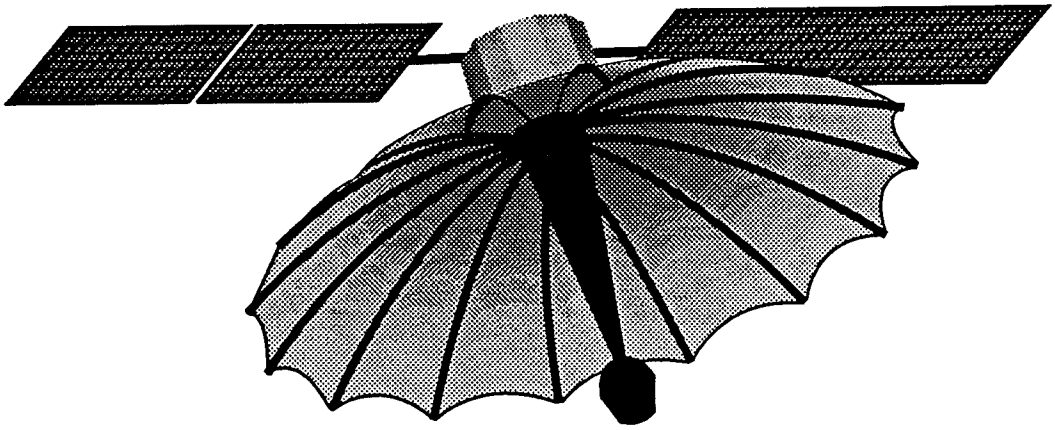

Figure 6-11. Bistatic GEO SAR illuminator (from Duchs et al, 1993).

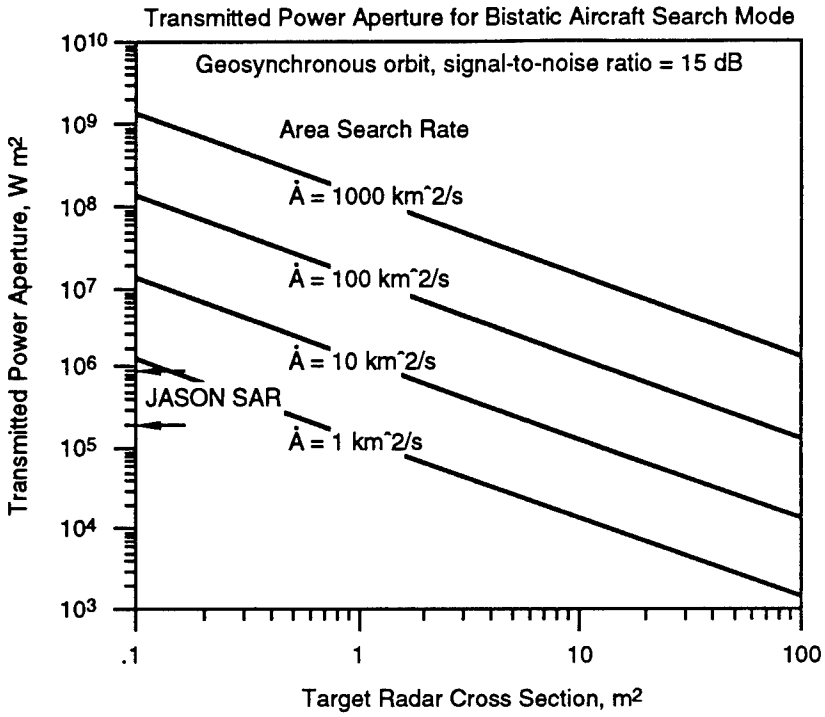

Figure 6-12. Area search rate is a function of power – aperture product and RCS (from Duchs et al, 1993).

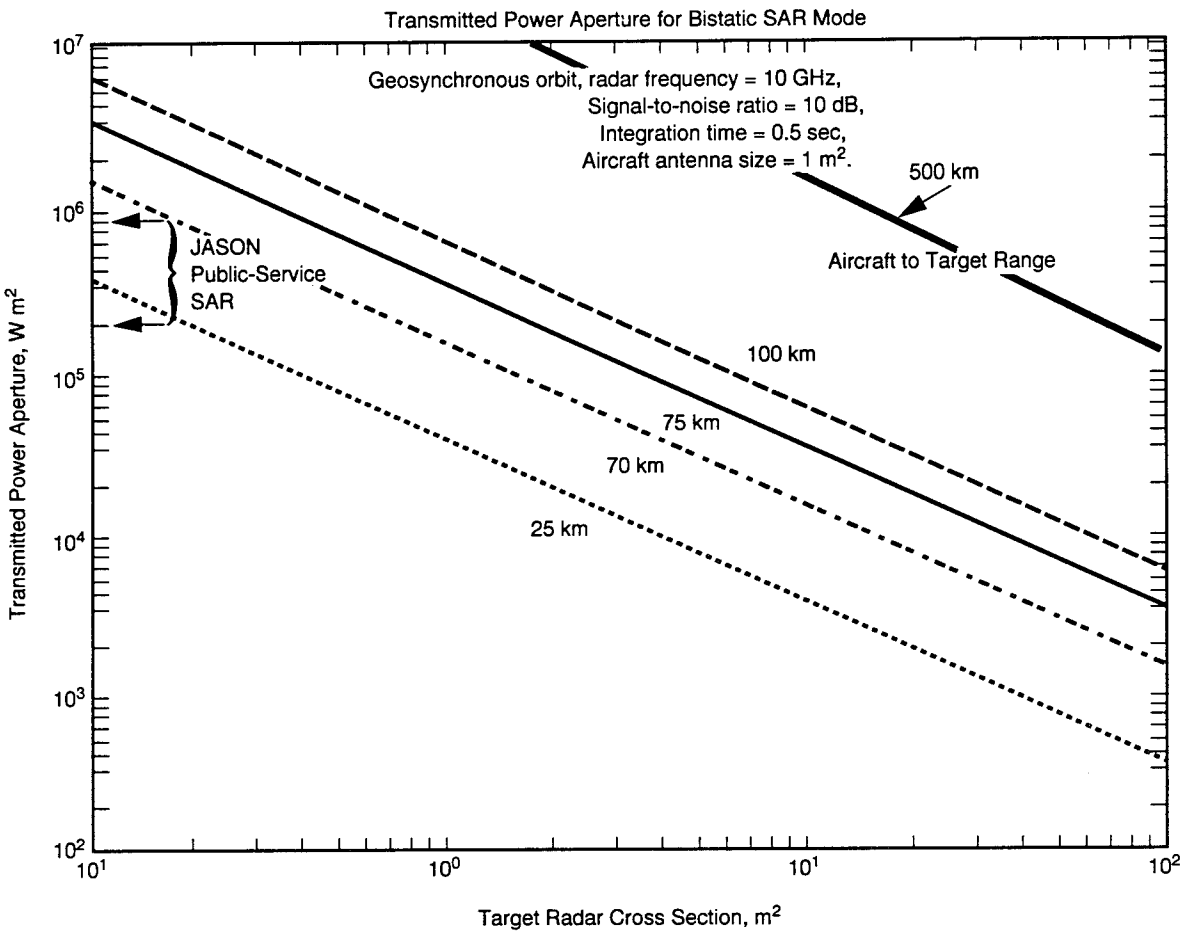

Figure 6-13. Detection range as a function of power-aperture product and RCS (from Ducles et al. 1993)

have indicated in these figures the range of power-aperture products of our public-service SAR per Figures 6-6 and 6-7. Useful detection can be achieved to several hundred km against aircraft of RCS $\sim$ 10 m^2. Please note that Figure 6-13 from [36], refers to detection of ground targets from an aircraft, but it can be read as applying to aircraft detection from the ground, for which a shorter integration time T_I and larger receiver aperture A_R would be desirable. The detection range scales like $(T_I A_R)^{1/2}$.

The Aerospace people estimate that the cost of two 1,000 W illuminators, including RDTE, would be $410M.

6.3 Low-Earth-Orbit "Bistatic" Battlefield SAR

The motivation for this section is to outline how potential advances in workstation scale computers coupled with a modest constellation of simple, low-cost, LEO satellites will enable SAR-like microwave images of the battlefield to be created where they are to be used—in forward command posts. Since the ground stations are simple, they can be proliferated and a single illuminator satellite will have many users. This, too, is a "public-service". SAR, but with revisit times limited by satellite overpasses instead of the continuous coverage afforded by a GEO SAR transmitter.

Whenever relative motion changes the phase of a coherent radar signal received from a scattering element in a known, deterministic way, one can in principle apply phase coherent (SAR-like) processing to obtain an image of

the scattering object. Well-known examples are standard SAR images and inverse synthetic aperture radar images of ships.

This section investigates the imaging capability of a system composed of a transmitter in a low earth orbit satellite and stationary ground-based receiver. The commonly used term "bistatic" does not rigorously apply to this system because satellite motion is essential for imaging. Since the only functions of the satellite are to transmit a coherent radar pulse, satellite ephemeris data, and a steady carrier, the satellite should be relatively cheap, permitting one to acquire a sufficient number so that images are available frequently. In the example below, each satellite transmitter will have an average power of 1 kw and provide images in a swath of width 2,000 km, so a constellation of 6 polar orbiting satellites will permit a new image every two hours. The average power of 1 kw is needed only for several hundred seconds while the satellite passes over the active theatre. The orbit-average power is less than 10 watts. The concept expands easily to 50 satellites and a 15 minute revisit time. Figure 6-14 is a cartoon of the concept.

The ground receiving station consists of two simple antennas—one to acquire a direct signal from the satellite and a second antenna that points towards the battlefield area to be imaged. Timely data processing calls for a workstation scale computer, upgraded to have a 2 gigabyte DRAM memory. Such units are not yet available commercially, but could be designed using commercial parts (see Section 3.4). An image should be available within 100 sec of satellite passage.

The microwave image will have 1-meter resolution and, of course, only

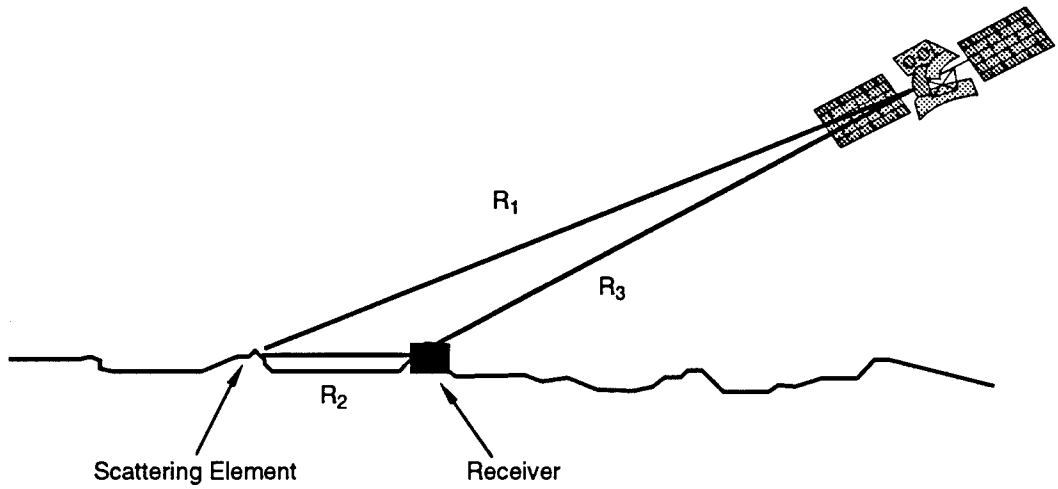

- Low earth orbit satellite illuminator combines with cheap, proliferated ground-based receivers to image line-of-sight area from receiver.
- Difference range $\Delta R = R_1 + R_2 - R_3$ and phase $2\pi \Delta R/\lambda$ evolve by satellite motion, providing basis for SAR.

Figure 6-14. "Bistatic" battlefield SAR concept.

terrain that is line-of-sight from the receiving antenna will contribute to the image. Thus, one will want the antenna to be located on high ground, be raised on a pole, etc. All the principles of this section also apply to receiving antennas on an RPV which would greatly extend the line-of-sight terrain. However, the fixed receiver is appropriate for the first test of this concept and simplifies deployment. Indeed, if one is to have an RPV, why not put a 100 W transmitter aboard and have continuous imagery?

The advantage of microwave images is that they are all weather and not degraded by battlefield smoke and haze. Since the receiving station is simple and rugged, it can be mobile and move with armor and troops. It need be stationary only during a several minute period when the satellite is passing by. Most importantly, the microwave image is created where it is to be used, in a forward area command post. There is no need for communication links to RPV's or to the rear to transmit data. All the signals discussed in this section could be transmitted in a spread-spectrum, encrypted format to deny the microwave imaging capability to adversaries. The procedure would be similar to P-code Global Positioning System encryption.

Figure 6-15 illustrates the concept. A satellite ground track passes within $y \approx 1,000$ km of the area to be imaged. We envision that the satellite altitude z will be $z = 700$ km to obtain a $2,000$ km illuminated swath width. The satellite radar beam is narrow in the along-track direction and sweeps across the area to be imaged. A series of radar pulses is emitted from the satellite and the ground station receives both the direct and scattered radar signals. Imaging is performed based on the delay ΔR and phase evolution $\Phi = 2\pi\Delta R/\lambda$ of the scattered signal relative to the direct signal. Figure 6-15

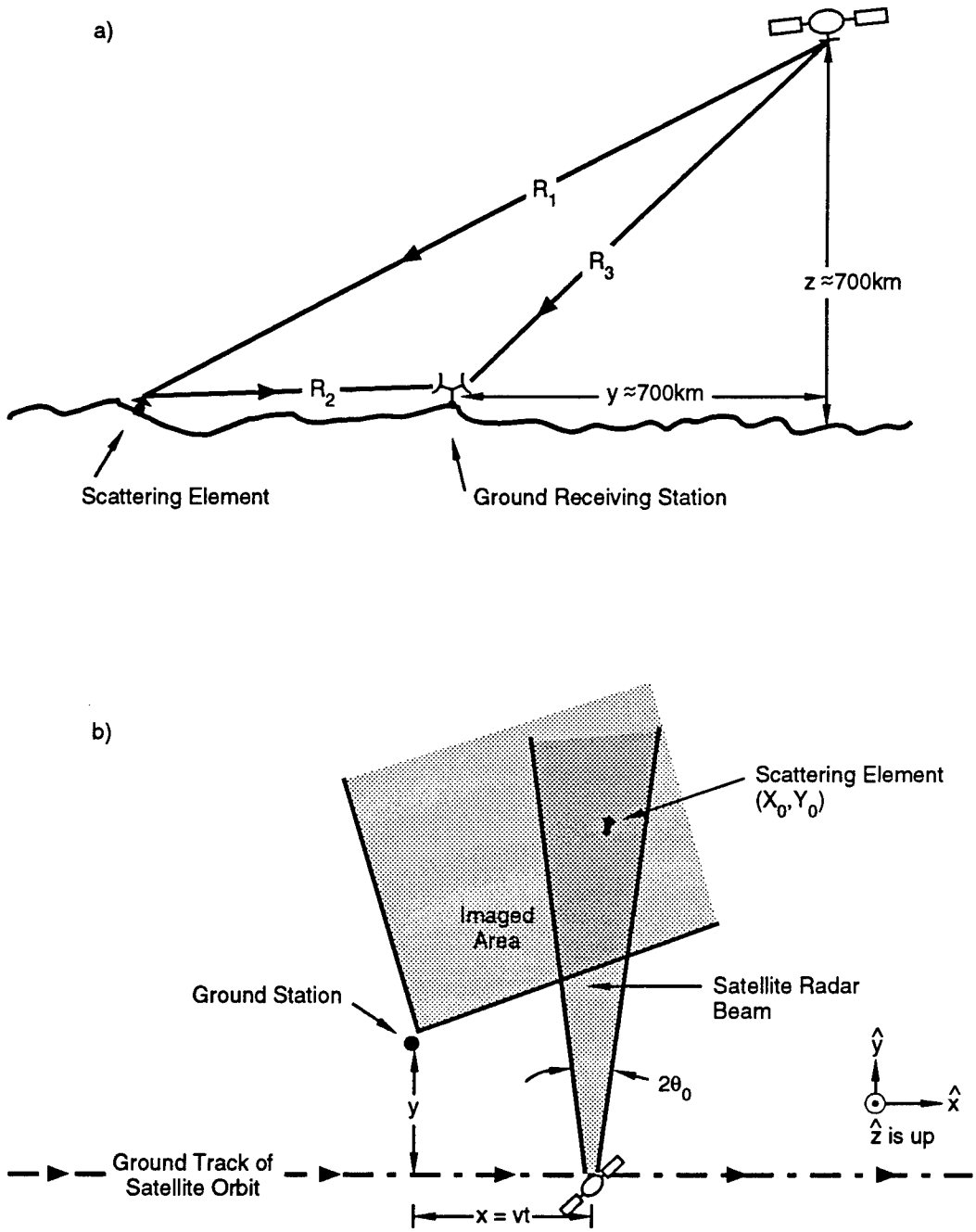

Figure 6-15. Battlefield microwave imaging system. a) Elevation view portraying scattered versus direct path. b) Plan view. Narrow satellite radar beam sweeps over area to be imaged.

illustrates the geometry for calculating $R\Delta R$

$$\Delta R = R_1 + R_2 - R_3 \tag{6-6}$$

$$R_1 = \left[R^2 + x^2 + 2\,\vec{R}\cdot\vec{r}_o - 2xx_o + r_o^2\right]^{\frac{1}{2}} \tag{6-7}$$

$$R_2 = r_o = (x_o^2 + y_o^2 + z_o^2)^{\frac{1}{2}} \tag{6-8}$$

$$R_3 = \sqrt{x^2 + R^2} \tag{6-9}$$

$$x = Vt \qquad \vec{R} = \hat{y}y + \hat{z}z. \tag{6-10}$$

Here R denotes the distance of closest approach between the satellite and the ground station; $\vec{R}$ the satellite-to-ground-station separation vector at closest approach, and $\vec{r}_o$ is the location of the scattering element relative to the ground station. The presentation of this work uses a flat-earth approximation which simplifies the algebra but retains correct resolution estimates. We envision the characteristic size of the imaged area is $r_o \sim 10\,\text{km} << R \approx 10^3$ km. Thus, one can expand Equation (6-7) and express ΔR as

$$\Delta R = \frac{\vec{R}.\vec{r}_o - xx_o}{(R^2 + x^2)^{\frac{1}{2}}} + r_o. \tag{6-11}$$

Higher order terms in the expansion for ΔR are needed to compute range variation at the 1.0 meter accuracy level needed for mapping purposes. Expression (6-11) does represent the total range variation and suffices for image accuracy estimates. Note that ΔR depends on the combination

$$\frac{\vec{R}\cdot\vec{r}_o}{R} = \frac{yy_o - zz_o}{(R^2 + x^2)^{\frac{1}{2}}}$$

and thus a scattering element located at y_o, z_o will appear at $y_o' = y_o - \frac{z}{y}z_o$ in the microwave image. Henceforth, we ignore the difference between y_o' and

y_o and write ΔR as

$$\Delta R = \frac{yy_o - xx_o}{(R^2 + x^2)^{\frac{1}{2}}} + r_o, \tag{6-12}$$

where y_o now stands for y_o'. Note that the magnitude of the variation of the first term with satellite along track position x is of the magnitude of the size of the microwave image.

The microwave image is formed by the customary technique of convolving the data set against the point-scatter response function

$$I(x_o, y_o) = \int\int drdx e^{-\frac{2\pi}{\lambda} i\Delta R} \delta(r - \Delta R) s(r, x), \tag{6-13}$$

where $s(r, x)$ represents the complex data set which has been compressed in range. It is assumed that x and R are precisely known by comparing the directly received satellite phase against the expected result

$$\phi(x) = \frac{2\pi}{\lambda}\sqrt{R^2 + x^2}. \tag{6-14}$$

The satellite velocity v and y are known from empheresis data.

Let us first address the accuracy of the microwave map, given full implementation of convolution (6-1). This implies the range migration interpolation

$$r(x_o, y_o, y, x') = \sqrt{x_o^2 + y_o^2} + \frac{yy_o - x_o^2 - x'x_o}{[R^2 + (x' + x_o)^2]^{\frac{1}{2}}} \tag{6-15}$$

is carried out so the convolution becomes

$$I(x_o, y_o) = \int dx' e^{\frac{-2\pi i \Delta R}{\lambda}} e^{\frac{-x'^2}{R^2 \Theta_o^2}} s(r, x') \tag{6-16}$$

where $x' = x - x_o$. In Equation (6-13), we have introduced a Gaussian along-track satellite antenna pattern for tractability. Here $2\Theta_o$ denotes the beamwidth.

Let us suppose that the chosen values of x_o and y_o depart by small amounts δx_o δy_o from the actual location of the scattering element. Then the x' integration becomes

$$I(x_o, y_o) \ \alpha \ \frac{1}{\sqrt{\pi}} \int \frac{dx'}{R\Theta_o} e^{\frac{-x'^2}{R^2\Theta_o^2}} e^{i\Phi} \tag{6-17}$$

where

$$\Phi(x', \delta_{xo}, \delta_{yo}) = \frac{2\pi}{\lambda} \frac{y\delta y_o - x'\delta x_o}{(R^2 + x'^2)^{\frac{1}{2}}} + \text{higher order terms.} \tag{6-18}$$

An adequate approximation to Φ is

$$\Phi = \frac{-2\pi}{\lambda} \left[\frac{y\delta y_o}{R^3} x'^2 + \frac{x'\delta x_o}{R} \right]. \tag{6-19}$$

This approximation permits an analytic evaluation of Equation (6-17).

$$I(x_o, y_o) = \frac{\exp\{-\frac{(2\pi)^2\Theta_o^2(\delta x_o)^2}{\lambda^2(1+\frac{2\pi i\Theta_o^2 y\delta y_o}{\lambda R})}\}}{(1 + \frac{2\pi i\Theta_o^2 y\delta y_o}{\lambda R})^{\frac{1}{2}}}. \tag{6-20}$$

Thus the image resolution $\Delta x = 2\delta x_o$ is

$$2\delta x_o = \frac{\lambda}{\pi\Theta_o} = \Delta x. \tag{6-21}$$

Because the phase associated with δy_o varies more slowly, the phase compression doesn't determine δy_o as accurately as δx_o.

The value of δy_o is determined by the accuracy of the range resolution δr. From Equation (6-15), we deduce

$$\delta r = \frac{x_o\delta x_o + y_o\delta y_o}{r_o} + \frac{y\delta y_o}{R} - \frac{x'}{R}\delta x_o. \tag{6-22}$$

Thus

$$\delta y_o = \frac{1}{\frac{y_o}{r_o} + \frac{y}{R}} \left(\delta r - \frac{x_o}{r_o}\delta x_o \right), \tag{6-23}$$

where we have neglected $x'/R \sim \Theta_o \ll 1$. Thus resolution in δy_o is comparable to the larger of the range resolution δr or δx_o. One should note that if the imaged area lies between the satellite ground track and the receiver (negative y–values), then y_o–resolution can be poor.

The computional requirements for the ground station will depend on the number of data pixels. Let us turn to the question of how many samples are needed to acheive a resolution $\Delta x = 2\delta x_o$. An estimate of the maximum Doppler shift is

$$\nu_D = \frac{1}{\lambda}\frac{\partial(\Delta R)}{\partial x}V = \frac{V x_o}{R\lambda}. \tag{6-24}$$

The sampling time is $t_s = 2R\Theta_o/V$ so the total number of samples to satisfy the Nyquist criterion is

$$N_{sx} = 2\nu_D t_s = \frac{4}{\pi}\frac{x_o}{\Delta x} \approx 1.3 \times 10^4 \left(\frac{1\,\mathrm{m}}{\Delta x}\right), \tag{6-25}$$

where the estimate $y_o \sim 10$ km and Equation (6-21) were used. It also follows that the radar PRF must be

$$\mathrm{PRF} = \frac{2\,V\,x_o}{R\,\lambda} = 5\mathrm{kHz}\left(\frac{3\,\mathrm{cm}}{\lambda}\right), \tag{6-26}$$

which is representative of standard radar technology. The unambiguous range is R_{max}, which is

$$R_{\mathrm{max}} = \frac{c}{2\cdot\mathrm{PRF}} \approx 30\,\mathrm{km}\left(\frac{\lambda}{3\,\mathrm{cm}}\right) \tag{6-27}$$

normally sufficient to place terrain beyond the microwave line of sight. Should additional unambiguous range be desired for RPV-based receivers, one can transmit a sequence of orthogonal Costas pulses so that range returns from different pulses vanish upon range compression.

Range resolution δr calls for a waveform bandwidth

$$B = \frac{c}{\delta r} = 300\,\mathrm{MHz}\left(\frac{1\,\mathrm{m}}{\delta r}\right) \tag{6-28}$$

and the number of samples required in range for each radar pulse is

$$N_{sr} \approx \frac{4\,r_o}{\delta_r} \approx 4 \times 10^4 \left(\frac{1\,\mathrm{m}}{\delta r}\right) \tag{6-29}$$

where $r_o \approx 10$km. However, if one restricts the pulse length to $\tau_p < 10\mu$sec, one can break up the range problem into roughly 10 overlapping images, each extending 2 km in range and requiring only 8×10^3 range samples per image.

Overall, an image calls for $6 \cdot 10^8$ data samples, requiring two gigabytes of DRAM memory. A computer capable of roughly 100 M FLOPS with the storage is necessary for this ground station

What signal-to-noise ratio can be expected for this system? The usual radar equation yields the signal-to-noise expression

$$\frac{S}{N} = M\frac{U_p(\sigma_o \Delta x \delta r)\lambda^2 G}{A_o(4\pi)^2 r_o^2 (k\,T_n)}. \tag{6-30}$$

Here U_p denotes the radar energy per pulse, M the number of coherent pulses, $(\sigma_o \Delta x \delta r)$ the radar cross section associated with a pixel of size $\Delta x \delta r$, A_o the area illuminated by the satellite antenna, G the gain of the receive antenna and r_o the range from a pixel element to the receiver. Let us discuss each of these terms separately. From Equation (6-25), we find the number of coherent pulses in

$$M = N_{sx} = \frac{4x_o}{\pi(\Delta x)}. \tag{6-31}$$

The area illuminated by the satellite antenna is assumed to have a swath width $2R$

$$A_o = 2R(2R\Theta_o) = \frac{4\,R^2\lambda}{\pi(\Delta x)} \tag{6-32}$$

where Equation (6-21) has been used. The radar energy-per-pulse is related to the average power $< P >$ via

$$U_p = \frac{< P >}{\text{PRF}} = \frac{< P > R\lambda}{2\,V x_o}. \tag{6-33}$$

The receive antenna is designed to have a wide beamwidth of 90° in the azimuth direction and a narrow beamwidth vertically $\Theta_v = 10^{-1}$ radians. Thus

$$G = \frac{4\pi}{\left(\frac{\pi}{2}\right)\Theta_v} = 80. \tag{6-34}$$

Lastly, we assume a receiver-only system can achieve a noise-temperature $T_n \approx 200°$ K so that $kT_n = 2.8 \times 10^{-21}$ joules. Let us combine Equations (6-30) – (6-34) into the formula

$$\frac{S}{N} = \frac{< P > \lambda^2 G(\sigma_o \Delta x \delta r)}{2\,V\,R\,r_o^2 (4\pi)^2 (kT_n)} \tag{6-35}$$

$$= 20\left(\frac{< P >}{1kW}\right)\left(\frac{\sigma_o \Delta x \delta r}{0.1\ \text{m}^2}\right)\left(\frac{\lambda}{3\ \text{cm}}\right)^2 \tag{6-36}$$

and we used $R \approx 10^6$ m, $r_o \approx 10^4$ m, $V = 7.5 \times 10^3$ m/sec. A value of $\sigma_o \approx 0.1$ is representative of x-band radar ground scatter data. One should note that the average radar power of $< P >= 1\,kW$ is needed only for 100-200 secs while the satellite flys over the theater of operation. During the rest of its orbit, it can store energy collected by solar cells in a battery. The orbit-average power load is less than 10 watts.

A more elaborate receive antenna could improve the signal-to-noise ratio considerately, without exceeding a size of 1 meter. At x-band, our nominal antenna with $G = 10^2$ has physical dimensions of 3 cm width and 35 cm height. If a $(0.5\,\text{m})^2$ 16-element phased-array receive antenna were used, then a factor of 25 improvement in signal-to-noise would result.

Let us collect the properties of the satellite radar needed in Table 6.1. Implied in this table is the fact that the radar pulse energy goes up in proportion to the wavelength, while the average power remains fixed (see Equation (6-34). Table 6.1 also reflects the fact that σ_o decreases as the wavelength increases.

Overall, this section demonstrates that a microwave imaging capability can result from aggressive use of current satellite and receiver technology as well as computer hardware parts in a new system. More thought needs to be given to the implementation of the image-forming computation, especially the range migration issues implied by Equation (6-15).

Recommendation:

Tests of the principles of this microwave imaging concept can be carried out using the signals of SAR satellites now on orbit. These satellites are designed to have $\approx$ 10 m resolution so a full 1 m resolution would not be achievable. But such a research program would involve only passive receivers and computation, and, therefore, be quite cheap.

Table 6.1. Parameters of Satellite Radar Transmitter.

Parameter	$\lambda = 3$ cm	$\lambda = 10$ cm
Altitude	700 km	700 km
$< P >$	1kW	1kW
PRF	5 kHz	1.6 kHz
$2\Theta_0$ – Along Truck Antenna Beamwidth	1.2°	3.6°
Bandwidth	300 MHz	300 MHz
Image Resolution	$(1\ m)^2$	$(1\ m)^2$
Across Track Swath Width	2000 km	2000 km
σo	0.10	0.01
S/N/ Simple Antenna	20	20
S/N/ Phased Array Antenna	500	500

7 CONCLUSIONS

We have examined the role of massively parallel computers (MPC) in SAR processing. SAR phase coherence implies not only images of radar scattering cross section regardless of weather, but also images of small shifts in topography of a fraction of a radar wavelength, and measurement of object motion (for example oscillating objects). Massive parallel computing applied to SAR allows small lightweight instruments, timely characterization of object motion and vibration, characterizations of environmental parameters, detection of small changes in scenes over time, opportunities for innovative SAR configurations and missions, and production of 3D images.

In Section 2 we have reformulated the SAR algorithm in order to evaluate various approximation schemes that have historically been used and to compare their computational requirements and their effects on image quality with those of possible future algorithms made feasible by MPC. In Sections 2.3, 6.1.1 and 6.1.3, we have evaluated the use of pseudorandom-sequence waveforms for SARs. While we have not found any superiority in resolution or computational algorithms, the effective encryption serves to conceal basic SAR parameters. In Sections 2.4 and 2.5 we have formulated an exact inversion algorithm for SAR, and have avoided the Fraunhofer or Fresnel approximations, but we have not ourselves found a numerically efficient algorithm (equivalent to the FFT) for our resulting equation. In Section 2.6 we have suggested an alternative to the usual computationally-intensive step of polar reformatting. In Section 2.7 we have described several classical pro-

cessing schemes and indicated how they all are capable of achieving required accuracies of pixel phase so that change detection algorithms can be used.

In Section 2.8 we have described the expected order-of-magnitude effects of atmospheric and ionspheric heterogeneities on SAR phase. We conclude that these effects can be substantial, especially at larger radar wavelengths for ionspheric effects and smaller radar wavelength for atmospheric effects. In cases where the effects are substantial, SAR information can be used as a probe of these environmental heterogeneities (see Sections 4.4 and 4.5).

We point out that environmental effects can be removed by comparing returns at two different wavelengths. This could be crucial for developing a reliable instrument for change detection, or for developing a sensor for environmental effects (see Section 4.5.4).

In Section 3 we have evaluated a number of commercially-available MPCs in a SAR context. We find that general-purpose massively parallel computers (MCPs) are available that can process a SAR image. Small systems (64 processors) can process a 16 K $\times$ 16 K image in about one minute. Large systems (1024 processors) can process an image in a few seconds. The capability of MPCs is expected to improve at a rate of 40% per year.

Special-purpose processors are currently about 100 times more cost effective than general-purpose processors. This gain comes from improved arithmetic density [100s of arithmetic logic units (ALUs) vs a few], more efficient use of memory bandwidth (because of direct ALU-ALU connections), and low-precision arithmetic (24 bits vs 64 bits). The advantage of special

purpose processors is expected to increase over time as increased chip densities enable larger numbers of arithmetic units and more exploitation of local ALU-ALU bandwidth.

The capability of special-purpose SAR processors and large MPCs enables computationally intensive methods of exploiting SAR data.

Section 4 focussed on novel methods for exploitation of SAR data with advanced parallel computing. These methods concerned moving targets, shadows, ionspheric and atmospheric scintillation, azimuthal scan SAR, battlefield scanning SAR and a variety of dual-use environmental applications. In general we found that a parallel computing architecture was well suited to these new methods and that the speed advantage of parallel machines was essential to applying these methods to a large body of SAR data in a timely manner.

Section 4.1 discusses problems associated with moving targets. Measurements of moving targets present a fundamental problem for SAR in that the number of unknowns of position (x,y) and velocity (V_x, V_y) exceeds the number of measurements available from a single SAR. This problem can be addressed by using monopulse techniques to determine azimuthal position, invoking a prior knowledge such as location of roads, measurements by two separated SARs or subaperture processing. A further method is to use subaperture processing on the shadows of objects as well as the objects themselves, since the shadow does not include a radial velocity to complicate the problem. Frequency domain processing can also be used to recover information on moving targets.

Section 4.2 discusses SAR Processing for Airborne Azimuthal Scan Radars. Advanced parallel computing makes possible synthetic aperture processing for azimuthal scan radars, such as periscope and AWACS radars. Azimuthal resolution can be enhanced by a factor of ~ 100 while the antenna may become smaller and cheaper depending on sensitivity requirements. A case in point is airborne periscope-detection radars. We conclude that it is practical to add a SAR-mode to upgrades of existing periscope radars with the result being a factor ~ 100 increase in azimuthal resolution and a corresponding decrease in the clutter patch size.

As discussed in Section 4.3, SAR mode added to a conventional aircraft-borne azimuthal scan radar (as discussed in Section 4.2) would allow both high azimuth resolution and moving target identification. To make such enhanced performance available to battlefield commanders in a timely manner parallel computation capabilities are required.

As discussed in Section 4.5, SAR measurements of land and ocean characteristics are greatly aided by SAR observations at multiple frequencies and polarizations. Advanced parallel computing makes possible the processing and interpretation of the large data sets commensurate with environmental observations. This conclusion is illustrated by an example from sea ice observations by multi-frequency, multi-polarization SAR.

Section 5 addresses possible counter-measures to SAR. For any individual target, standard radar concealment techniques (radar nets, placement within foliage) can evidently mask the target. Radar nets, however, can be potentially separated from background terrain by use of polarization comparisons

between a transmit-vertical, receive-vertical (VV) signal and (VH, HH, HV) signals which will differ for background and radar-net signals. Moreover, the addition of radar glint points can confuse a SAR target signature. But again, this will differ from background. Similar remarks apply to hiding targets with stealth-like planar reflecting sheets. In general, while the specifics of a target can be protected by concealment, SAR's are well-suited to recognize the existence of concealment.

Jamming is a well-known radar countermeasure. SAR's, especially with the new waveforms of Section 6, are resistant to jamming because of the extensive processing (effectively filtering) which must be done to generate a radar image. Nonetheless, future SARs should make use of adaptive nulling antennas and random waveforms to deny adversaries the possibility of creating false-target, decoy signals.

False signals associated with vibrating target surfaces are generally quite weak and not an important countermeasure.

To our knowledge, SAR-specific radar countermeasures are only at the most rudimentary state of development and thus unlikely to be deployed by third-world adversaries.

Section 6 notes that the principles of SAR processing permit configurations quite different from the standard side-looking SAR in an aircraft or in a satellite. SAR image formation needs only a high-bandwidth signal to attain high resolution in a generalized range coordinate and a time-varying transmitter-target-receiver path to achieve resolution in a second dimension.

This forms two-dimensional SAR images; the third dimension is effectively unresolved.

In the time-bandwidth domain, waveforms can be engineered to serve a variety of purposes. Costas/Maric codes have ambiguity functions decidedly superior to common linear frequency ramps and are also useful at rejecting scattered signals from areas outside of the desired swath width in LEO satellite applications. Random stochastic waveforms and pseudorandom cyclic difference sets yield waveforms which convey minimal information regarding SAR objectives even to the extent that one can not be sure that SAR processing is being used at all. We conclude that theoretical and experimental development of advanced waveforms should be carried out. In particular, the domain of the ambiguity function should be extended to encompass several bursts.

A corollary to the preceding paragraph is that transmitter tubes with poor phase and amplitude control are perfectly satisfactory for SAR applications. One need only have the ability to measure the transmitted waveform.

SAR systems can have separated transmitters and receivers. While such a configuration is often called "bistatic," this cannot be rigorously true because a time-varying transmitter-target-receiver path length is needed for SAR imaging. Thus one can envision "public service" SAR transmitters located in geosynchroneous orbit with receivers located on moving aircraft, UAV's, or LEO satellites. An alternative configuration is a fixed receiver which would be sensitive to a moving (aircraft) target. Indeed, such systems have been demonstrated. Figures 6-6 and 6-7 illustrate that a geosynchro-

neous SAR illuminator could be built (albeit at some expense) with present technology. In addition to the usual area images, a public service SAR is in principle capable of (1) instant interferometry or, in other words, moving target identification, (2) incoherent 3-dimensional imagery, and (3) aircraft detection. Each application requires considerably more theoretical development to identify a data processing algorithm that would mesh with new computing capabilities. But the requisite information resides in the SAR signal and only needs to be extracted.

One can also envision a system consisting of a constellation (6-50 depending on desired revisit times) of cheap, low-earth-orbit satellite emitters, that would enable SAR imaging by either stationary or UAV-borne SAR receivers. A stationary SAR receiver was shown to be small, cheap and able to attain 1 m $\times$ 1 m resolution over a battlefield area of 10 km $\times$ 10 km. It is recommended that a demonstration of such a system be carried out by exploiting the signals of SARs currently in orbit, which could, of course, serve as LEO transmitters in the absence of a dedicated constellation.

Overall, SAR signals, especially those dedicated to change detection or with moving targets, contain enormous amounts of unexploited information. The principles for information extraction exist and it has been data processing—computation—that has limited SAR techniques. Straightforward development of special purpose massively parallel (but NOT massively expensive) computers is the key to unleashing the ultimate potential of SAR methods.

A PROOF OF EQUATION (2-34)

It is sufficient to prove the inversion Equation (2-34) when $f(r,c)$ is any plane wave

$$f(r,c) = \exp\,(i(\alpha r + \beta c)). \tag{A-1}$$

In this case Equation (2-33) becomes

$$g(a,b) = \int \exp\,(i(\alpha a + (\alpha b + \beta)c)dc = 2\pi\delta(\alpha b + \beta)\,\exp\,(i\alpha a). \tag{A-2}$$

Using the Fourier representation Equation (2-25) of $\phi(x)$, the right side of Equation (2-34) becomes

$$RHS = \frac{1}{2\pi}\int\int \delta(\alpha b + \beta)\exp\,(i\alpha a)dadb \int |\mu| d\mu \exp\,(i\mu(r - a - bc)). \tag{A-3}$$

In Equation (A-3) the integration over a gives $2\pi\delta(\alpha - \mu)$, and so

$$\begin{aligned} RHS &= \int \delta(\alpha b + \beta)|\alpha|\exp\,(i\alpha(r - bc))db \qquad \text{(A-4)} \\ &= \int \delta(s + \beta)\exp\,(i(\alpha r - sc))ds \\ &= \exp(i(\alpha r + \beta c)), \end{aligned}$$

which verifies Equation (2-34).

B PROOF OF EQUATION (2-42)

To calculate n^2, we multiply Equation (2-35) by its complex conjugate, using Equation (2-6), and pick out the second term on the right of Equation (2-41). The result is

$$\begin{aligned} n^2 &= (2V/\pi^2)^2 \int\int\int\int f(r_1c_1)f^*(r_2c_2)dr_1dc_1dr_2dc_2 \\ &\int\int\int\int dt_1dt_2dt'dt''(t_1-t')^2(t_2-t^1)^2(t_1-t'')^{-2}(t_2-t'')^{-2} \\ &\phi(t_1-t'-2r+Vc(t_1+t'))\phi(t_2-t'-2r+Vc(t_2+t')) \\ &\delta(t_1-t''-2r_1+Vc_1(t_1+t''))\delta(t_2-t''-2y_2+Vc_2(t_2+t'')). \end{aligned} \tag{B-1}$$

We express each of the last four factors in (B.1) as a Fourier integral

$$\phi(t_1-t'-2r+Vc(t_1+t')) = \frac{1}{2}\int |\lambda_1| d\lambda_1 \exp\,(i\lambda_1(t_1-t'-2r+Vc(t_1+t')), \tag{B-2}$$

$$\delta(t_1-t''-2r_1+Vc_1(t_1+t'')) = (2\pi)^{-1}\int d\mu_1 \exp(i\mu_1(t_1-t''-2r_1+Vc_1(t_1+t'')), \tag{B-3}$$

and so on. With an error of relative order V, we replace the factor $(t_1-t')^2$ by $(2r)^2$ and so on. The integrations over (t_1, t_2, t', t'') then give delta–functions, and so we obtain

$$\begin{aligned} n^2 &= (2V/\pi)^2 \int\int\int\int f(r_1c_1)f^*(r_2c_2)dr_1dc_1dr_2dc_2 \\ &(r^2/r_1r_2)^2 \int\int\int\int |\lambda_1||\lambda_2| d\lambda_1 d\lambda_2 d\mu_1 d\mu_2 \\ &\exp\,[-2i(\lambda_1 r+\lambda_2 r+\mu_1 r_1+\mu_2 r_2)] \\ &\delta(\lambda_1+\mu_1+V(c\lambda_1+c_1\mu_1))\delta(\lambda_2+\mu_2+V(c\lambda_2+c_2\mu_2)) \\ &\delta(\lambda_1+\lambda_2-Vc(\lambda_1+\lambda_2))\delta(\mu_1+\mu_2-V(c_1\mu_1+c_2\mu_2)). \end{aligned} \tag{B-4}$$

Again neglecting terms of relative order V, the delta-functions in Equation (B-4)imply

$$\lambda_1 = -\lambda_2 = -\mu_1 = \mu_2, \tag{B-5}$$

and the multiple integral reduces to

$$n^2 = (2V/\pi)^2 \int\int\int\int f(r_1c_1)f^*(r_2c_2)dr_1dc_1dr_2dc_2(r^2/r_1r_2)^2. \tag{B-6}$$
$$\frac{1}{2}\int \lambda^2 d\lambda \exp[2i\lambda(r_1 - r_2)]\delta[V\lambda(c_1 - c_2)].$$

since

$$\delta[V\lambda(c_1 - c_2)] = (V|\lambda|)^{-1}\delta(c_1 - c_2), \tag{B-7}$$

and

$$\phi(2(r_1 - r_2)) = (1/4)\phi(r_1 - r_2), \tag{B-8}$$

Equation (B-6) immediately reduces to Equation (2-42).

C SAR ON A SPHERE

In this section we discuss exact inversion of SAR data when the surface to be imaged is a sphere rather than a plane. We hope that this will have application to SAR imaging of the Earth from orbit, or in other situations where the curvature of the planet is not negligible.

The problem is to reconstruct the radar reflectivity $\sigma(\theta, \phi)$, where (θ, ϕ) are the standard spherical polar coordinates, $\theta \in [0, \pi]$ being the colatitude and $\phi \in (-\pi, \pi]$ the longitude. The antenna follows an orbit that is a great circle in the plane $\theta = \pi/2$. The orbital radius $R' = R + h$, where R is the radius of the Earth and h is the altitude of the antenna above the sphere. At any instant, the antenna can "see" a spherical cap. The angle subtended at the center of the sphere between the edge of this cap and the antenna itself is

$$\gamma_{\max} = \arccos(R/R'). \tag{C-1}$$

This cap moves with the antenna and sweeps out the band $\theta \in [\frac{\pi}{2} - \gamma_{\max}, \frac{\pi}{2} + \gamma_{\max}]$. The rest of the sphere is never visible.

When the antenna is at $(\theta = \frac{\pi}{2}, \phi = \phi_a)$, the set of points at a common range d is

$$\left\{(\theta, \phi) | \quad \sin\theta \cos(\phi - \phi_a) = (R^2 + R'^2 - d^2)/2RR' \equiv \cos\gamma\right\}. \tag{C-2}$$

This locus is a small circle with the antenna as its pole. It is also the intersection of the sphere with a plane perpendicular to the plane of the orbit. Therefore, the orthographic projection of any of these small circles onto the

orbital plane is a straight line. In fact, the defining Equation in (C-2) can be expanded in terms of cartesian coordinates,

$$\begin{aligned} x &= R\sin\theta\cos\phi, \\ y &= R\sin\theta\sin\phi, \\ z &= R\cos\theta, \end{aligned} \tag{C-3}$$

as

$$x\cos\phi_a + y\sin\phi_a = R\cos\gamma, \tag{C-4}$$

which is the equation of a straight line in the xy plane. These lines form a two-parameter family (ϕ_a and γ, for example).

Projected onto the orbital plane, the latitudinal band visible to the antenna corresponds to the annulus

$$A \equiv \{(x,y)|\ \ R^2/R' \leq \sqrt{x^2+y^2} \leq R\}. \tag{C-5}$$

Thus, the set of lines of interest are those chords of the larger circle (radius R) that do not intersect the smaller concentric circle (radius R^2/R') except perhaps in a single point.

The radar reflectivity $\sigma(\theta,\phi)$ can be mapped onto the xy plane by defining $\tilde{\sigma}(x,y)$ such that $\tilde{\sigma}(x,y)dxdy = \sigma d\cos\theta d\phi$, which leads to

$$\tilde{\sigma}(x,y) = |\sec\theta|[\sigma(\theta,\phi) + \sigma(\pi-\theta,\phi)]. \tag{C-6}$$

Therefore, the projected reflectivity involves the even part of σ with respect to reflection in the orbital plane, and $\tilde{\sigma}$ is (integrably) singular at the outer edge of the annulus since $\sec\theta = R/\sqrt{R^2-x^2-y^2}$.

After range compression and suitable rescaling, the data collected by the antenna are integrals of σ along the small circles (C-2) on the sphere. These data are directly proportional to integrals of $\tilde{\sigma}$ along the corresponding lines in the xy plane. (Since parallel small circles project into parallel lines, the ratio of an infinitesimal arc along a small circle to the arc length along its projection equals the ratio of an infinitesimal area element to the area of its projection, *viz.* $\sec\theta$.) Thus the range-compressed data are equivalent to

$$K(\phi_a, r) = \int \tilde{\sigma}(r\cos\phi_a - s\sin\phi_a, r\sin\phi_a + s\cos\phi_a)ds, \tag{C-7}$$

where $r = R\cos\gamma$ is the minimum distance of the chord (C-4) from the center of the annulus. The limits of integration are $-R\sin\gamma \leq s \leq R\sin\gamma$, but by defining $\tilde{\sigma}(x,y) \equiv 0$ when $\sqrt{x^2+y^2} > R$, one can extend these limits to $\pm\infty$.

The inversion of (C-7) to obtain $\tilde{\sigma}\ (x,y)$ is almost the standard Radon tomography problem. The only nonstandard feature is the absence of data for all lines intersecting the "hole"

$$H \equiv \{(x,y)|\sqrt{x^2+y^2} < R^2/R'\}. \tag{C-8}$$

However, we are assured that an inverse exists and is unique within the annulus A, because of a theorem due to Helgason [53]. This theorem states that if an continuous function (here $\tilde{\sigma}$) is supported on a compact set in the plane ($A \cup H$), and its line integral is known along all lines exterior to a convex subset (H), then the function is uniquely defined within the complement of that subset.

In order to continue the analysis, we will make some simple changes of scale and some of notation. The change of scale is incorporated in our assuming that H is the hole $\{(x,y)|\sqrt{x^2+y^2} < 1\}$, and that $\tilde{\sigma}\ (x,y)$ is compactly

supported. In the interest of simplicity of notation, we replace ϕ_a by ϕ in Equation (C-8).

So we assume henceforth that we are given

$$K(\phi, r) = \int_{-\infty}^{\infty} \sigma(r\cos\phi - s\sin\phi, r\sin\phi + s\cos\phi)\, ds$$

for all $r \geq 1$. Next we suppose that $\tilde{\sigma}\ (x, y)$ is simply a function (not necessarily analytic) of the single complex variable $Z = x + iy$, and write accordingly $\tilde{\sigma}\ (x, y) = \sigma(Z)$. In these terms what we are given is:

$$K(\phi, r) = \int_{-\infty}^{\infty} \sigma((r + is)e^{i\phi})\, ds \tag{C-9}$$

for $r \geq 1$.

On our assumption that σ is compactly supported, we will formally invert the relation given in Equation (C-9), thus giving a concrete realization of the theorem of Helgason alluded to above, but the formulas we obtain are beset by innumerable numeric difficulties which we do not explore. (There are other efforts in the literature, to which we do not have access at this time, which encounter similar difficulties in attempting to invert Equation (C-9). See [54], [55].

One can see that the inversion problem is numerically delicate by virtue of the following observation. Suppose $\sigma(Z) = Z^{-k}$, $k \geq 2$. Then $\int_{-\infty}^{\infty} \sigma((r + is)e^{i\phi})\, ds = -ie^{-ik\phi} \int \frac{dz}{z^k}$, where the last line integral is over the line $z = r + is, -\infty < s < \infty$. Upon making the substitution $z = \frac{1}{\omega}$, the integral over the line is thrown into the line integral over a circle, $-\int \omega^{k-2} dw$, which is zero by Cauchy's theorem.

Thus the function $\sigma(Z) = \frac{1}{Z^k}$ returns tomographic information zero. The same is also true of $\sigma(Z) = \bar{Z}^{-k}, k \geq 2$; even more generally if $\sigma(Z)$ is any function, analytic in the exterior of the closed disk $Z \leq 1$, with a zero of at least second order at ∞, then

$$\int_{-\infty}^{\infty} \sigma((r+is)e^{i\phi})ds \equiv 0 \text{ for all } r \geq 1.$$

Because the radar returns are limited in range, the region of space that can contribute to $K(\phi, r)$ is necessarily compact in our application, even if there are returns from scatterers not on the surface of the sphere. So we probably do not have to be concerned about analytic functions contributing to σ. (No analytic function can be compactly supported.).

We return to inversion of Equation (C-9). If the Fourier series expansions for $K(\phi, r)$ and $\sigma(\rho e^{i\phi})$ are $\sum K_n(r)e^{in\phi}$ and $\sum \sigma_n(\rho)e^{in\phi}$ respectively, then:

$$\begin{aligned} K_n(r) &= \int_{-\infty}^{\infty} \sigma_n(\sqrt{r^2+s^2})e^{in\tan^{-1}\frac{s}{r}}\, ds \qquad \text{(C-10)} \\ &= 2\int_0^{\infty} \sigma_n(\sqrt{r^2+s^2})T_n\left(\frac{r}{\sqrt{r^2+s^2}}\right) ds, \end{aligned}$$

where $T_n(x)$ is the nth Chebyshev polynomial $= \cos(n\cos^{-1} x)$.

It is instructive to consider the special case $n = 0$.

$$K_0(r) = 2\int_0^{\infty} \sigma_0(\sqrt{r^2+s^2})\, ds$$

since $T_0(x) = 1$ for all arguments x. Changing the integration variable to $y \equiv r^2 + s^2$, and writing $r = \sqrt{x}$, we have

$$K_0(\sqrt{x}) = \int_x^{R^2} \frac{\sigma_0(\sqrt{y})}{\sqrt{y-x}}\, dy.$$

Here we have used the fact that σ_0 vanishes when its argument is greater than R. The above is a standard Abel integral and has the inverse

$$\sigma_0(\sqrt{z}) = -\frac{1}{\pi}\frac{d}{dz}\int_z^{R^2} \frac{K_0(\sqrt{x})}{\sqrt{x-z}}\,dx$$

Thus the inversion is essentially a "half-derivative" with respect to the variable $\rho = z^2$.

It is fortunate that in the Abel inverse the values of $\sigma_0(\sqrt{z})$ for $z \geq 1$ are determined by the values of $K_0(\sqrt{z})$ for $x \geq 1$.

We will have occasion to use the Rodriguez formula:

$$T_n(x) = \frac{(-1)^n}{2^n}\frac{\Gamma(1/2)}{\Gamma(n+1/2)}(1-x^2)^{1/2}D^n(1-x^2)^{n-1/2}, \qquad \text{(C-11)}$$

and will with its aid, extract $\sigma_n(r)$, for $r \geq 1$, from $K_n(r)$, given for $r \geq 1$.

In the right hand side of Equation (C-11) we make a substitution $v = \frac{r}{\sqrt{r^2+s^2}}$, yielding:

$$\begin{aligned}
\int_0^\infty \quad \sigma_n \quad & (\sqrt{r^2+s^2})T_n\left(\frac{r}{\sqrt{r^2+s^2}}\right) ds \\
&= \frac{1}{r}\int_0^1 \sigma_n(r/v)(r/v)^2 \frac{T_n(v)}{\sqrt{1-v^2}}\,dv \\
&= \frac{1}{r}\int_0^1 \tau_n(v/r)\frac{T_n(v)}{\sqrt{1-v^2}}\,dv, \qquad \text{(C-12)}
\end{aligned}$$

where $\tau_n = \sigma_n\left(\frac{1}{v}\right)\left(\frac{1}{v}\right)^2$. $\tau(v)$ is identically zero in a neighborhood of $v = 0$, since σ, hence σ_n, is compactly supported.

Since $\frac{T_n(v)}{\sqrt{1-v^2}}$ is by Rodriguez an nth derivative, we carry out n integrations by parts on the last integral in Equation (C-12). Upon dropping scale factors

which depend on n and r in a known fashion, we can recover the expression

$$\begin{aligned} & \int_0^1 \tau_n^{[n]}(v/r)(1-v^2)^{n-1/2}dv \\ = & \int_0^1 h(v/r)(1-v^2)^{n-1/2}dv \end{aligned} \tag{C-13}$$

where we have replaced $\tau_n^{[n]}$ by $h(v)$.

In Equation (C-13) make an additional substitution $v = ry^{1/2}$, putting $r^2 = \frac{1}{U}$ at the same time, while dropping scale factors as before, to recover:

$$\begin{aligned} L(U) &= \int_0^U \frac{h(\sqrt{y})}{\sqrt{y}}(U-y)^{n-1/2}\,dy \\ &= \int_0^U H(y)(U-y)^{n-1/2}\,dy \end{aligned} \tag{C-14}$$

Since r was confined to $r \geq 1$, U satisfies $U \leq 1$. Our problem now is given the expression Equation (C-14) for $U \leq 1$, to recover $H(y)$ for $O \leq y \leq 1$. H is zero in a neighborhood of $y = 0$, but this restriction may now be set aside.

One finds readily that

$$L_1(U) = \int_0^U L(t)dt = \frac{1}{n+1-1/2}\int_0^U H(y)(U-y)^{n+1-1/2}\,dy$$

Continuing in same fashion, we have:

$$\int_0^U L_1(t)dt = \frac{1}{(n+2-1/2)(n+1-1/2)}\int_0^U H(y)(U-y)^{n+2-1/2}\,dy$$

Thus we may recover from what is given all expressions:

$$\begin{aligned} & \int_0^U H(y)(U-y)^{n-1/2}\,(U-y)^k dy \\ = \; & U^{n+1/2+k}\int_0^1 H(U(1-t))t^{n-1/2}\,t^k\,dt \end{aligned}$$

Setting $U = 1$, we may recover

$$\int_0^1 H(1-t)t^{n-1/2}\,P(t)\,dt$$

for any polynomial $P(t)$. If we let the polynomials $P(t)$ run through a complete orthonormal family on the interval [0,1] with respect to the weight function $t^{n-1/2}$, we obtain the expansion in this family of $H(1-t)$ and thus recover $H(y)$.

The assorted integrations, differentiations, and change of variable we have undertaken above, may presumably be combined into one master formula. Indeed, an Abel inversion, slightly generalized, may be used to determine τ_n directly from K_n. We have not done so; our main purpose was to convince ourselves and the reader that inversion is possible. We have not investigated numerical implementation either.

References

[1] Desai, M. D. and W. Jenkins, "IEEE Trans. Image Processing, 1, 505-517 (1992).

[2] Radon, S. Über die Bestimmung...(1917) Radon's original paper translated in Reference above.

[3] Cormack, A.M. - Representation of a Function by its Line Integrals, with some Radiological pplications. Journal of Applied Physics, Vol. 34, #9, 1963, 2722-2727.

[4] Deans, S.R. The Radon Transform and Some of Its Applications, Wiley (1983).

[5] Goldstein, R.M., H.A. Zebker, and C.L. Werner, "Satellite Radar Interferometry: Two-dimensional Phase Unwrapping," Radio Science 23, 713-720 (1988).

[6] Bamler, R., A comparison of range-Doppler and wavenumber domain SAR focusing algorithms, **IEEE Trans. Geosci. Remote Sens. 30**, 706-713 (1992).

[7] Curlander, J. C. and McDonough, R. N., "Synthetic aperture radar: systems and signal processing", Wiley, N.Y. (1991).

[8] Barber, B. C., "Theory of digital imaging from orbital synthetic aperature radar," Tech. Rpt. 83079, Royal Aircraft Establishment, Farnborough, Hants., UK (Nov. 1983).

[9] Barber, B. C., "Theory of digital imaging from orbital synthetic aperature radar," **Intl. J. Remote Sensing 6**, 1009-1057 (1985).

[10] Chang, C. Y., M. Jin and J. C. Curlander, Squint mode SAR Processing Algorithms, **Proc. IGARSS '89**, 1702-1706 (1989).

[11] Smith, A. M. A new approach to range-Doppler SAR processing, **Int. J. Remote Sensing 12**, 235-251 (1991).

[12] Wong, F. H. and Cumming, I. G., Error sensitivities of a secondary range compression algorithm for processing squinted satellite SAR data, **Proc. IGARSS '89**, 2584-2587 (1989).

[13] Rocca, F., Synthetic aperture radar: A new application for wave equation techniques, in "Stanford Exploration Project Report SEP-56," 167-189 (1987).

[14] Wehner, D.R., "High Resolution Radar," Artech House, Norwood, MA (1987).

[15] Kelley, M.C., "The Earth's Ionosphere," Academic Press, San Diego (1989).

[16] Rino, C.L., "On the Application of Phase Screen Models to the Interpretation of Ionospheric S," Radio Science, 17, 4, 1982, 855-867.

[17] Ishimaru, A., "Wave Propagation and Scattering in Random Media," II, Academic Press, New York, 1978.

[18] Rino, C. and C.E. Hess, "Numerical Simulation of SAR Propagation Effects," Final Report on Contract 78-9790 for the Defense Nuclear Agency (1978).

[19] Massonnet, D., M. Rossi, C. Carmona, F. Adragna, G. Peltzer, K. Feigl, and T. Rabaute, "The Displacement Field of the Landers Earthquake Mapped by Radar Interferometry." Nature 364, 138-142 (1993).

[20] Clifford, S.F., "The Classical Theory of Wave Propagation in a Turbulent Medium," in "Laser Beam Propagation in the Atmosphere," Ed: J.W. Strohbehn, Springer-Verlag, Berlin (1978).

[21] Raney, Keith, "Synthetic Aperture Imaging Radar and Moving Targets", IEEE Trans. on Aerospace and Electronics Systems, Vol AES-7, No. 3, p. 499-505.

[22] Freeman, A., A. Currie, "Synthetic Aperture Radar (SAR) Images of Moving Targets", GEC Journal of Research, Vol 5, No. 2, 1987, p. 106-114.

[23] Chen, H.C, C. D. McGillem, "Target Motion Compensation by Spectrum Shifting in Synthetic Aperture Radar", IEEE Trans. on Aerospace and Electronic Systems Vol 28, No. 3, July 1992, p 895-901.

[24] Muller-Buffington (1974).

[25] N. Levanon, Radar Principles (John Wiley, New York, (1988) p.268-284.

[26] Prati, C., F. Rocca, A. M. Gwarhieri, and F. Damonti, (1990), Seismic Migration for SAR Focusing: Interferometric Applications, *IEEE Trans. Geosec. Remote Sensing*, **28**, 627-640

[27] Lin, Q., J. F. Vesecky and H. Zebker (1992), New Approaches in Inteferometric SAR Data Processing, *IEEE Trans. Geosec. Remote Sensing*, **30**, 560-567.

[28] Lin, Q., (1992), New Approaches to Topographic Estimation Using Interferimetic SAR Images, Ph. D. Thesis, Elec. Eng. Dept., Stanford University, Stanford, CA.

[29] Elachi, C., E.A. Roth and G. G. Schaber, Spaceborne radar subsurface imaging in hyperarid regions, IEEE Trans. Geosci. and Remote Sens. GE-22, 283-388 (1984)

[30] Dudgeon, D., Lincoln Labs briefing to JASON, 1993.

[31] Maric, S.F., and E. Titlebaum, Nov. 1990, "Frequency Hop Multiple Access Codes Based Upon the Theory of Cubic Congruences," *IEEE Trans. on Aerospace and Electronic Systems*, Vol. 26, No. 6.

[32] Baumert, L. D., "Cyclic Difference Sets," Springer-Verlag, New York (1971).

[33] Callan, C., et al., "Precision Strike" (JASON report JSR-92-170,1993).

[34] Cornwall, J.M., et al., "SAR and GPS in Precision Strike" (JASON report JSR-92-171, 1993).

[35] Avrin, J., "Bistatic Space-Based Radar Experimentation at the Aerospace Corporation in 1977," unpublished report, 1980.

[36] Duclos, D.P., et al., "Spaceborne/Airborne Bistatic Radar System," briefing to the Defense Science Board, 1993.

[37] A. D. Siegel and J.J. Wilcox, "Radar Sea Clutter Doppler Characteristics" Rome Air Development Center Report, RADC-TR-90-250 (1990). See Figure 32, p45.

[38] Helgason, S. The Radon Transform, Birkhauser (1980).

[39] Costas, J.P., 1984, "A Study of a Class of Detection Waveforms Having Nearly Ideal Range–Doppler Ambiguity Properties," *Proc. IEEE*, 72, pgs. 996-1,009.

[40] Golomb, S.W., Sept. 1984, "Construction and Properties of Costas Arrays," *Proc. IEEE*, 72 9, pgs. 1,143 - 1,163.

[41] Fried, D.L., and J.L. Vaughn, "Branch Cuts in the Phase Function," Applied Optics 31, 2865-2882 (1992).

[42] Ghiglia, D.C., and G.A. Mastin, "Two-dimensional Phase Correction of Synthetic-aperture-radar Imagery," Optics Letters 14, 1104-1106 (1989).

[43] Eichel, P.H., and C.V. Jakowatz, Jr.,"Phase-gradient Algorithm as an Optimal Estimator of the Phase Derivative," Optics Letters 14, 1101-1103 (1989).

[44] Flatté, S.M., "Wave Propagation Through Random Media: Contributions from Ocean Acoustics," Proc. of the IEEE, 71, 1267-1294, Nov. 1983.

[45] Martin, J.M., and S.M. Flatté, "Intensity Images and Statistics from Numerical Simulation of Wave Propagation in Three-dimensional Random Media," Applied Optics, 27, 2111-2126, Special Issue June 1988.

[46] Martin, J.M. and S.M. Flatté, "Simulation of Point-source Scintillation in Three-dimensional Random Media," J. Opt. Soc. Am. A, 7, 838-837, 1990.

[47] Dashen, R., G.Y. Wang, Stanley Flatté, C. Bracher, "Moments of Intensity and Log-intensity: New Asymptotic Results for Waves in Power-law Media," J. Opt. Soc. Am. A., 92, in press, 1993.

[48] Flatté, Stanley M., G.Y. Want, J. Martin, "Irradiance Variance of Optical Waves Through Atmospheric Turbulence by Numerical Simulation and Comparison with Experiment," J. Opt. Soc., Am. A, 922 in press, 1993.

[49] Flatté, S.M., R. Dashen, W. M. Munk, K.M. Watson, F. Zachariasen, "Sound Transmission Through a Fluctuating Ocean," Cambridge University Press, 1979, London.

[50] Tatarskii, V.I., "The Effects of Turbulent Atmospheres on Wave Propagation," National Technical Information Service, Springfield, Virginia, 1971.

[51] Rignot, E. and Drinkwater, M, "Winter Sea Ice Mapping From Multiparameter," Synthetic Aperture Radar, in press **J. Glaciol.** (1993)

[52] Massonnet, D., M. Rossi, C. Carmona, F. Adragna, G. Peltzer, K. Feigi and T. Rabaute, The displacement field of the Landers earthquake mapped by radar interferomentry, **Nature 364**, 138-142 (1993).

[53] Helgason, S. 1980, *The Radon transform*

[54] Quinto, T. - Tomographic reconstruction from incomplete data - Inverse Problems, Vol 4, 1988, pp. 867-876

[55] Quinto, T. - Computer Tomography and Rockets, Springer Notes in Math number 1497, pp. 261-268.

DISTRIBUTION LIST

Director of Space and SDI Programs
SAF/AQSC
1060 Air Force Pentagon
Washington, DC 20330-1060

CMDR & Program Executive Officer
U S Army/CSSD-ZA
Strategic Defense Command
PO Box 15280
Arlington, VA 22215-0150

A R P A Library
3701 North Fairfax Drive
Arlington, VA 22209-2308

Dr Peter M Banks
3485 Narrow Gauge Way
Ann Arbor, MI 48105

Dr Arthur E Bisson
Director
Technology Directorate
Office of Naval Research
Room 407
800 N. Quincy Street
Arlington, VA 20350-1000

Dr Albert Brandenstein
Chief Scientist
Office of Nat'l Drug Control Policy
Executive Office of the President
Washington, DC 20500

Mr. Edward Brown
Assistant Director
ARPA/SISTO
3701 North Fairfax Drive
Arlington, VA 22203

Dr H Lee Buchanan, I I I
Director
ARPA/DSO
3701 North Fairfax Drive
Arlington, VA 22203-1714

Dr Curtis G Callan Jr
50 Lafayette Road, West
Princeton, NJ 08540

Dr Ashton B Carter
Nuclear Security & Counter Proliferation
Office of the Secretary of Defense
The Pentagon, Room 4E821
Washington, DC 20301-2600

Dr Collier
Chief Scientist
U S Army Strategic Defense Command
PO Box 15280
Arlington, VA 22215-0280

Dr. John M Cornwall
Dept of Physics
Univ of California/Los Angeles
Los Angeles, CA 90024

D T I C [2]
Cameron Station
Alexandria, VA 22314

Dr William J Dally
Massachusetts Institute of Tech
Dept of Electrical Eng & Comp Science
Bldg NE43, Rm 620
545 Technology Square
Cambridge, MA 02139

DISTRIBUTION LIST

Mr John Darrah
Senior Scientist and Technical Advisor
HQAF SPACOM/CN
Peterson AFB, CO 80914-5001

Dr Gary L Denman
Director
ARPA/DIRO
3701 North Fairfax Drive
Arlington, VA 22203-1714

Dr John M Deutch
Under Secretary
DOD, OUSD (Acquisition)
The Pentagon, Room 3E933
Washington, DC 20301

Professor Freeman J Dyson
Institute for Advanced Study
Olden Lane
Princeton, NJ 08540

Mr John N Entzminger
Chief, Advance Technology
ARPA/ASTO
3701 North Fairfax Drive
Arlington, VA 22203-1714

Dr Stanley M Flatte
678 Spring Street
Santa Cruz, CA 95060

Mr Dan Flynn [5]
OSWR
Central Intelligence Agency
Washington, DC 20505

Dr Paris Genalis
Deputy Director
OUSD(A&T)/S&TS/NW
The Pentagon, Room 3D1048
Washington, DC 20301

Dr Lawrence K. Gershwin
Central Intelligence Agency
NIC/NIO/S&T
7E47, OHB
Washington, DC 20505

Dr Jeremy Goodman
Princeton University Observatory
Peyton Hall
Princeton, NJ 08544

Mr. Thomas H Handel
Office of Naval Intelligence
The Pentagon, Room 5D660
Washington, DC 20350-2000

Dr Robert G Henderson
Director
JASON Program Office
The MITRE Corporation
7525 Colshire Drive
Mailstop Z561
McLean, VA 22102

Dr Barry Horowitz
President and Chief Exec Officer
The MITRE Corporation
202 Burlington Road
Bedford, MA 01730-1420

Dr Paul Horowitz
Lyman Laboratory of Physics
Harvard University
Cambridge, MA 02138

DISTRIBUTION LIST

Dr William E Howard I I I [2]
Director of Advanced Concepts &
Systems Design
The Pentagon Room 3E480
Washington, DC 20301-0103

Dr Gerald J Iafrate
U S Army Research Office
PO Box 12211
4330 South Miami Boulevard
Research Triangle NC 27709-2211

J A S O N Library [5]
The MITRE Corporation
Mail Stop W002
7525 Colshire Drive
McLean, VA 22102

Dr Anita Jones
Department of Defense
DOD, DDR&E
The Pentagon, Room 3E1014
Washington, DC 20301

Dr Bobby R Junker
Office of Naval Research
Code 111
800 North Quincy Street
Arlington, VA 22217

Lt Gen, Howard W. Leaf, (Retired)
Director, Test and Evaluation
HQ USAF/TE
1650 Air Force Pentagon
Washington, DC 20330-1650

Dr Alfred Lieberman
Chief Science Advisor, Acting
USACDA
320 21st Street NW
Washington, DC 20451

Dr. John Lyons
Director of Corporate Laboratory
US Army Laboratory Command
2800 Powder Mill Road
Adelphi, MD 20783-1145

Col Ed Mahen
ARPA/DIRO
3701 North Fairfax Drive
Arlington, VA 22203-1714

Dr. Arthur Manfredi
OSWR
Central Intelligence Agency
Washington, DC 20505

Mr James J Mattice
Deputy Asst Secretary
(Research & Engineering)
SAF/AQ
Pentagon, Room 4D-977
Washington, DC 20330-1000

Dr Greg Moore [10]
Office of Research and Development
Central Intelligence Agency
Washington, DC 20505

Dr Bill Murphy
Central Intelligence Agency
ORD
Washington, DC 20505

Mr Ronald Murphy
ARPA/ASTO
3701 North Fairfax Drive
Arlington, VA 22203-1714

DISTRIBUTION LIST

Dr Julian C Nall
Institute for Defense Analyses
1801 North Beauregard Street
Alexandria, VA 22311

Dr William A Nierenberg
Scripps Institute of Oceanography
Mail Code 0221
University of California/San Diego
La Jolla, CA 92092-0221

Dr Ari Patrinos
Director
Environmental Sciences Division
ER74/GTN
US Department of Energy
Washington, DC 20585

Dr Francis W Perkins
2730 Caminito Prado
La Jolla, CA 92037

Dr Bruce Pierce
USD(A)D S
The Pentagon, Room 3D136
Washington, DC 20301-3090

Dr William H Press
Harvard College Observatory
60 Garden Street
Cambridge, MA 02138

Dr Thomas A Prince
California Institute of Technology
220-47
Pasadena, CA 91125

Mr John Rausch [2]
Division Head 06 Department
NAVOPINTCEN
4301 Suitland Road
Washington, DC 20390

Records Resource
The MITRE Corporation
Mailstop W115
7525 Colshire Drive
McLean, VA 22102

Dr Victor H Reis
US Department of Energy
DP-1, Room 4A019
1000 Independence Ave, SW
Washington, DC 20585

Dr Oscar S Rothaus
106 Devon Road
Ithaca, NY 14850

Dr Fred E Saalfeld
Director
Office of Naval Research
800 North Quincy Street
Arlington, VA 22217-5000

Dr Dan Schuresko
O/DDS&T
Central Intelligence Agency
Washington, DC 20505

Dr John Schuster
Technical Director of Submarine
and SSBN Security Program
Department of the Navy OP-02T
The Pentagon Room 4D534
Washington, DC 20350-2000